University of South Carolina

Scholar Commons

Theses and Dissertations

Spring 2020

Design and Testing of a Supercritical Carbon Dioxide Plasma Reactor

Gregory Belk

Recommended Citation

Belk, G.(2020). *Design and Testing of a Supercritical Carbon Dioxide Plasma Reactor.* (Master's thesis). Retrieved from https://scholarcommons.sc.edu/etd/5944

DESIGN AND TESTING OF A
SUPERCRITICAL CARBON DIOXIDE PLASMA REACTOR

by

Gregory Belk

Bachelor of Science
Francis Marion University, 2012

Bachelor of Science
University of South Carolina, 2018

Submitted in Partial Fulfillment of the Requirements

For the Degree of Master of Science in

Mechanical Engineering

College of Engineering and Computing

University of South Carolina

2020

Accepted by:

Tanvir I. Farouk, Director of Thesis

Sang Hee Won, Reader

Jamil A. Khan, Reader

Cheryl L. Addy, Vice Provost and Dean of the Graduate School

DEDICATION

This thesis is dedicated to the loving memory of my grandmother, Marilynn Belk. Her love for the Gamecocks and her support is what has made all this possible. Go Gamecocks!

ACKNOWLEDGEMENTS

First and foremost, I would like to acknowledge and thank Dr. Farouk for his support. This project has been a joy and a good challenge. I would also like to thank each of the members of the RASAER Lab. Being a member of the team has been an honor, and I'm glad to have had the opportunity to work with you all.

Thank you to the employees in the machine shop for teaching me how to machine my own parts and thank you for always being so eager to help with this project.

I would like to thank Dr. Won for allowing me to work in his lab. Working alongside Ayuob and Seungjae has been a pleasant experience. I thank each of my previous instructors for sharing their knowledge with me.

Finally, I'd like to thank my wife and my family for supporting me.

ABSTRACT

The objective of this project was to design, build, and test a plasma reactor capable of operating in the supercritical conditions. The reactor allows for the initiation of a plasma discharge in different fluids driven by a direct current (DC) power supply operating either in steady state mode or pulsing mode. The reactor was specifically designed for igniting plasmas within supercritical carbon dioxide, which has a pressure of 72.9 atm and 31.1 degrees Celsius.

A series of runs were conducted for varying pressures and inter-electrode separation, which allowed testing the operation regimes of the reactors. Finally, plasma experiments were conducted under supercritical carbon dioxide. Several diagnostics were performed which included high speed image acquisition, voltage-current characterization, as Schlieren imaging. Measurements indicated the presence of severe parasitic capacitance in the power circuit, which resulted in significant ringing and oscillatory patterns in the current signals. The Schlieren images showed the formation of density/pressure waves forming between the electrodes. Unexpected events such as electromagnetic pulses, sharp gradients and rise in discharge currents, spectral line broadening, electrode degradation, and discharge driven shockwaves in liquid were observed. Some of these observations will help in guiding the way to design and build an improved supercritical reactor that can mitigate some of these negative or unwanted effects.

TABLE OF CONTENTS

LIST OF FIGURES

LIST OF SYMBOLS

”	inches
˚C	Degrees Celsius
˚F	Degrees Fahrenheit
A	Amperes
atm	Atmosphere
d	Electrode gap
DC	Direct current
kV	kilovolts
K	Kelvin
μ	Micro 10^{-6}
m	milli 10^{-3}
mA	milliamperes
MPa	Megapascal
P_c	Critical pressure
psig	pounds per square inch (gauge pressure)
r	radius of curvature
T_c	Critical temperature
V	Volts

LIST OF ABBREVIATIONS

CBD	Cannabidiol
CO_2	Carbon dioxide
DAQ	Data acquisition
EMI	Electromagnetic interference
OES	Optical emission spectroscopy
PEEK	Polyether ether ketone
ppm	Parts per million
RCL	Resistor capacitor inductor
SCF	Supercritical fluid
sCO_2	Supercritical carbon dioxide
SCR	Supercritical reactor

CHAPTER 1

INTRODUCTION

1.1 CHARACTERISTICS OF SUPERCRITICAL CO_2

The thermodynamic state of CO_2 can be expressed in terms of pressure and temperature. Carbon dioxide has a critical point at $P_c = 72.83$ atm and a critical temperature at $T_c = 304.25$ K. This is shown in the phase diagram in Figure 1.1.

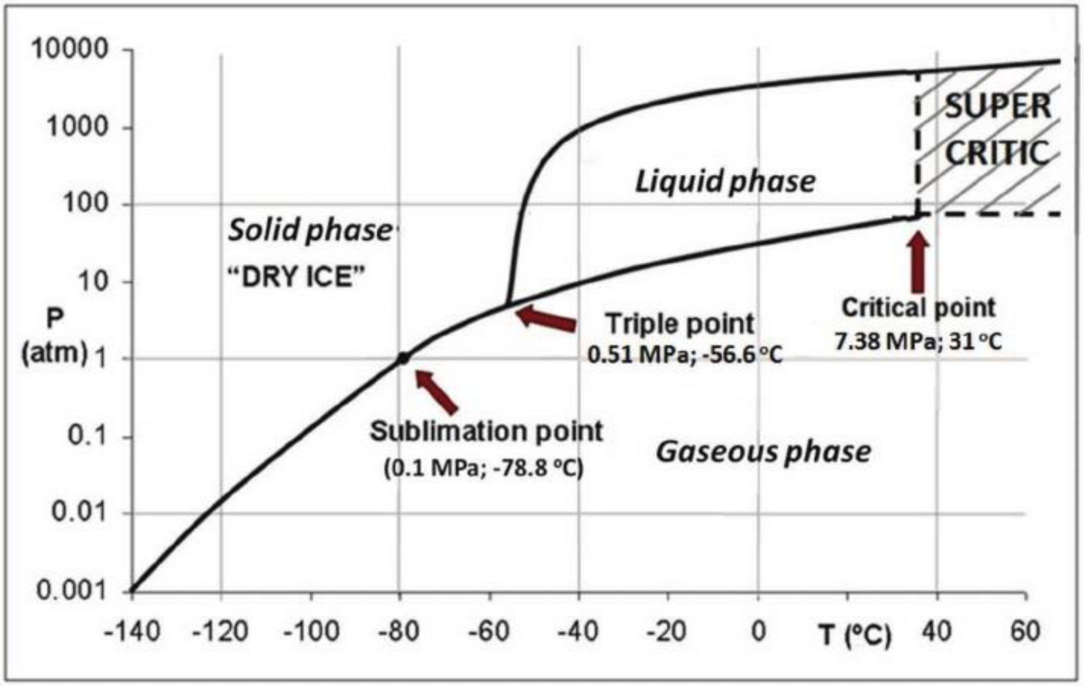

Figure 1.1 Carbon dioxide phase diagram

In supercritical fluids (SCFs), a small temperature or pressure fluctuation will cause a large density fluctuation. This is because the fluid is above the saturation curve where it behaves as a single-phase supercritical fluid [1]. If the fluid properties were located within the saturation curve, it would be two-phase, and heating or pressurizing would play a larger role on the gas to liquid ratio.

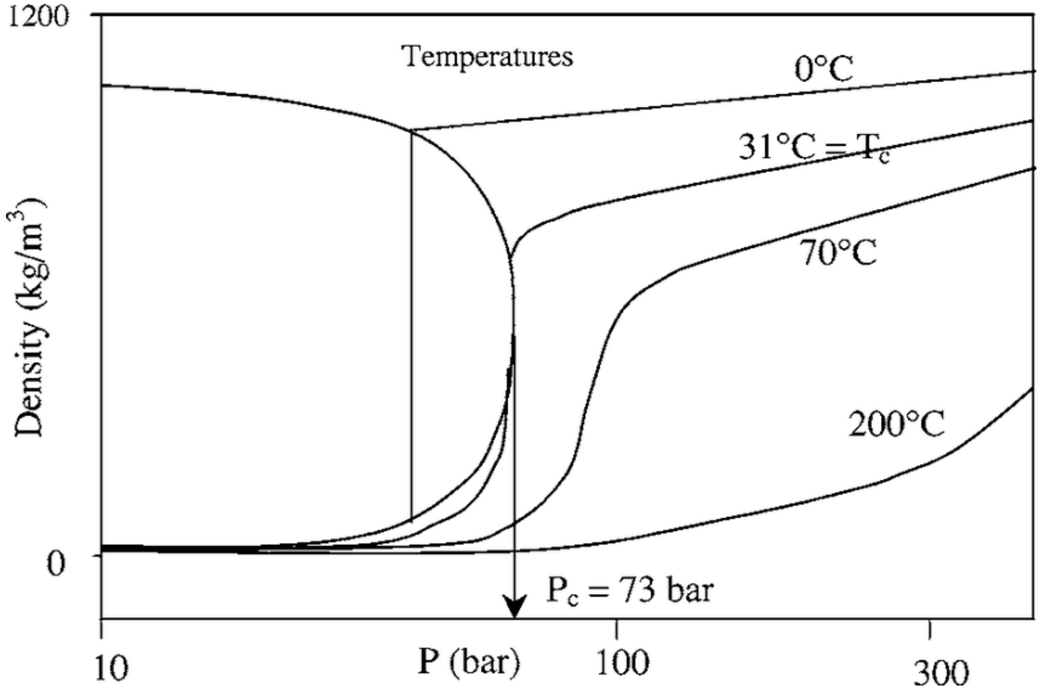

Figure 1.2 Carbon dioxide density vs pressure plot

1.2 APPLICATIONS OF SUPERCRITICAL CO_2

Carbon dioxide is in the gaseous phase at standard pressure and temperature. This gaseous CO_2 is a waste product of many natural and human created sources that enters the atmosphere and acts as a greenhouse gas. The planet has carbon dioxide naturally present in the atmosphere, but too much of it could potentially cause a runaway greenhouse effect [2]. This possibility has motivated many scientists and engineers around the world to take a closer look at more applications for CO_2. With CO_2 being a waste product, it is a relatively inexpensive gas.

Supercritical CO_2 (sCO_2) is one of the most popular solvents used for extraction processes [3]. It is known as a tunable solvent due to its ability to selectively extract essential oils depending on its pressure and temperature. The low temperature of sCO_2 (31.1+ °C) makes it a great solvent because high temperatures do not denature the product. Carbon dioxide is also nontoxic, so it is a clean and safe solvent to mix with food. This extraction process leaves no residue behind. The sCO_2 fluid extraction industry is rapidly growing. Some common products produced using sCO_2 fluid extraction processes are decaffeinated coffee beans, cannabidiol (CBD), and other natural oils produced from fruits, vegetables, and nuts.

As semiconductors and nanoelectronic devices continue to shrink, supercritical CO2 is being used for cleaning and deposition [4]. There is also great use for CO_2 being used as a cooling agent in machining. Carbon dioxide is pressurized to supercritical conditions, and then it ejected at atmospheric pressure towards the cutting tool. This process doesn't make a mess like using water as a cooling agent. The rapid expansion of the CO_2 at atmospheric pressure can remove much more heat from the cutting tool than water.

1.3 POTENTIAL APPLICATIONS OF PLASMAS IN SUPERCRITICAL CO_2

Plasmas in sCO_2 have the potential to be used in many different applications in various fields. The high density and enthalpy of sCO_2 combined with the high reactivity of pulsed laser plasmas or either electric discharge plasmas could potentially have a place in the fabrication of nanomaterials as well as chemical synthesis [5]. Supercritical CO_2 plasmas have shown great promise in synthesizing Si nanoparticles, molecular diamonds, Ag, Au nanoparticles and fractals, and ZnO nanoparticles [6].

There is also a potential to use sCO_2 plasmas while exploring the planet Venus. Venus is a very good example of a superheated planet with a thick atmosphere made up mostly of CO_2 [7]. Venus is the hottest planet in the solar system with an average temperature of 462°C and a pressure of approximately 92 atm. An ocean of supercritical carbon dioxide exists naturally on the surface of Venus. Understanding plasmas in sCO_2 could possibly shine a light on what happens in a lightning storm on Venus. There could be many more sCO_2 plasma applications related to Venus, and it should be investigated since Venus is our closest neighboring planet, and it has a gravity similar to that on Earth.

1.4 LITERATURE REVIEW

Plasmas in supercritical carbon dioxide have been a subject of interest for engineers and scientists for over 10 years. A team led by C. H. Zhang studied corona and arc discharges in supercritical CO_2 [8]. Zhang found that DC corona discharges can be produced in supercritical CO_2 using a point-plane electrode configuration. Zhang also found that an arc discharge would form when the corona became large enough to bridge the gap between the electrodes. Breakdown voltages were measured at 0.5 mm and 0.8 mm electrode gap spacings at the critical temperature for pressures ranging from 0.1 to 15 MPa. Zhang reported that there appeared to be a correlation between the density of the supercritical CO_2 and discharge voltage. Figure 1.3 shows a trough near the critical point for the 0.5 mm electrode gap.

Rather than being a homogenous fluid, supercritical fluid has dense clusters and less dense clustered regions. Zhang theorizes that the mean free path of the electrons in the SCF increase due to the clustering of CO_2 molecule, and this allows for a lower breakdown voltage. Figure 1.4 shows typical electron channeling in supercritical CO_2 [9]. Electron channeling describes the way electrons move through the fluid. The clusters affect the ionization mechanisms for electron collision, recombination, and attachment.

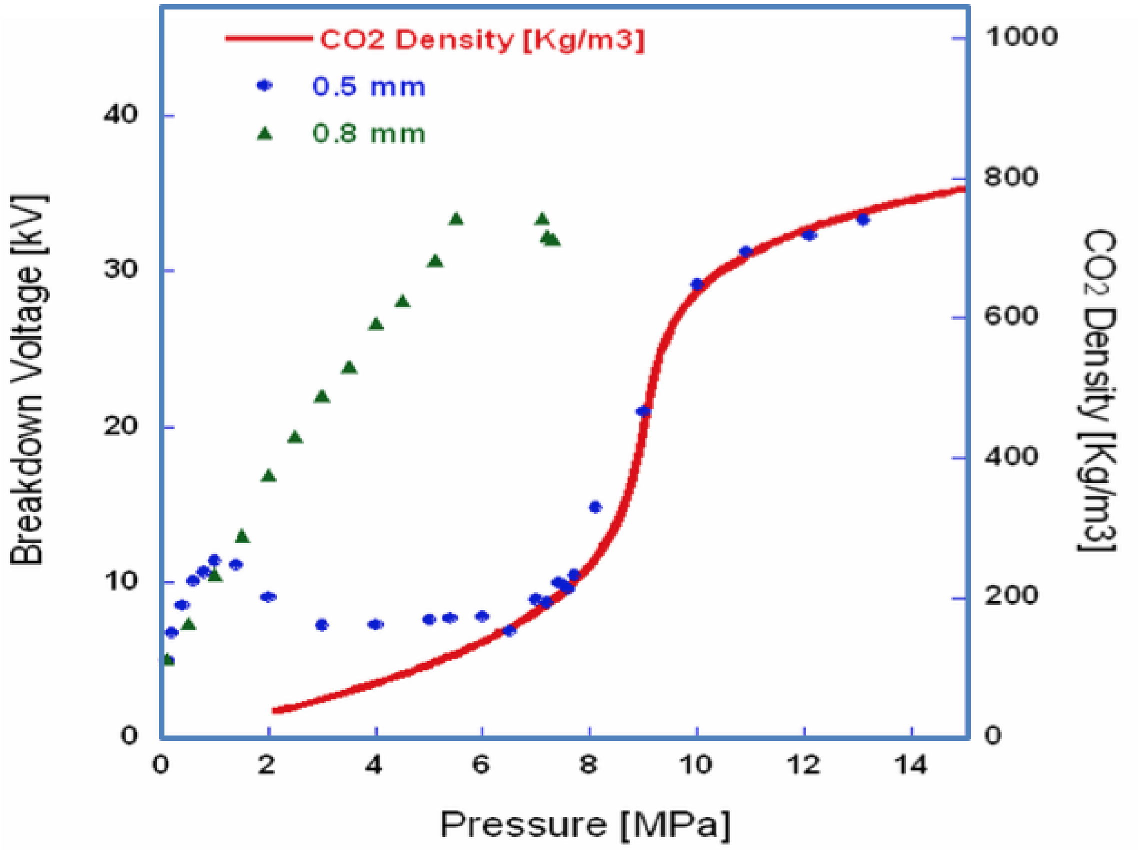

Figure 1.3 Breakdown voltage of CO_2 from 0.1 MPa to 15 MPa [8]

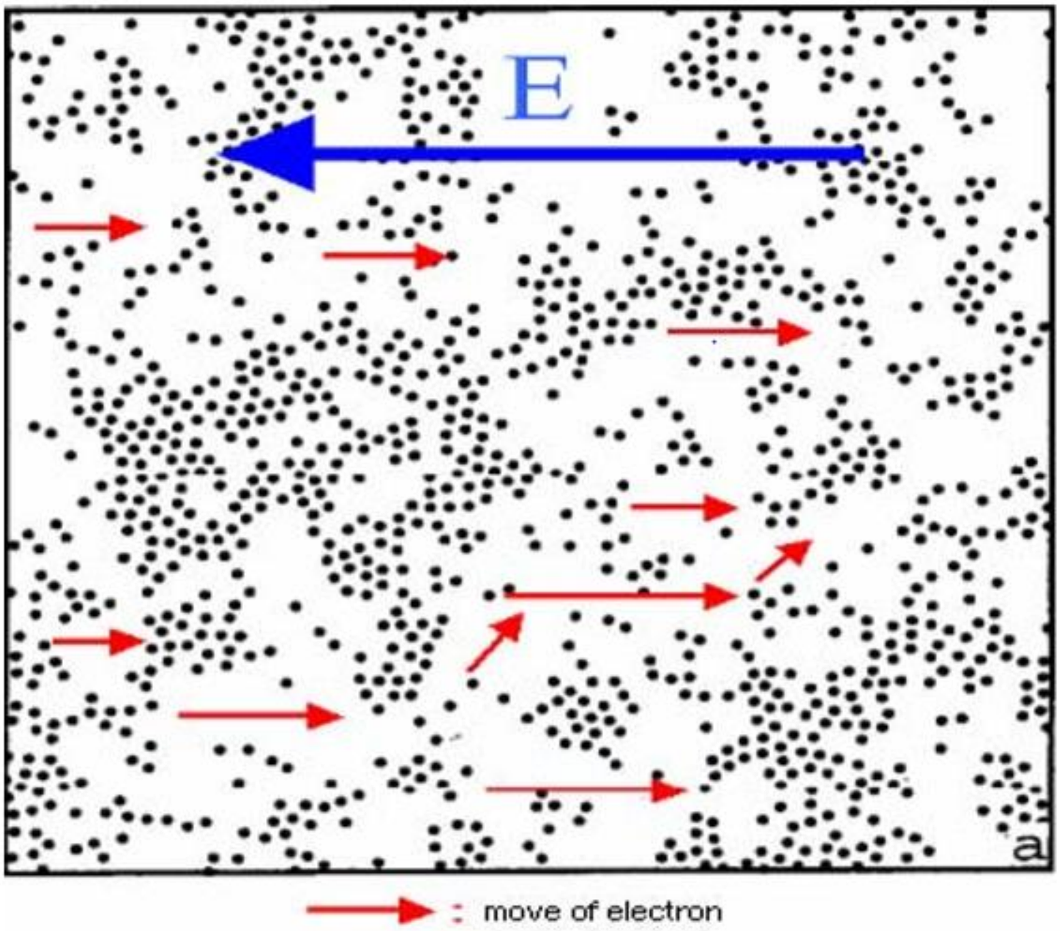

Figure 1.4 Electron channeling in supercritical CO_2 [9]

Zhang also lays out some of the basic ionization processes for understanding how corona discharges and breakdown occur [8]. Equation 1 shows that free electrons will increase and develop into avalanches due to high electric field regions. Equation 2 shows that positive ions may combine with electrons to produce photons. Equation 3 states that photons produced from Equation 2 will produce more electrons ahead of the avalanche, which can cause streamers to develop. In high density fluids, it is very common for negative ions to be formed by electron collisions, as shown in Equation 4. This can slow down or stop the growth of electron avalanches.

$$(CO_2)_n + e \longrightarrow (CO_2)_{+n} + e + e \qquad (1)$$

$$(CO_2)_{+n} + e \longrightarrow (CO_2)_n + \text{energy} \qquad (2)$$

$$\text{photon} + (CO_2)_n \longrightarrow (CO_2)_{+n} + e \qquad (3)$$

$$e + (CO_2)_n \longrightarrow (CO_2)_{-n} \qquad (4)$$

Further research into the effect of electrode geometry and power supply polarity was later conducted by Tsuyoshi Kiyan [10,11]. Kiyan demonstrated that an anode tip with a small radius of curvature (80 µm) can achieve electrical breakdown at a lower voltage than one with a larger radius of curvature (150 µm). His research also showed that a corona discharge precedes only as a pulse right before the arc discharge in supercritical CO_2 when using positive polarity. However, a stable corona discharge can be produced using a negative polarity power supply without arcing. Figure 1.5 shows that a negative corona discharge can be produced at a lower voltage than that required for electrical breakdown. Figure 1.5 also shows that breakdown using a positive polarity is not dependent on fluid density. Whereas, breakdown voltage is pressure dependent when a negative polarity power supply is used.

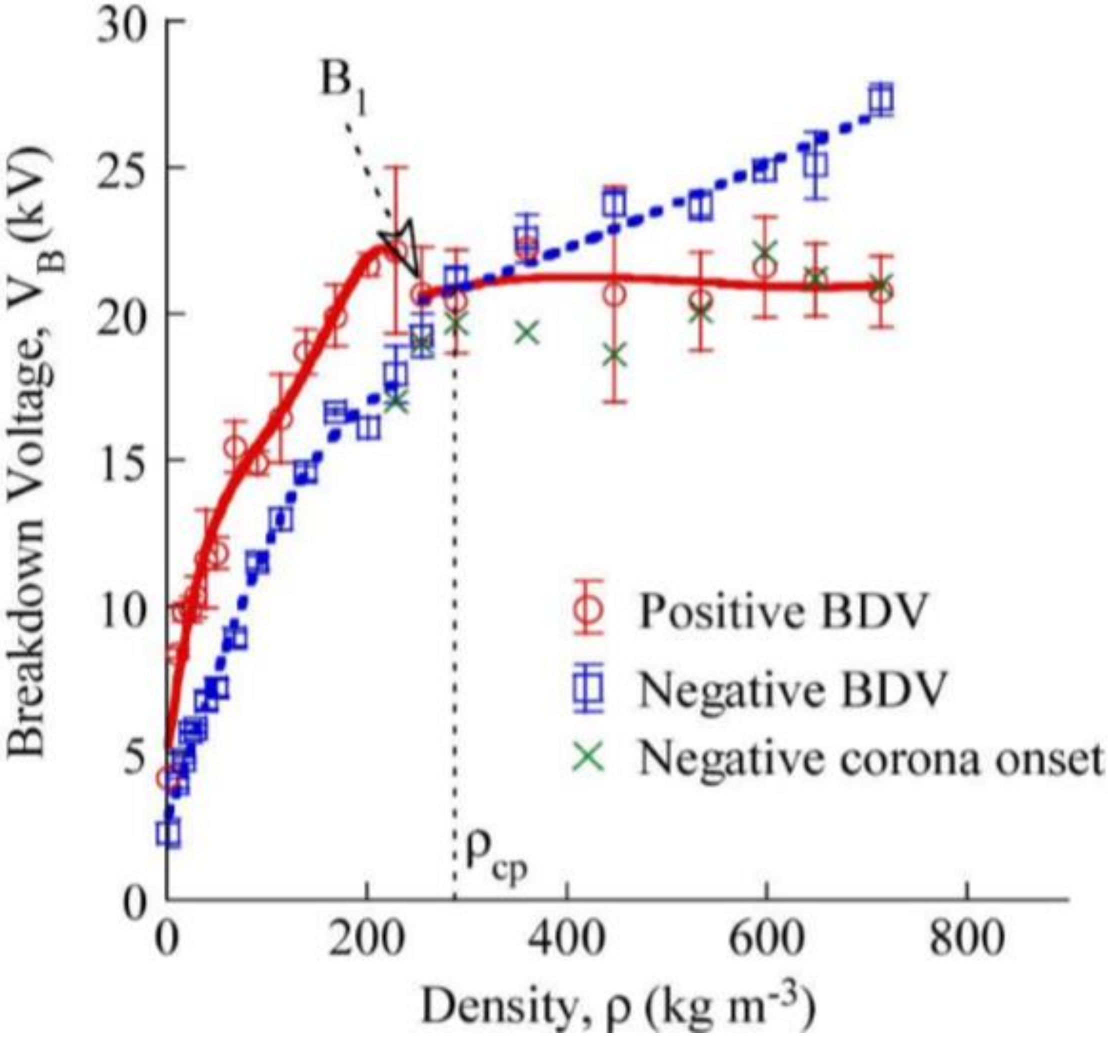

Figure 1.5 Dependence on BDV on CO_2 density; T = 313 K, d = 250 µm, r = 80 µm [11]

Research led by Furusato was carried out to observe the streamer formation of a positive prebreakdown discharge in the gaseous, liquid, and supercritical CO_2 phases [12,13]. Furusato was able to achieve discharge voltages up to 90 kV using a high-voltage bushing made of polyether ether ketone (PEEK) polymer. PEEK is an excellent electrical insulator that is very strong under compression [14]. Laser pulsed Schlieren imaging was used to get time resolved images of the streamers. The electrode gap used in Furusato's system was 7 mm. A needle-to-plane electrode configuration was used in this system, and the need electrode was electropolished with a 5 μm radius. The time resolution of the Schlieren images is 5 ns because the pulse width of the YAG laser is 5 ns. Schlieren images of the streamers in different phases are shown in Figure 1.6, and the traces are shown in Figure 1.7. In this study, Furusato observed that there are more streamer branches in supercritical CO_2 than in liquid CO_2, and there are more branches in liquid CO_2 than in gaseous CO_2.

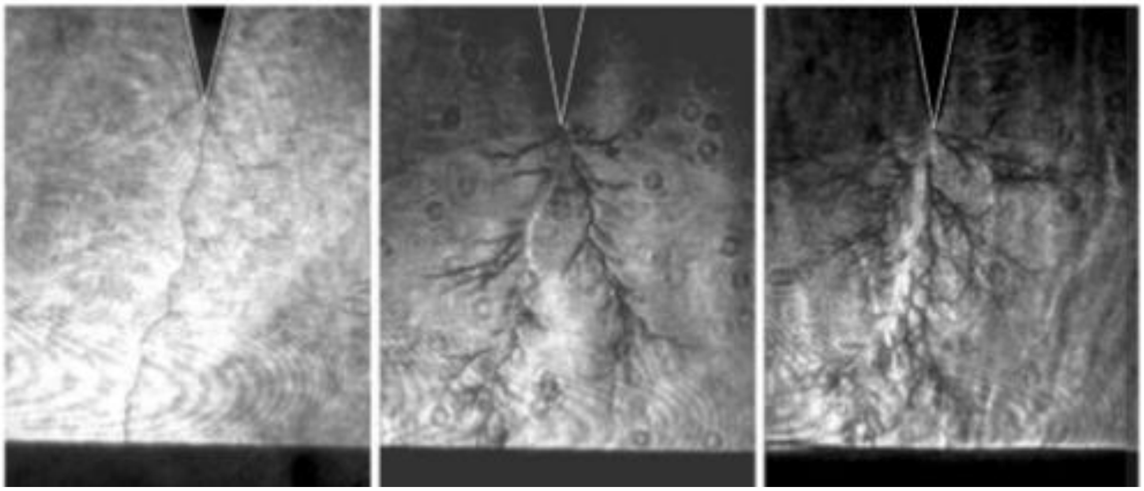

Figure 1.6 Positive prebreakdown streamers. a: gaseous, T: 300 K ; P: 0.1 MPa, b: liquid, T: 303 K, P: 10.5 MPa, c: supercritical, T: 307 K, P: 7.5 MPa [12]

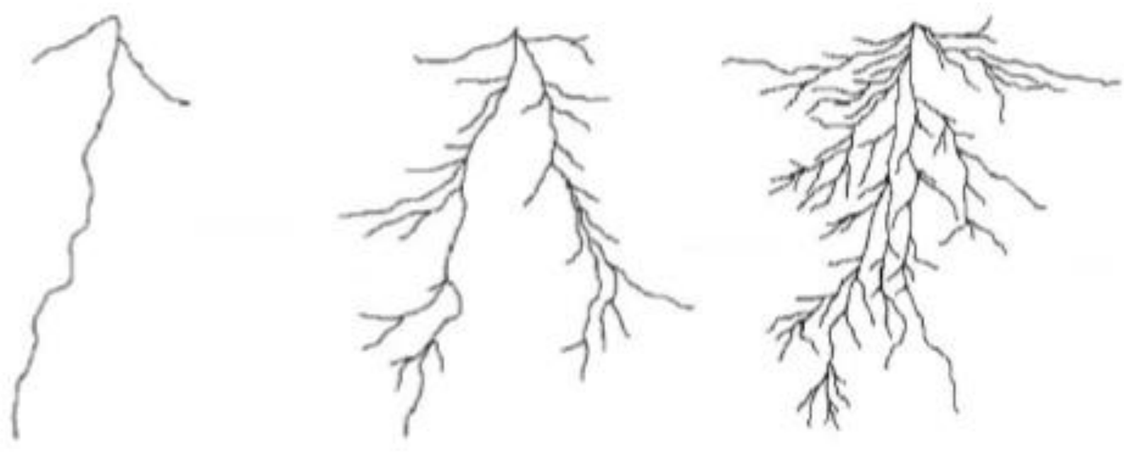

Figure 1.7 Traced images of the obtained Schlieren images: (top) anode; (bottom) cathode [12]

CHAPTER 2

DESIGN AND FABRICATION

2.1 SUPERCRITICAL REACTOR

The SCR was machined from a solid stainless steel 316L cube approximately 4.125” x 4.125” x 4.125”. Holes were bored into each face of the cube. Two holes were for placement of the 1” thick sapphire optical windows. Two holes were created for the inlet and outlet flow of CO_2, and the final two holes were for placement of the electrodes.

Typical supercritical reactor test cells had non-adjustable electrodes [1,10,11,12,13,15]. This means the electrode gap cannot be modified without depressurizing and disassembling the system. To overcome this problem, a high-pressure bellow was included in the reactor arrangement. The bellow is 4 ply of 0.008” thick Inconel 625 and is designed for pressures up to 100 atm with a factor of safety of 2.5. The tightening bolts allow the bellow to translate approximately 2 cm. The bolts are ⅜”-16. This means that every full rotation of the bolts is equivalent to 1/16” translation of the electrode. Figure 2.1 shows the supercritical reactor with the bellow arrangement.

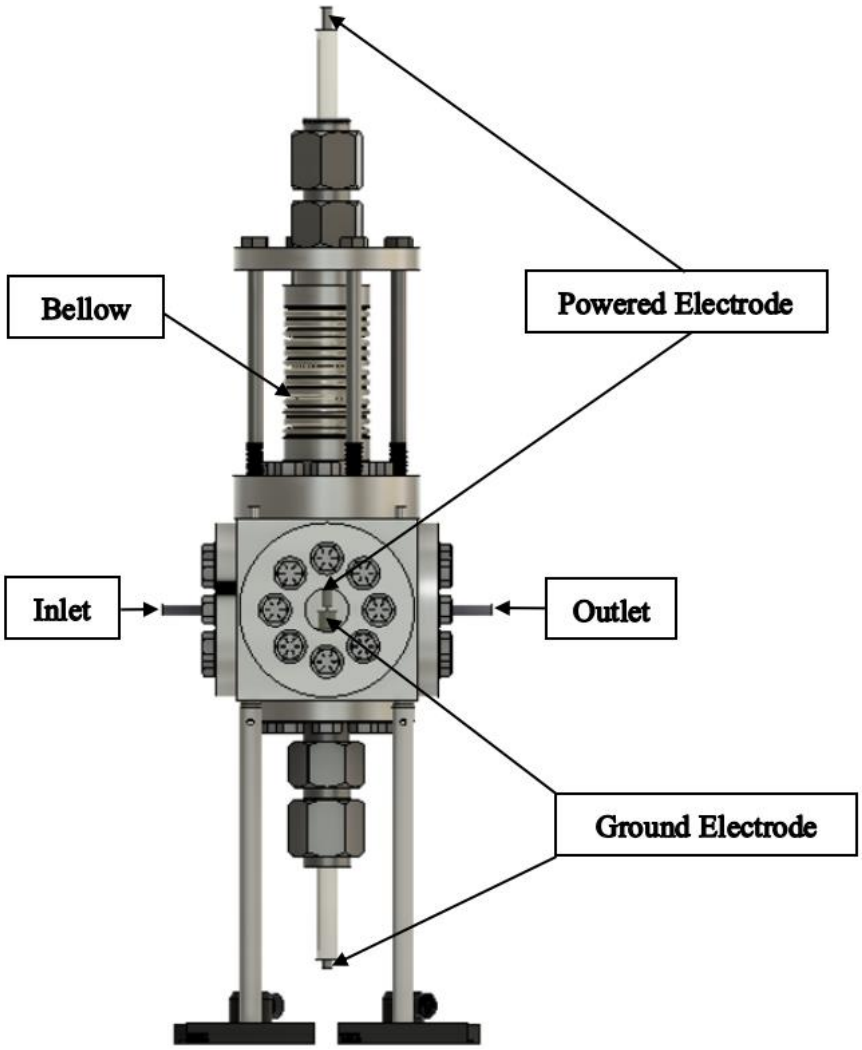

Figure 2.1 Test cell

A positive polarity, 20 kV DC, power supply was used for the experiments. This test cell is designed for micro plasmas with electrode spacing around 10-100 µm. Unlike the work done by Furusato [12,13,15], this reactor could achieve breakdown at much lower voltages due the small electrode gap.

2.2 ELECTRODES

The electrodes being used in this experiment are modified to fit into a high-pressure Conax fitting. The Conax fitting was rated for 8 kV, so it was necessary to make modifications for 20 kV applications. Figure 2.2 shows the original Conax electrode fitting, and Figure 2.3 shows the modified Conax electrode fitting.

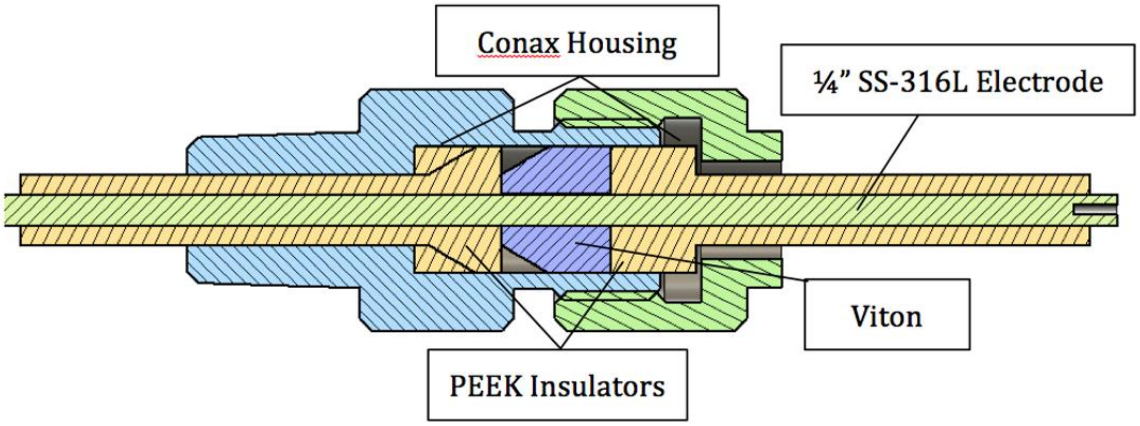

Figure 2.2 High-pressure Conax electrode fitting

The nut in Figure 2.3 was added to the electrode assembly to prevent the electrode from pushing up when pressurized. The Buna o-ring was added to prevent fluid from getting inside the plastic tube. Instead of using a ¼” electrode like shown in Figure 2.3, a ⅛” electrode was used. The ⅛” electrode was inserted into a ¼” nylon plastic tube. This increased the gap between the electrode and the housing. A #27 drill was used to drill a 7 mm hole in the bottom of the electrode to allow for a power connection via banana plug fitting.

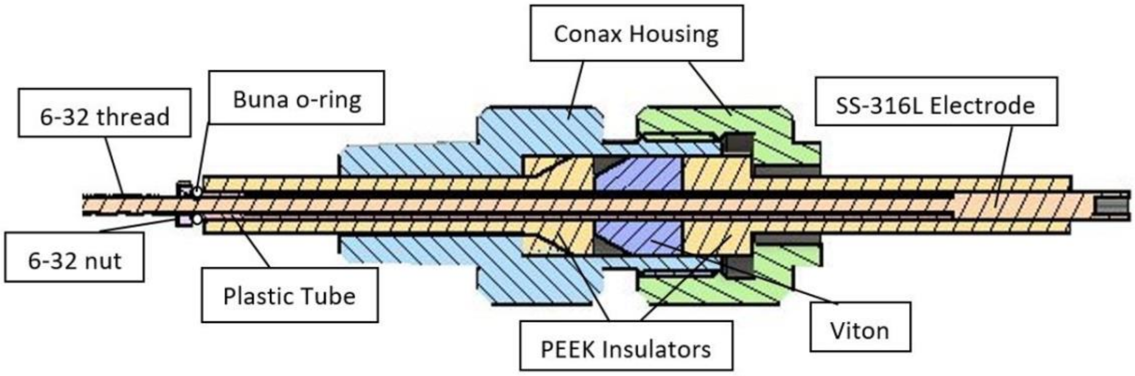

Figure 2.3 Modified high-pressure Conax electrode fitting

The electrode configuration for this experiment is a pin to plane. The pointed electrode had a radius of curvature of approximately 400 µm. This configuration was chosen so that the plasmas would appear in approximately the same location for each pulse. This configuration creates a moderately strong electric field, and the electrode lifetime is longer than that for a pin to plane configuration with a smaller radius of curvature. Discharges happen from the tip of the anode, so it is also very easy to focus the camera on the electrode gap. The anode was given a mushroom shaped geometry. This is so that the diameter of the mushroom head can be measured and used as a reference measurement for radius of curvature and electrode gap spacing. After turning the anode tip in a lathe, it was taken to a Keyence microscope and viewed at 500x magnification for precise geometry measurements. Figure 2.7 shows the anode tip, and Figure 2.8 shows the anode measurements taken using ImageJ software [18].

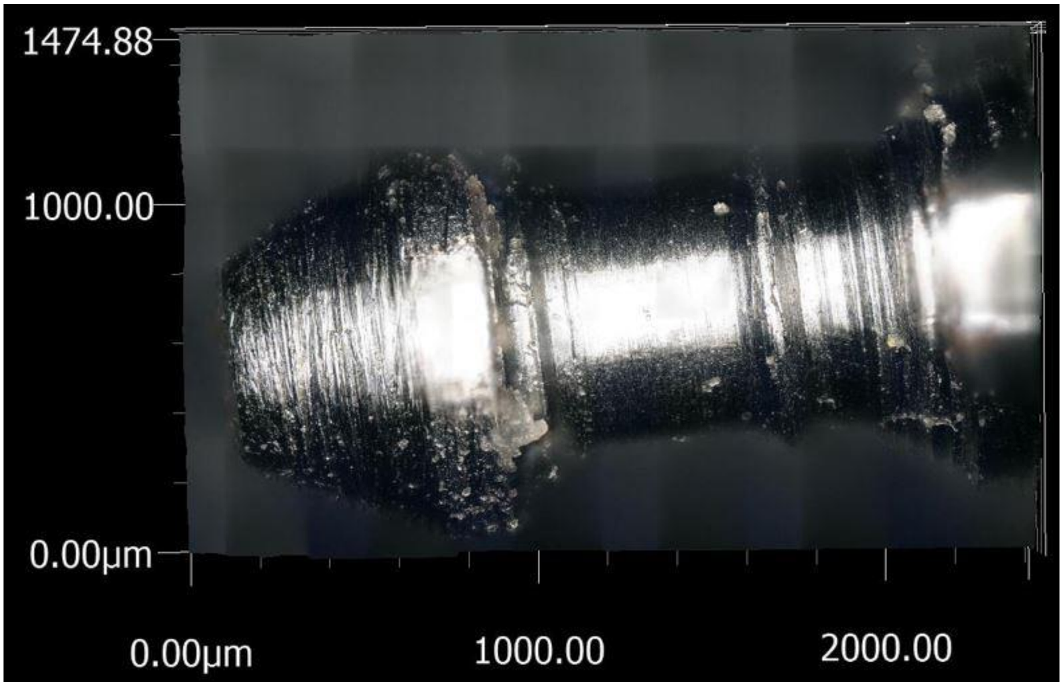

Figure 2.4 Anode tip 500x magnification

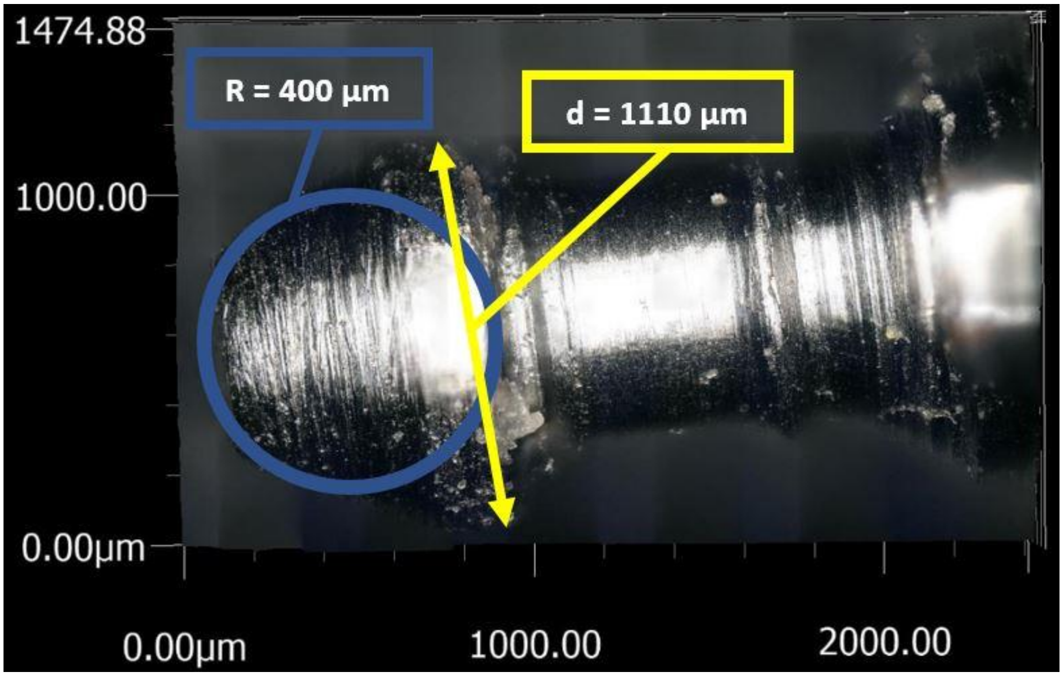

Figure 2.5 Anode tip measurements

2.3 SYSTEM SCHEMATICS

The supercritical reactor is composed of three main systems. The first of which is the plumbing system. The plumbing schematic in Figure 2.6 shows the key elements in the system that are used to create supercritical carbon dioxide.

Supercritical CO_2 is produced by pumping liquid CO_2 through the liquid booster pump until the pressure in the test cell has reached critical pressure. After the test cell has reached critical pressure, some fluid can be vented to remove the air from the test cell. Next, the back-pressure regulator is pressurized to the desired pressure using nitrogen, and then the cartridge heaters are engaged to heat the fluid beyond the critical temperature. During this heating process, CO_2 will be vented out of the back-pressure regulator as the density of the fluid increases. The back-pressure regulator helps ensure that the pressure stays within safe operating ranges.

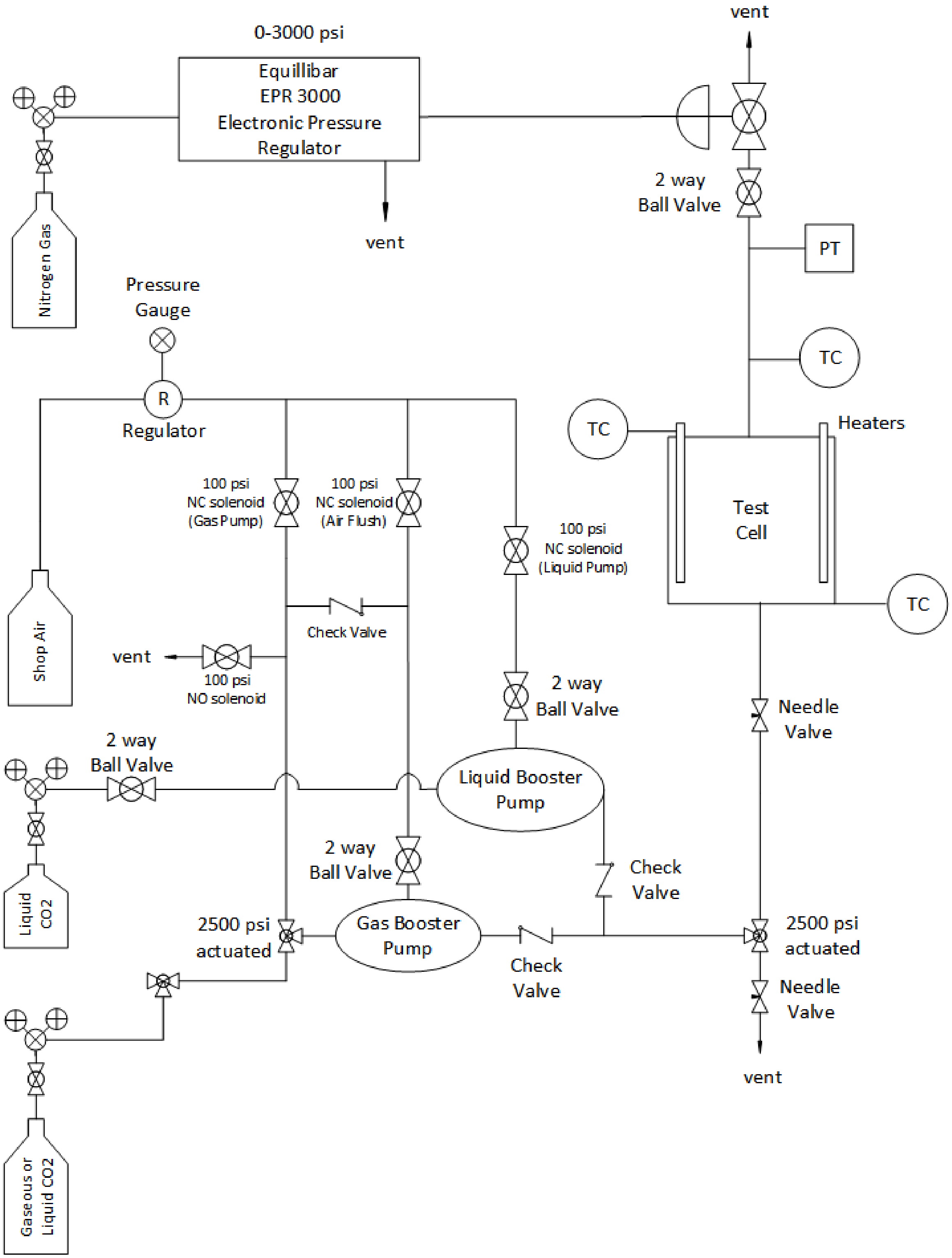

Figure 2.6 Plumbing schematic

An electrical system shown in Figure 2.7 shows the circuitry used to create the plasma and the methods used to record charging current and voltage as well as discharge current.

Two 3.2 MΩ resistors are put in parallel to limit the charging current to below 15 mA. This keeps the power supply from switching between voltage mode and current mode. The power supply current and voltage outputs are monitored using 0-10 V terminals in the back of the power supply. The discharge current is measured using a current transducer and a 20:1 attenuator. This method has proven, so far, to be the safest way to measure high amplitude pulsed current. Kiyan [1], Zhang [8], Bak [19] and Goto [20] each used the current coil to measure discharge current in their experiments.

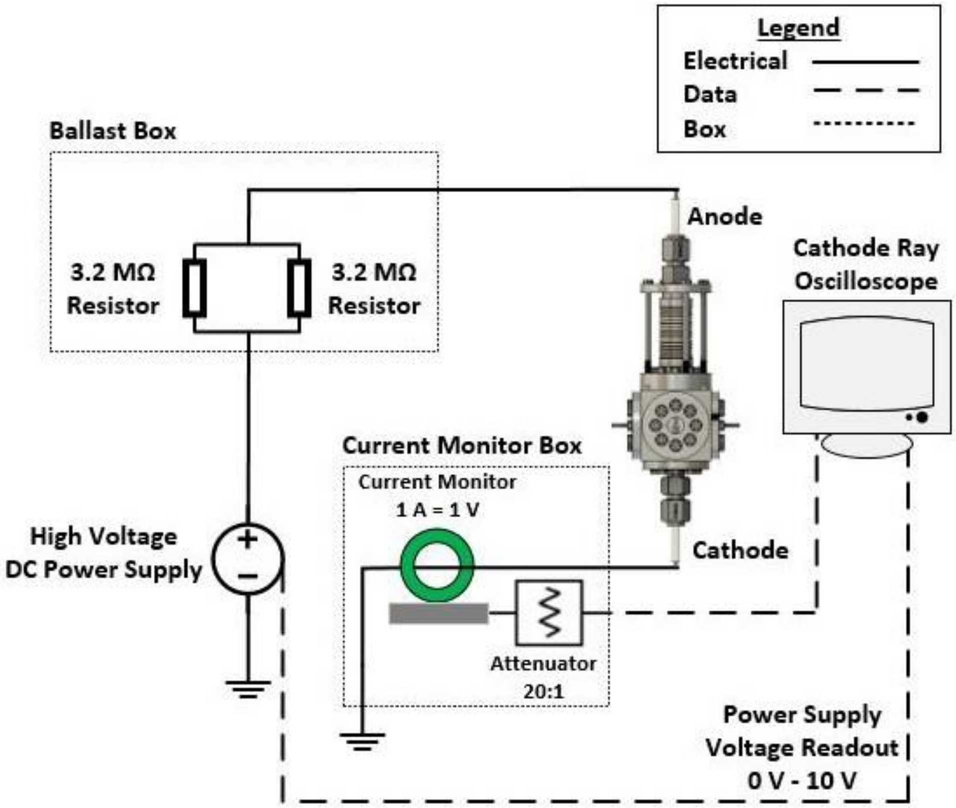

Figure 2.7 Electrical and data schematic

The final system is the controls system. LabVIEW is used to monitor and automate much of the system so that the user can safely operate the reactor from a distant location. A detailed schematic of the controls system is shown Figure A.1 in Appendix A, and the LabVIEW programming is shown in Appendix B.

2.4 ELECTROMAGNETIC PULSE SHIELDING

Shielding electrical components is a crucial element of this system. All wires carrying data are shielded either with tin or stainless-steel braids, or they are shielded with aluminum or copper foil. Shielding efficiency increases with DC conductivity [21]. It is important that the shields of these wires are grounded so that the current picked up in the shields has a place to flow. There are 3 boxes in this system that are used to protect sensitive components from electromagnetic interferences (EMIs) or strong electromagnetics pulses (EMPs). The first box contains the ballast resistors. It is very important to place a thick layer of insulating material between the ballasts and the box so that the ballasts do not arc and conduct electricity to the box. Another box used in the system is the current monitor box. The current monitor box is used because unshielded wires run through the current monitor, and the metal box is used to protect sensitive equipment located outside the box from EMIs. It is important to note that shielded, high voltage cable is used outside the boxes, and unshielded wire is used inside the boxes. The shielded, high-voltage cable is rated for 100 kV DC. The shields of these high-voltage cables are connected to the metal electrical boxes via conduit fittings and to the test cell so that the entire circuit is shielded. The boxes and the braided shields mitigate electromagnetic noise, and they must be connected to ground.

2.5 BOOSTER PUMPS

This setup has two booster pumps and two automated 3-way ball valves. The gaseous booster pump is used for air flush or gaseous CO_2 experiments up to 50 atm. There is an automated 3-way ball valve connected to the inlet of the gas booster pump that allows the user to pump either CO_2 or air into the inlet of the pump. The liquid booster pump is used to pump high-pressure liquid CO_2 into the test cell. These pumps each have built-in inlet and outlet check valves. There are secondary check valves downstream of the pumps, and they are connected to a tee fitting. This tee fitting is connected to an automated 3-way ball valve that is used to either direct the flow towards the test cell, vent the flow, or block all flow. This is all shown in Figure 2.8.

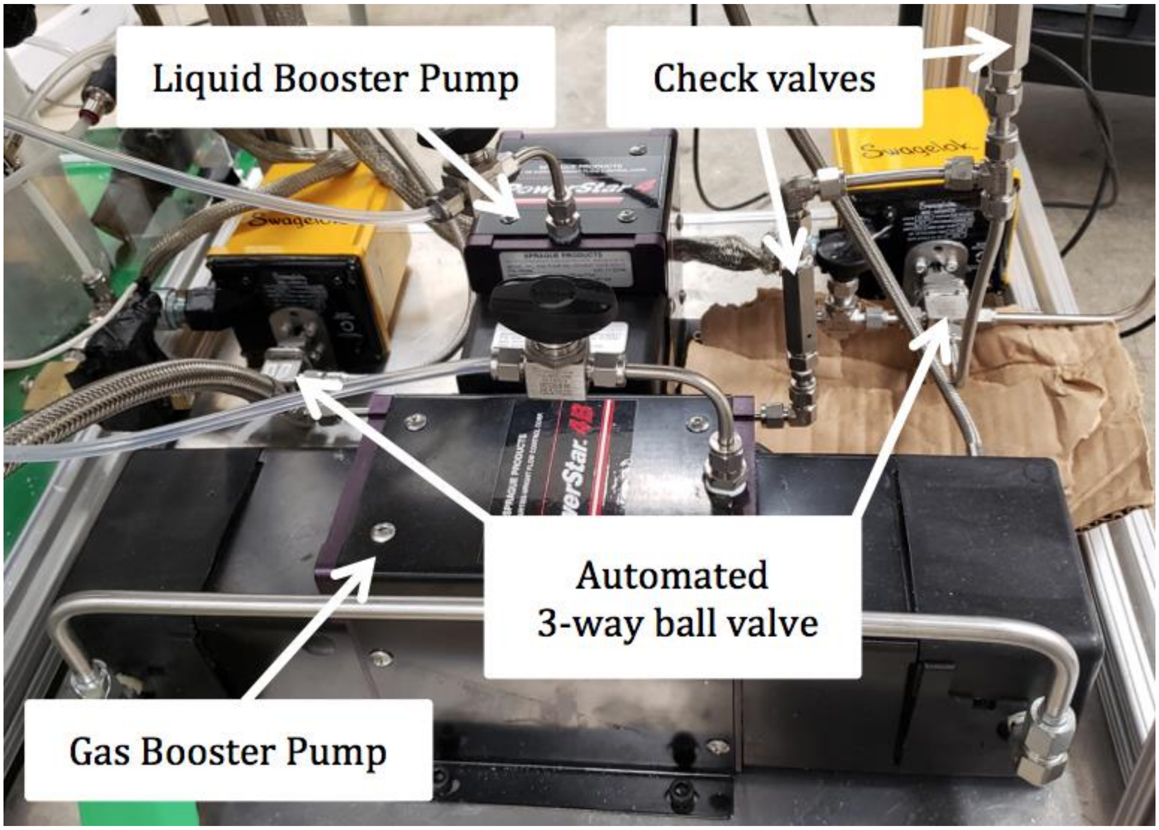

Figure 2.8 Booster pumps, automated ball valves, and check valves

2.6 OPTICAL EMISSION SPECTROSCOPY

Two different setups are used when performing optical emission spectroscopy. The first setup uses the Ocean Optics HR4000 spectrometer. This spectrometer shows a wide range of wavelengths between ultraviolet and near infrared. This setup has a 0.5 nm optical resolution and is used to get a general idea of the spectra emitted. The spectrometer is a small box that is connected to a computer and also connected to a 2-meter fiber optic cable. This cable has a lens on the end. The lens needs to be aimed at the plasma, and it needs to be mounted as close to the plasma as possible. The fiber optic cable and lens can be mounted using an optical mounting post.

The other setup uses a much larger spectrometer called the IsoPLANE SCT 320. This setup also requires the use of a 4Picos ICCD camera. The IsoPLANE spectrometer is used to get detailed images of spectra, rather than a wide field like with HR4000. The IsoPLANE has 3 gratings. The first grating is 600 $\frac{grooves}{mm}$ and has an optical range of 70 nm with an optical resolution of approximately 0.14 nm. The second grating is 1200 $\frac{grooves}{mm}$ and has an optical range of 35 nm with an optical resolution of approximately 0.07 nm. The final grating, which gives the most detail, is 3600 $\frac{grooves}{mm}$ and has an optical range of 10 nm with an optical resolution of approximately 0.02 nm. The 3600 $\frac{grooves}{mm}$ is great for viewing a specific range of wavelengths in great detail, whereas the other gratings are better suited for giving a general idea of the spectra.

A small lens is attached to one end of the optical fiber, and it is mounted and aimed at the plasma. The other end of the optical fiber is connected to the spectrometer. The 4Picos camera is attached to the other end of the spectrometer. The spectrometer and camera each have their own respective softwares. The 4Picos camera uses a spectroscopy software called 4SpecE, and the IsoPLANE spectrometer uses a program called IsoPLANE.

2.7 SCHLIEREN IMAGING

Schlieren imaging is used to show density gradients in the fluid during testing. This imaging technique is also very good for measuring the gap between the electrodes. This setup requires a light source to shine into a concave mirror. The concave mirror collimates the light, and the culminated light shines through the windows of the test cell. Another concave mirror is set up on the other side of the test cell and angled through an arch in the piping. The high-speed camera is aimed between the arch and at the concave mirror. A knife edge is placed between the camera and the knife edge. Shadowgraph imaging can be done using the exact same setup without the knife edge. Figure 2.9 shows the proper way to set up for Schlieren imaging.

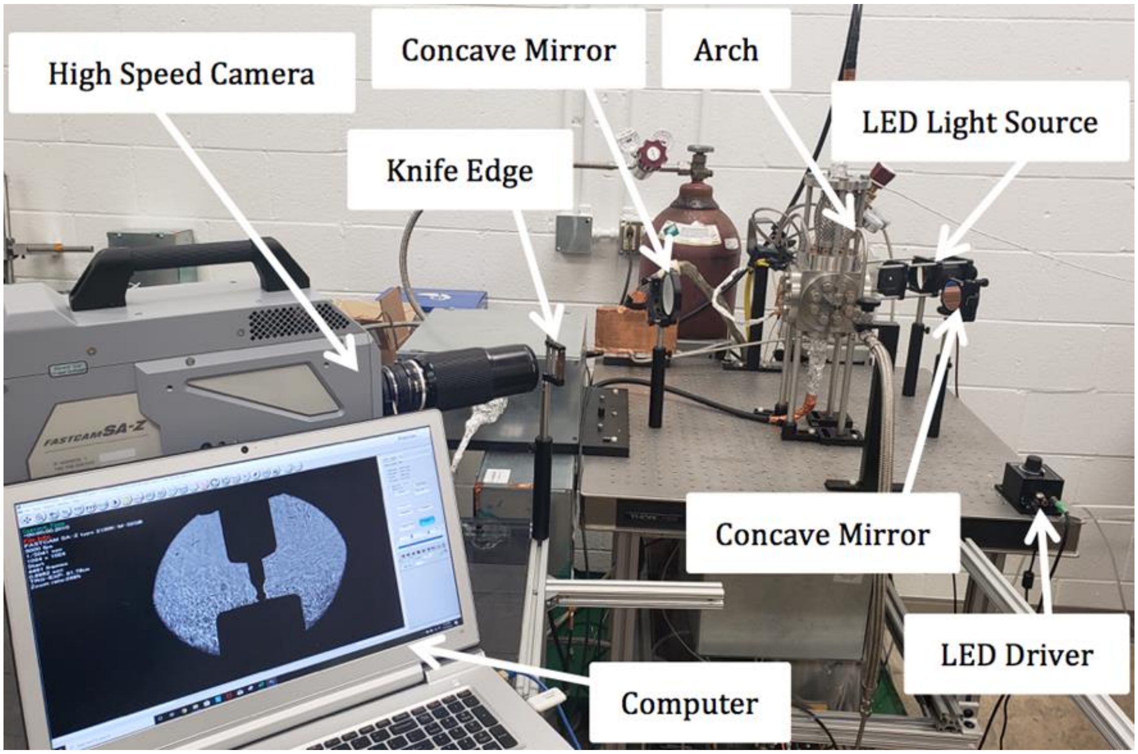

Figure 2.9 Schlieren imaging setup

CHAPTER 3

ANALYSIS

3.1 MECHANICAL PROPERTIES

The test cell is a cube made from stainless steel 316L. Each face of the test cell is approximately 4.125” wide, and stainless steel 316L flanges along with 90 durometer Buna o-rings seal the test cell. However, the flanges on the bellow are stainless steel 304. Grade 8 ⅜”-24 bolts secure each flange to the test cell. The test cell is equipped with two sapphire viewing windows on opposite faces. They are approximately 1.625” in diameter and 1” thick. Sapphire has excellent strength under compression [22]. A simplified model of the test cell was used to analyze the test cell’s structural integrity. The high-pressure bellow was not included in this model since the bellow geometry was complex, and its mechanical properties were given. The manufacturers of the bellow designed it with a factor of safety of 2.5 at 100 atm. The simplified model, Figure 3.1, is shown below. It has 373,157 nodes and 216,178 elements. Analysis was conducted in Fusion360 [23] using the finite volume method. Figure 3.1 shows the safety factor of the test cell when it is pressurized to 75 atm. It shows that the main stress areas are where the bolts are placed. Specifically, the areas with the lowest safety factor are the areas in the cube where the internal threads on one face are close to the internal threads on another face.

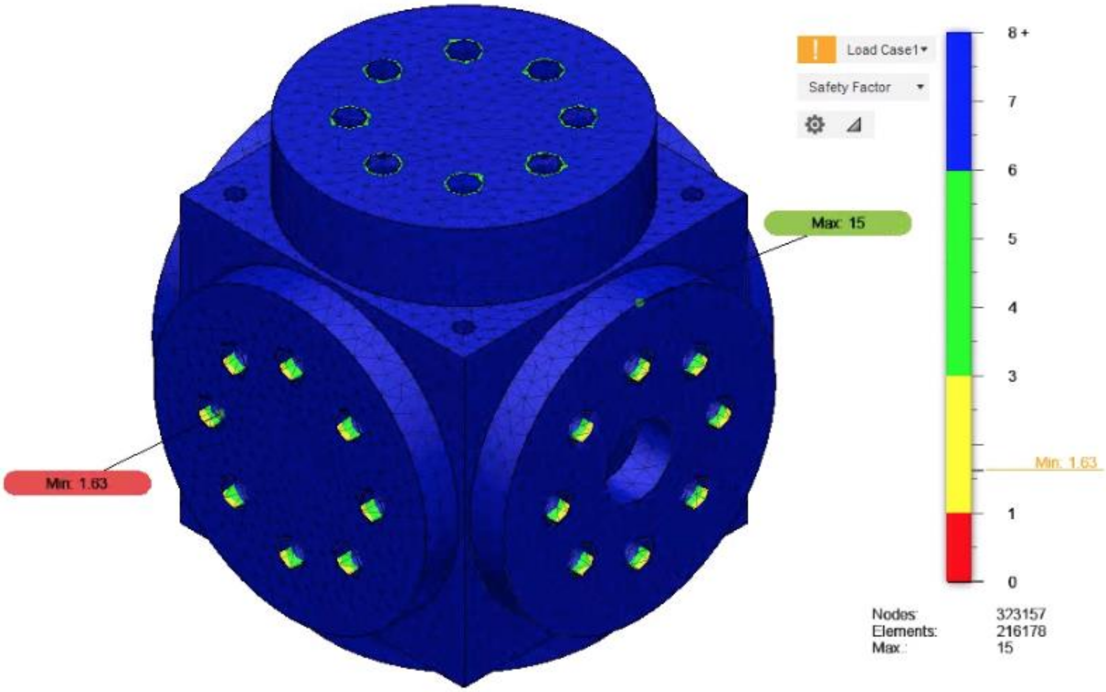

Figure 3.1 Safety factor at 75 atm (full range)

Since the outer faces and flanges of the test cell are at such a high safety factor, we will take a look at the test cell at 150 atm and 300 atm at factors of safety between 0 and 4. We will also look at the Von Mises stress at the weakest point in the test cell at 150 atm and 300 atm.

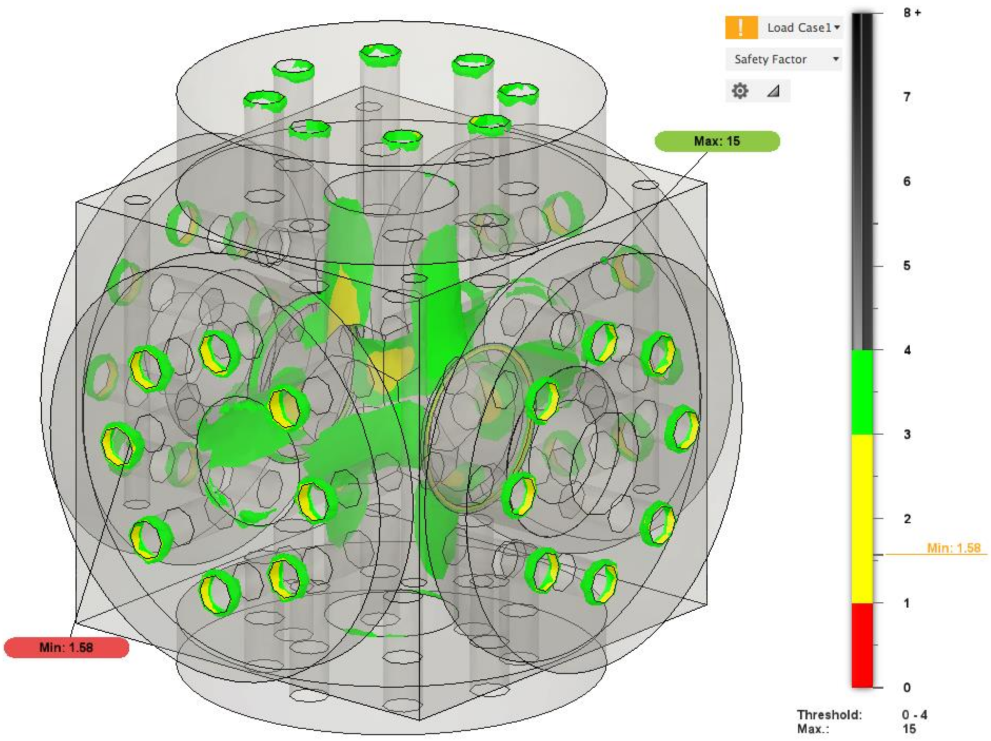

Figure 3.2 Safety factor at 150 atm (safety factor from 0-4)

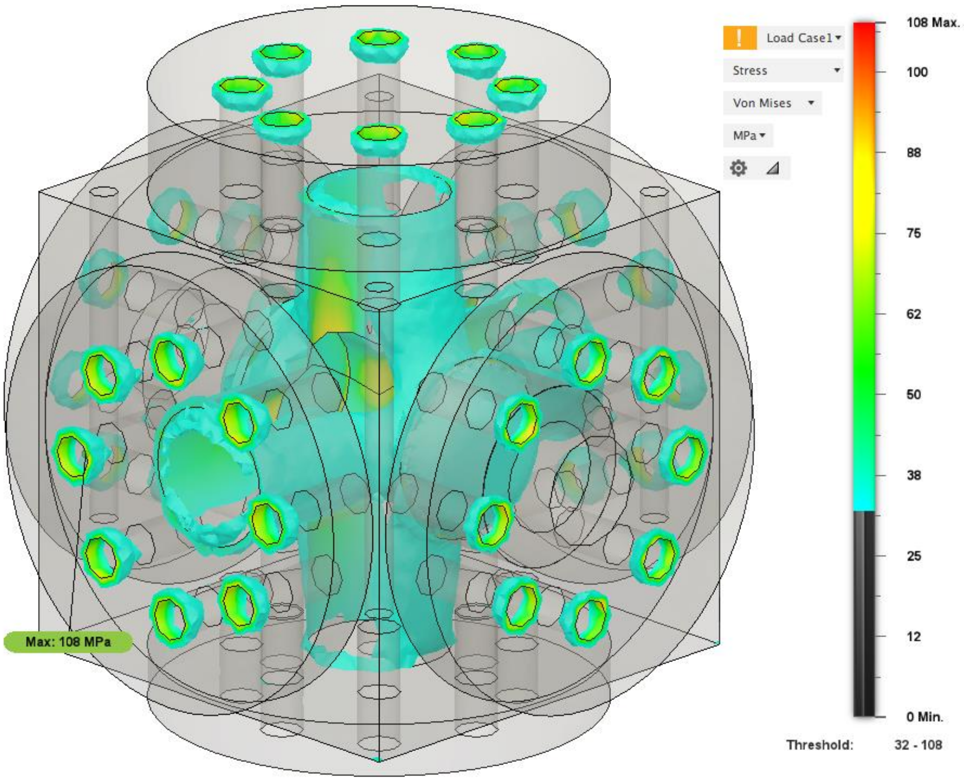

Figure 3.3 Von Mises stress at 150 atm (35 MPa to maximum stress)

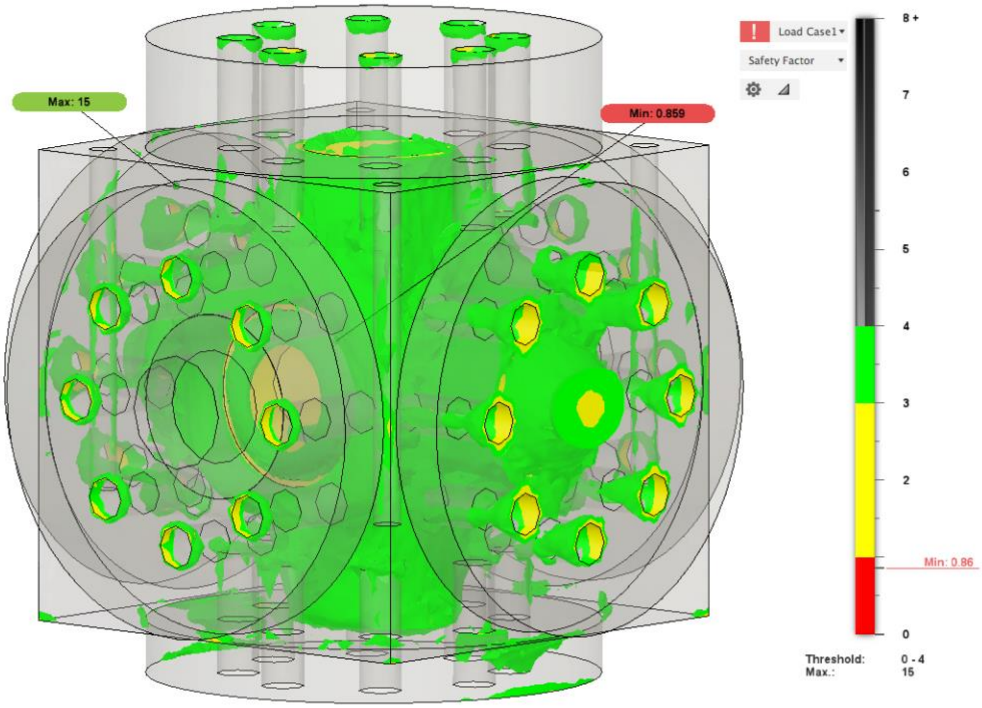

Figure 3.4 Safety factor at 300 atm (safety factor from 0-4)

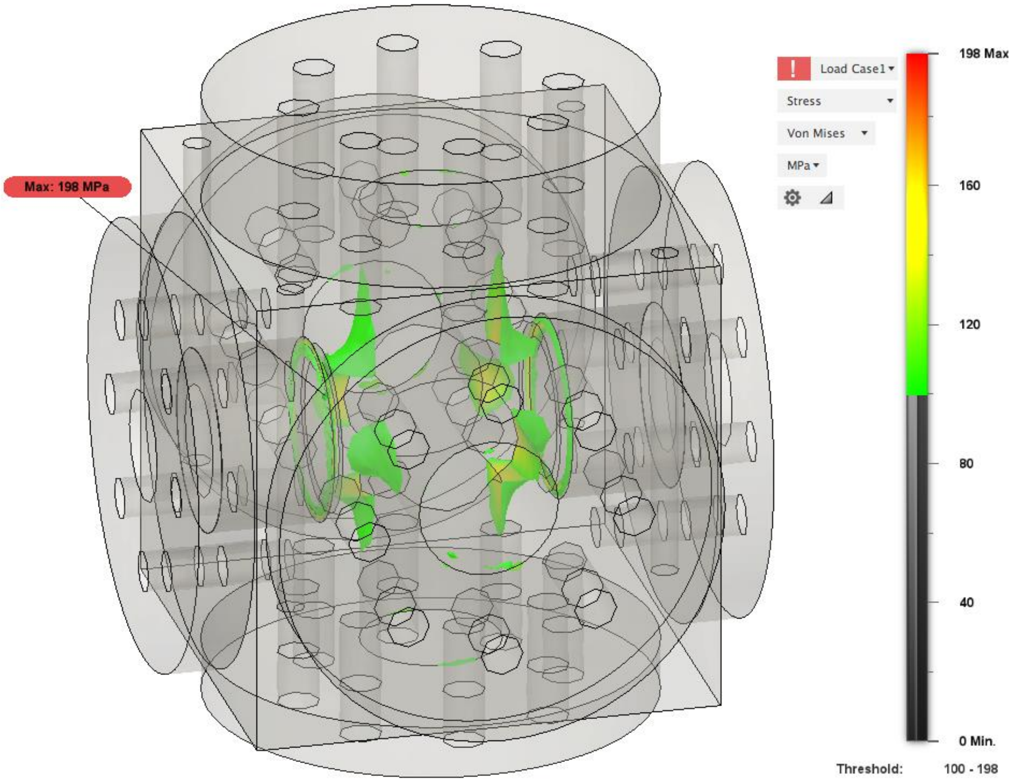

Figure 3.5 Von Mises stress at 150 atm (100 MPa to maximum stress)

3.2 THERMAL PROPERTIES

Transient thermal analysis was conducted in Ansys [24] which uses the finite element method. Transient analysis allows us to see how long it will take the test cell to heat up, and how evenly it will be heated. Since the density of supercritical CO_2 has massive fluctuations with minor temperature changes, it is important to mitigate uneven heating. The three models studied in this section have heat sources applied in different places. Each of these simulations only accounts for conduction through the walls of the test cell and for heat loss to the ambient air. These simulations do not account for heat transfer from the test cell to the CO_2. The mesh created for these simulations has 22,046 nodes and 7,088 elements. The mesh is shown in Figure 3.6.

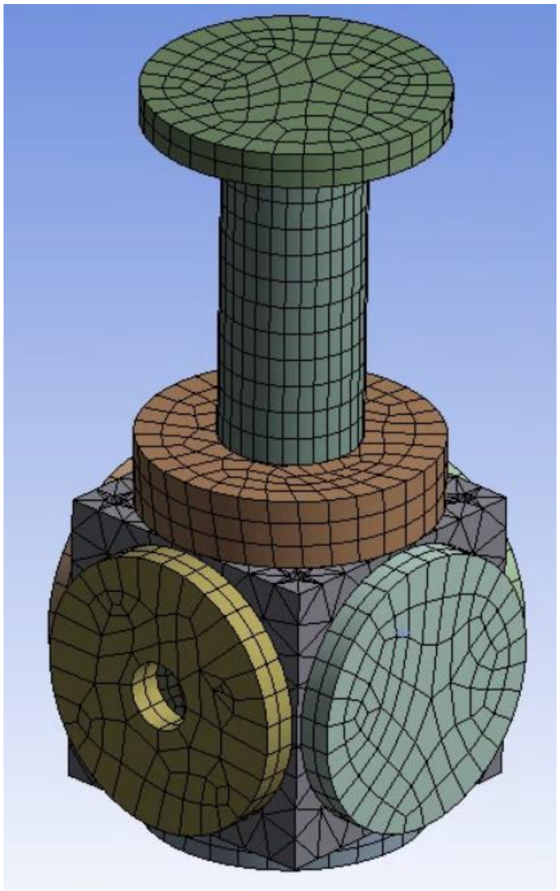

Figure 3.6 Thermal analysis meshing

Three separate simulations were conducted to compare different heating arrangements. Case 1 is the most similar heating arrangement to the current setup. In Case 1, the cartridge heater holes are set at 50°C. This is a safe assumption since the cartridge heaters have built in thermocouples and can be set to 50°C. Case 2 will apply an additional heat source to the outer diameter of the bottom flange at 50°C. Case 3 will apply an additional heat source to the outside of the bellow. Case 2 and Case 3 can be achieved using cartridge heaters in conjunction with heater wraps. Figures 3.7-3.9 show the initial conditions and where the heat loads are applied for each case. These figures show the temperature change of the test cell at times of 20 minutes, 40 minutes, and 60 minutes. Figures 3.7-3.9 also show the locations of the temperature probes. One temperature probe is located at the top, center of the bottom flange, and the other probe is located at the bottom center of the top flange. The data from the temperature probes is shown in Figure 3.10.

There are three boundary conditions for each case. A convection boundary condition was given to the outer surfaces of the test cell to simulate heat loss to the ambient air. This boundary condition is shown in equation 1. The boundary condition of the heated faces was a constant temperature boundary condition at 50°C. The boundary condition inside the test cell was an insulated boundary condition. This third boundary condition does not match the actual physics of what is happening in the experiment. But it greatly simplifies the problem, and still gives satisfactory results.

$$\mathrm{T}_\infty = 25^\circ\mathrm{C} \text{ and } \mathrm{h} = 10\,\frac{\mathrm{W}}{\mathrm{m}^2\mathrm{K}} \qquad -\mathrm{k}\frac{\mathrm{dT}(0,\mathrm{t})}{\mathrm{dx}} = \mathrm{h}[\mathrm{T}_\infty - \mathrm{T}(0,\mathrm{t})] \tag{5}$$

$$-k\,\frac{\mathrm{dT}(0,\mathrm{t})}{\mathrm{dx}} = 0 \tag{6}$$

Case 1

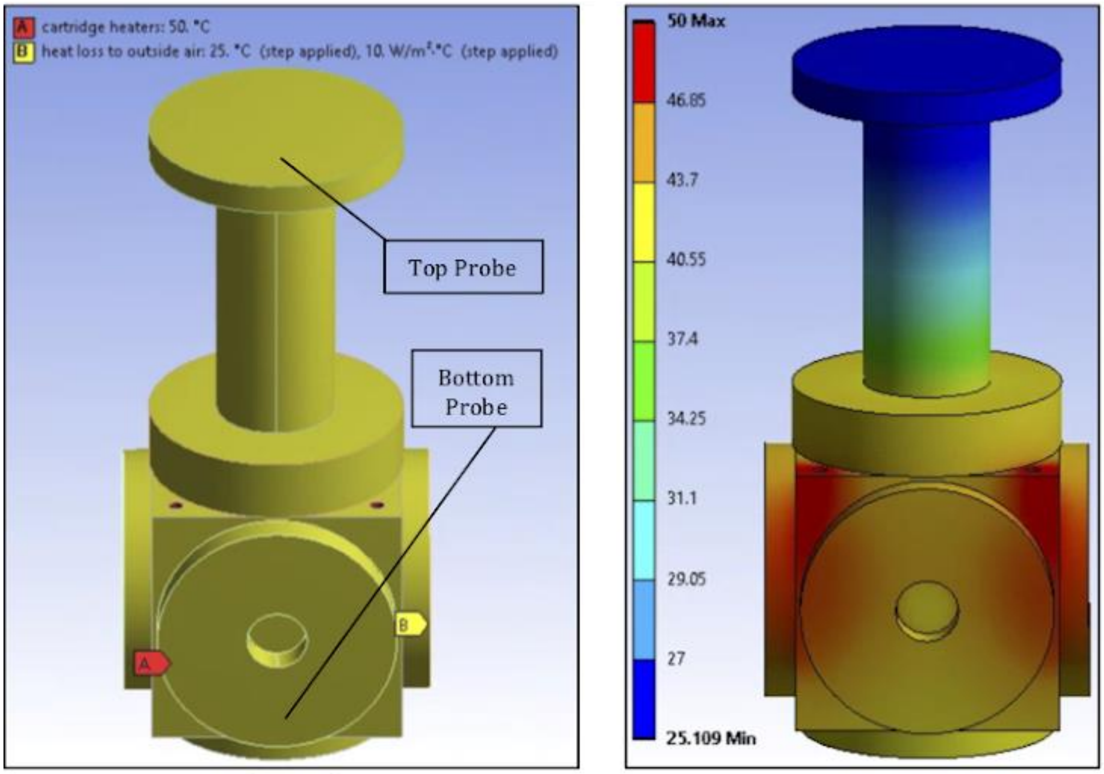

Initial condition

time = 20 minutes

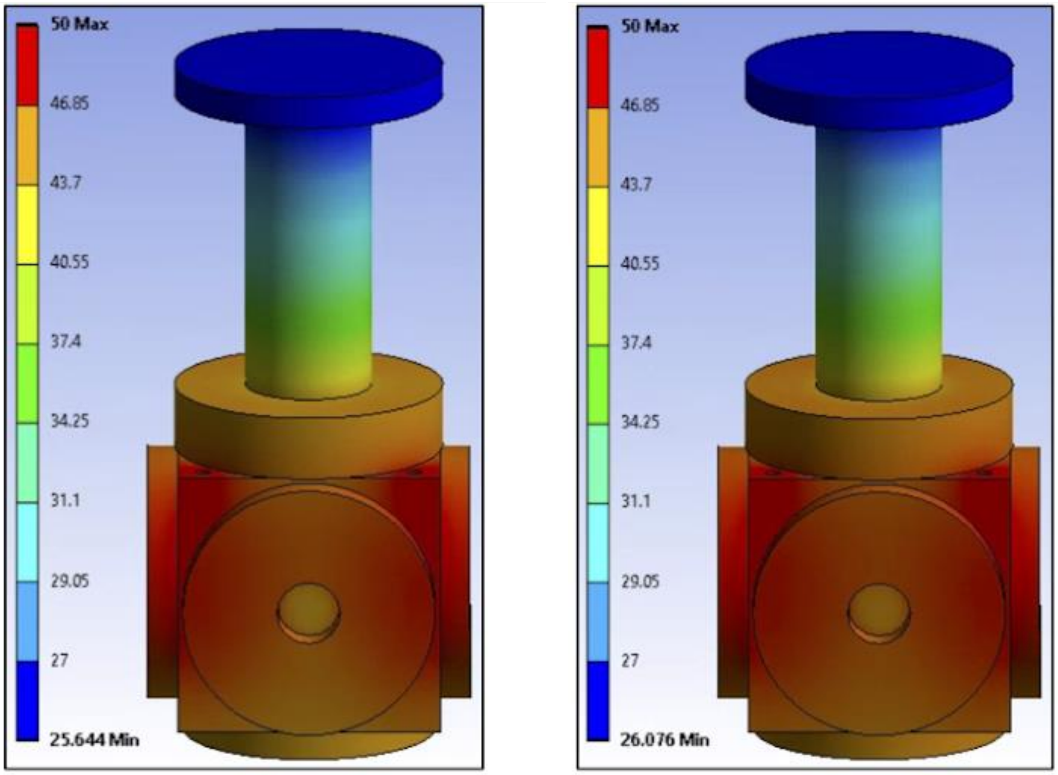

time = 40 minutes

time = 60 minutes

Figure 3.7 Heating (case 1)

Case 2

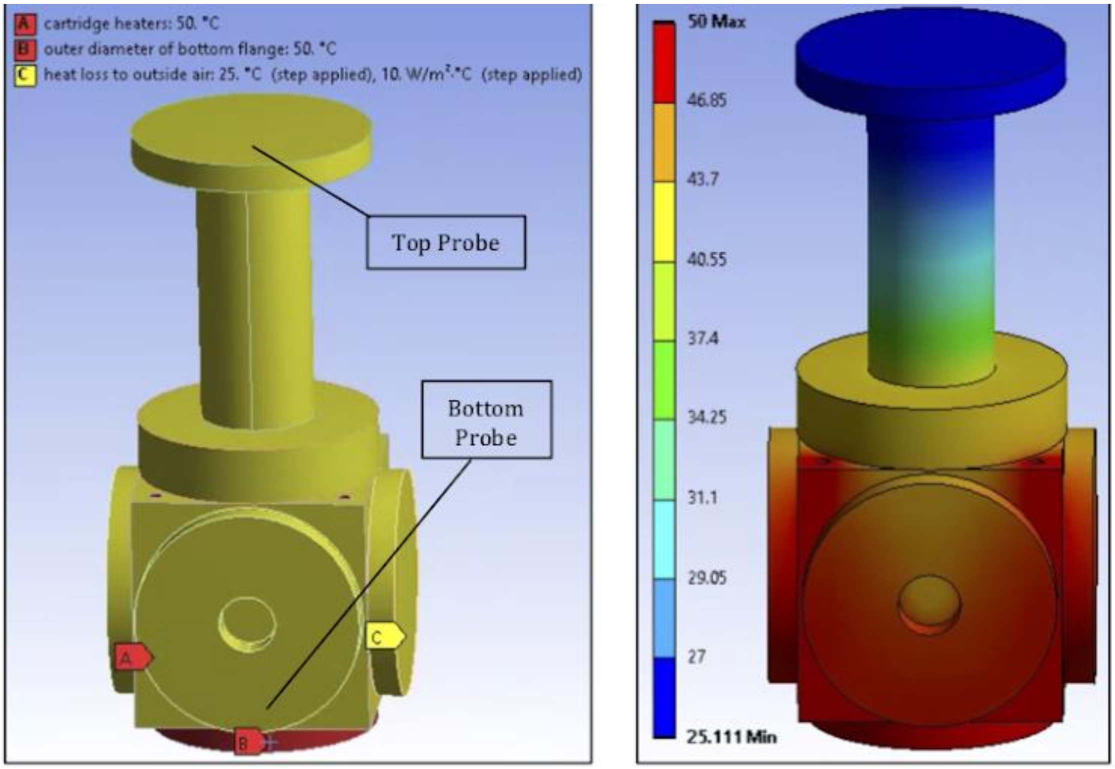

Initial condition time = 20 minutes

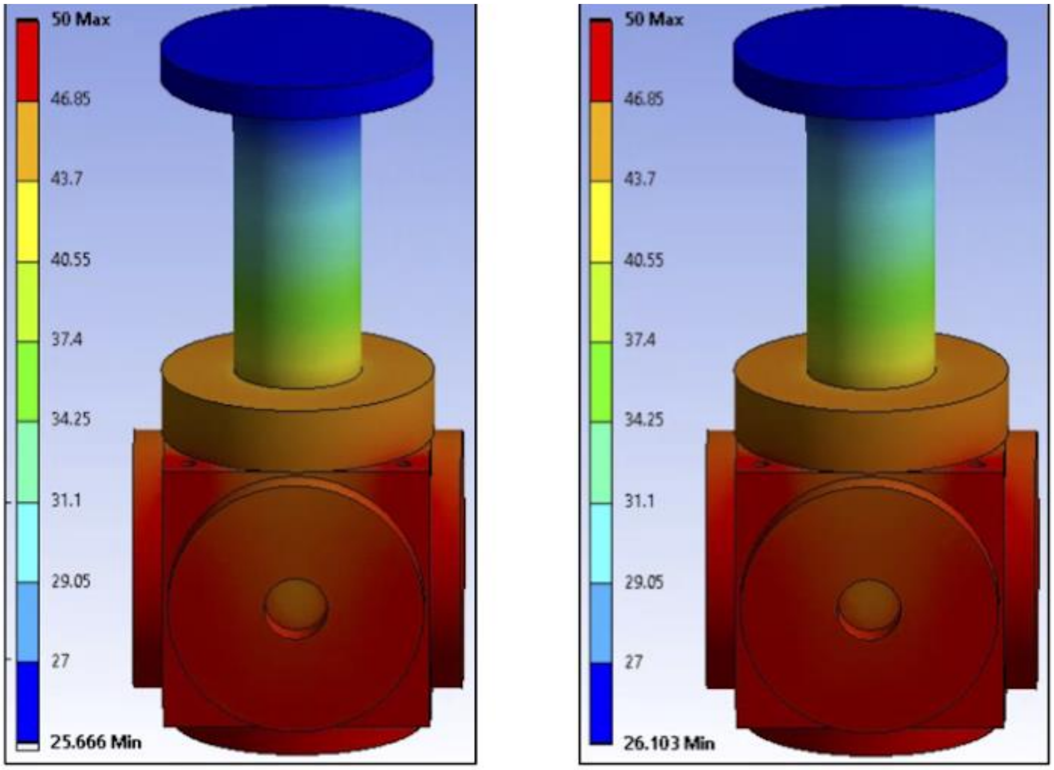

time = 40 minutes time = 60 minutes

Figure 3.8 Heating (case 2)

Case 3

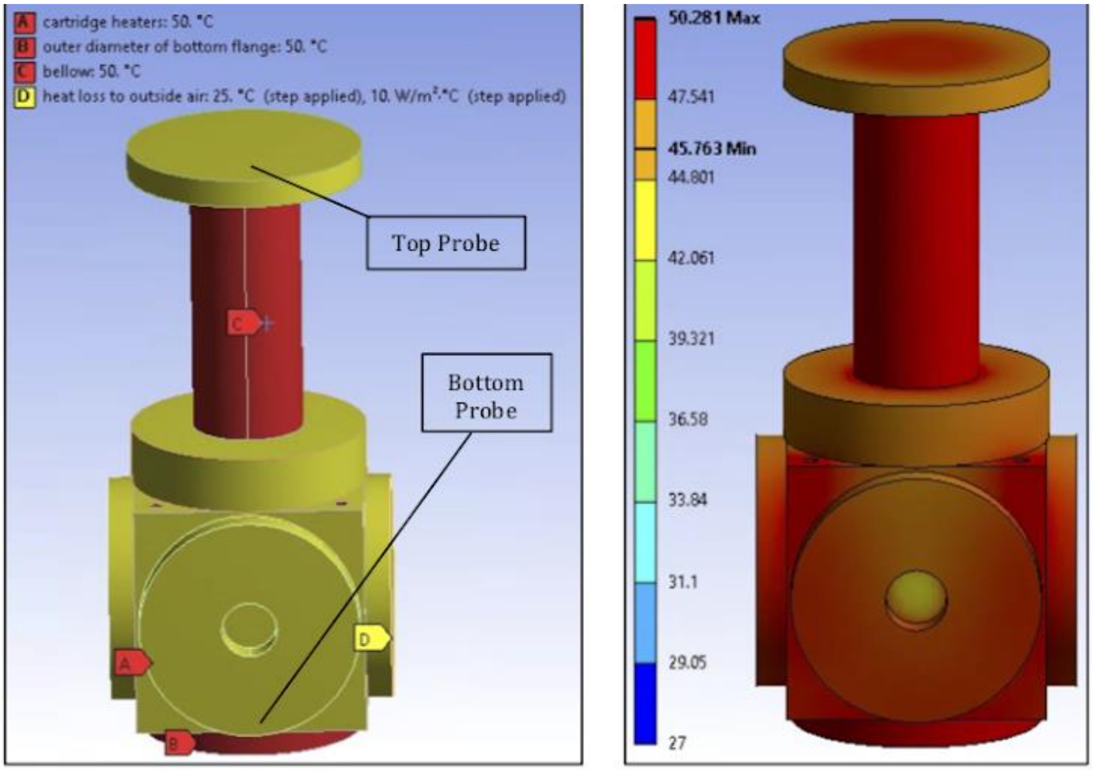

Initial condition time = 20 minutes

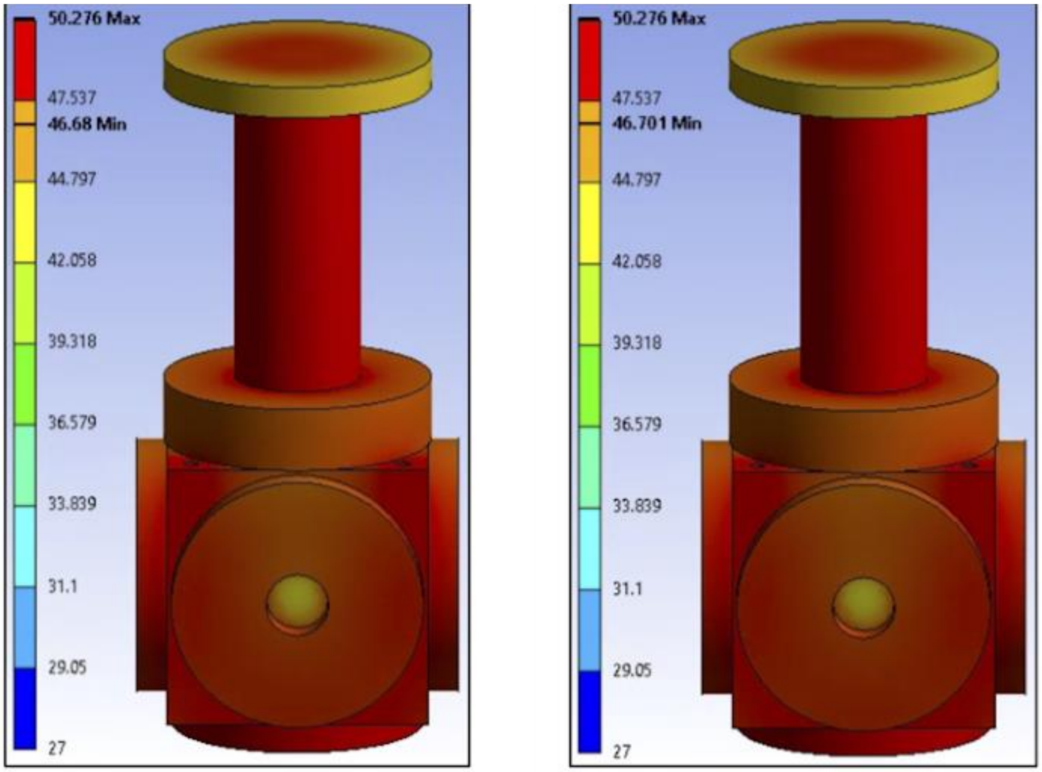

time = 40 minutes time = 60 minutes

Figure 3.9 Heating (case 3)

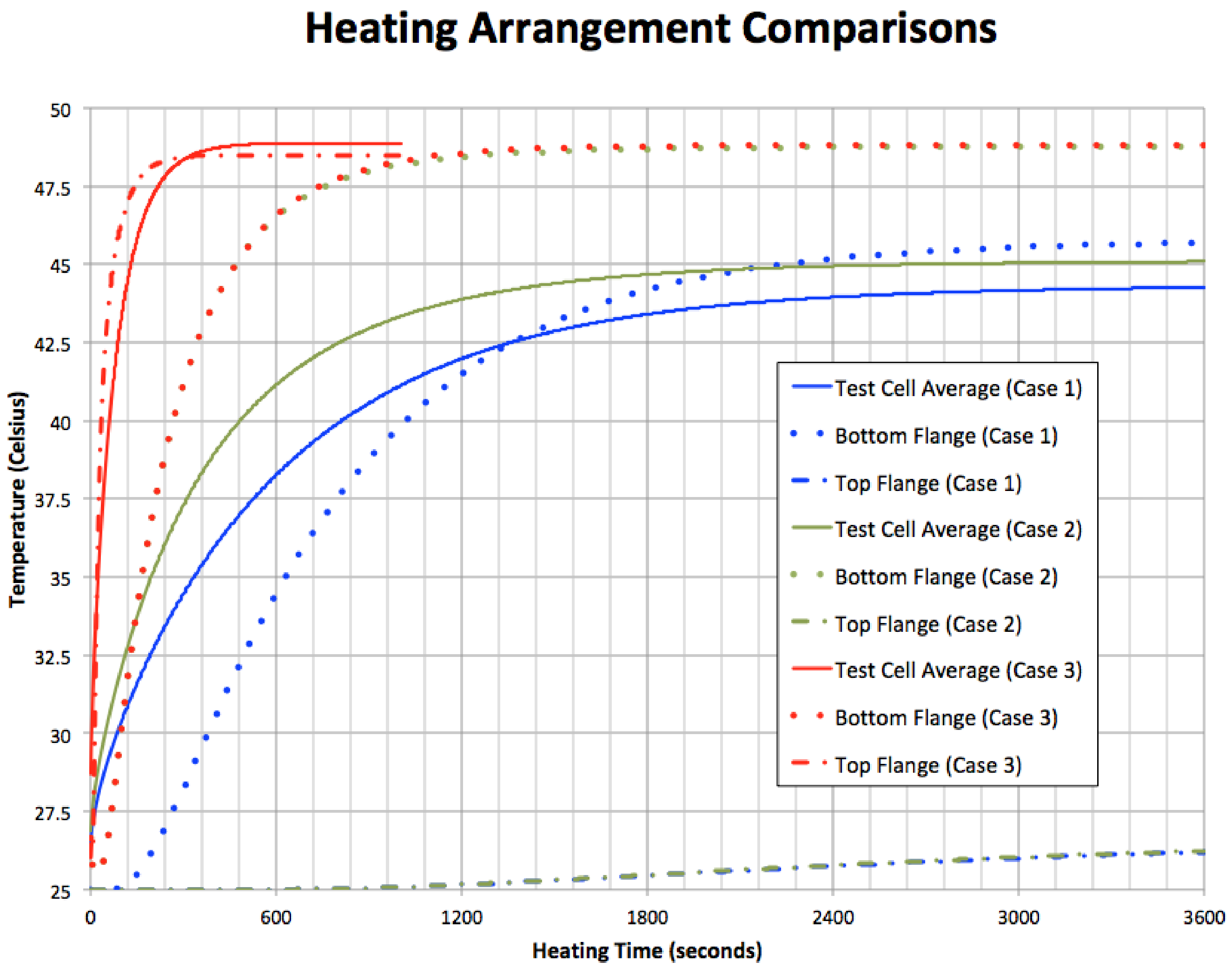

Figure 3.10 Heating arrangement comparison plot

CHAPTER 4

RESULTS AND DISCUSSION

4.1 EMP CHALLENGES AND STRATEGIES TO OVERCOME

High-pressure discharges caused the electrodes to behave like capacitors until breakdown was achieved. This meant that they could build charge and then have a high-current pulsed discharge. Preliminary tests with the supercritical reactor showed that these pulsed discharges were causing the DSLR camera and the DAQ cards to malfunction. This was likely due to EMPs created by a short burst of high oscillating current similar to the waveform shown in Figure 4.8. These pulses would turn the camera off, and they would zero the DAQ cards. A current output card, and a current input card were damaged by these pulses even though they were not wired into the system at the time.

It is believed that a large magnetic field was produced during these pulses, and the magnetic field induced a high current into the DAQ card channels. It was observed that the channels with wires in them were more susceptible to being damaged. This is true even if the cards were not powered on or connected to the chassis. These pulses were able to damage equipment on the outer perimeter of our lab space (20 ft away). It is possible that the EMP could have reached farther than 20 feet. After discovering that EMPs were created by this reactor, precautions were taken to shield and contain these pulses.

The electrical schematic of the system is shown in Figure 2.7. The electrical cables in this system are 100 kV DC, shielded cables. These cables have a thick insulating layer around the conducting core, and they have a braided metal shield around on the outside of the insulating layer. Figure 2.7 also shows that there are electrical boxes in the circuit. These boxes contain large components such as the resistor ballasts and the current monitor. The boxes act as shields, and they and connected to the shields on the high voltage wire. There are no breaks in the shield circuit, and the shield is grounded to a solid earth ground. This strong earth ground connection was shown to greatly reduce the strength of the EMPs. However, EMPs can still affect the electronics in the system if the current on the power supply is turned up high enough to create rapid pulsing plasmas.

Extra precautions were taken to shield the 8-slot chassis and DAQ cards from electrical noise and EMPs. The chassis and the DAQ cards were placed in an electrical box that is also connected to a solid earth ground. All wires connected to the DAQ cards are shielded wires that are fed through holes in the box. The shields of these wires are connected to the box, and the conductive cores are connected to the DAQ cards.

4.2 CHARACTERIZATION OF PLASMA IN AIR

Air was used as the working fluid for preliminary tests. A discharge voltage versus current plot is shown in Figure 4.1 for air plasmas at 1 atmosphere and at 5 atmospheres. Pictures of the plasmas were taken using a DSLR camera and a microscope. This data was recorded with a pin to plate electrode configuration, and the electrode gap is approximately 1.14 mm. Figures 4.2 and 4.3 show the plasma stretching from the anode at the bottom to the cathode at the top.

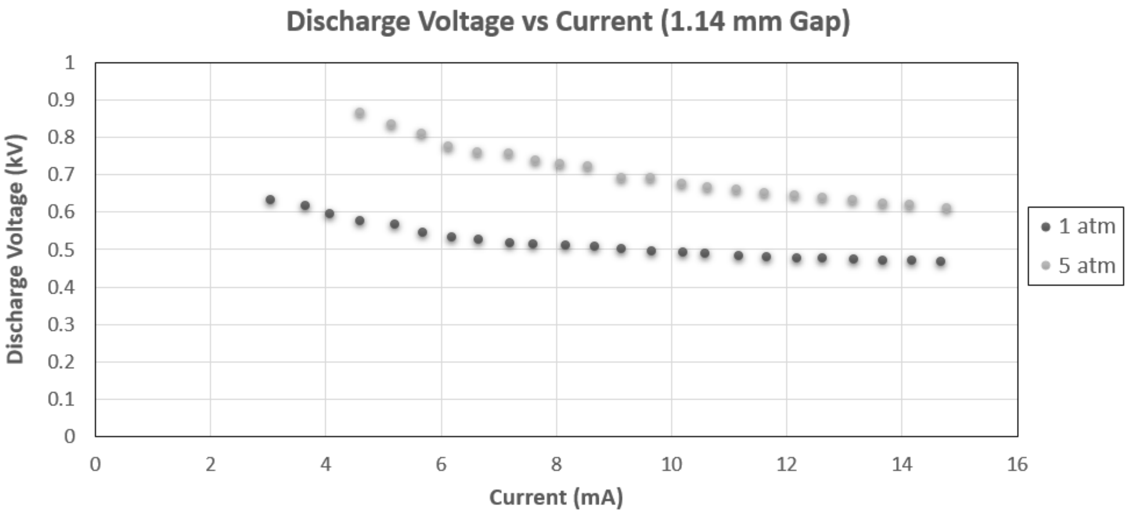

Figure 4.1 Voltage versus current characteristics of an air plasma operating at 1 and 5 atm pressure. Interelectrode separation = 1.14 mm

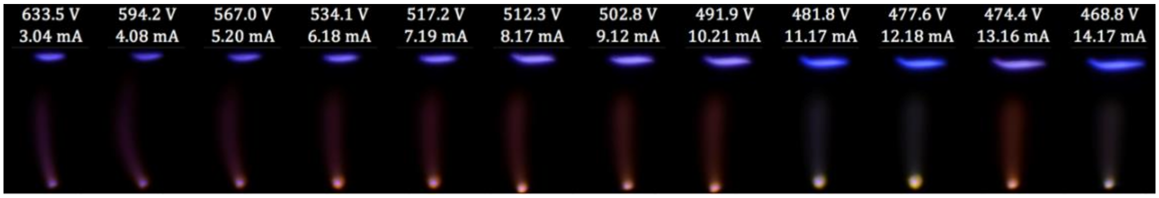

Figure 4.2 Air plasma (1 atm)

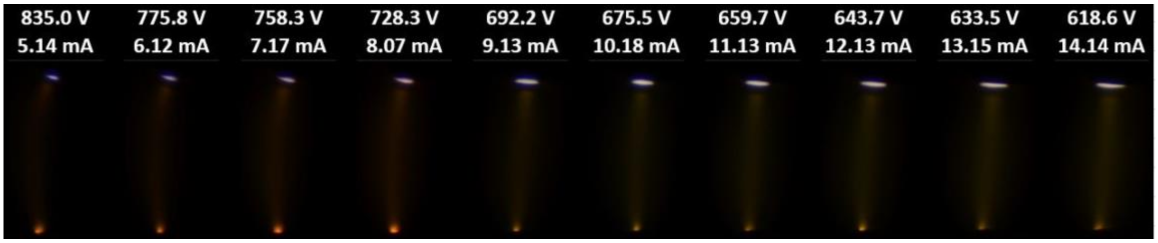

Figure 4.3 Air plasma (5 atm)

Attempts at achieving normal glow discharge in high-pressure (15+ atm) air were made. Discharge voltage and current were not measured for the higher-pressure tests. As the pressure increases, the plasma becomes whiter. This change can even be seen in Figures 4.2 and 4.3. The higher-pressure plasmas also tend to sputter and be less stable than the lower-pressure plasmas. In high-pressure plasmas the positive column can bend and break, causing a complete electrical discharge. This discharge creates an electromagnetic pulse (EMP), and it can damage sensitive electronics or interfere with readings. Shielded cables with a good ground connection were used after the discovery of EMPs.

Optical emission spectroscopy was conducted using the IsoPLANE SCT 320 on air plasma at atmospheric pressure and at 4.4 atm for the wavelengths 315-385 nm.

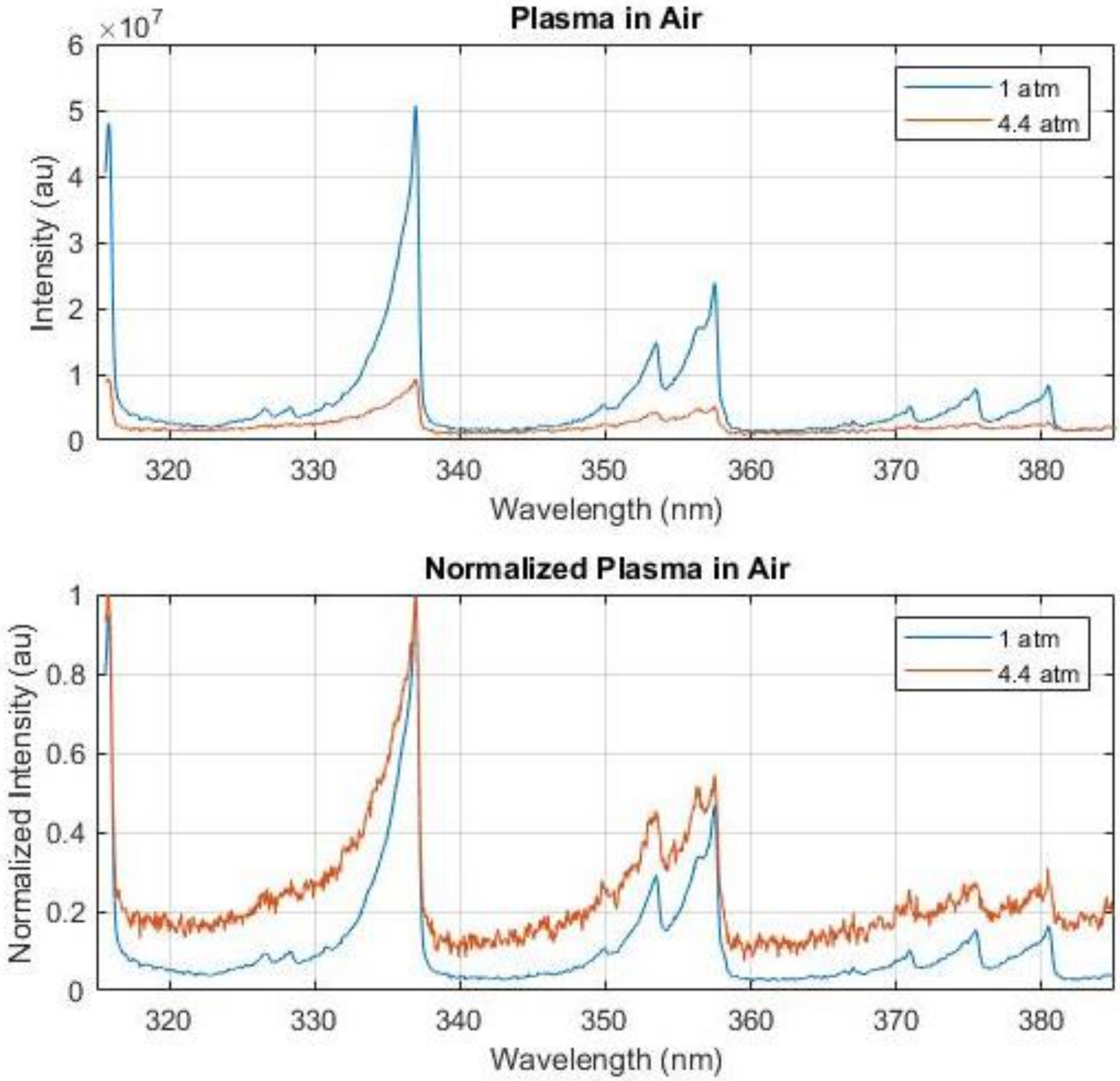
Plasma in Air

Normalized Plasma in Air

Figure 4.4 Air plasma optical emission spectroscopy 315 – 385 nm

A closer look was taken at the plasma using the 3600 $\frac{grooves}{mm}$ grating in the spectrometer that looked at the wavelengths between 334-338 nm. This area focuses on nitrogen peaks that can be used to determine the plasma translational, rotational, and vibrational electron temperatures. A current of 15 mA and an electrode gap of 1 mm was used for these measurements.

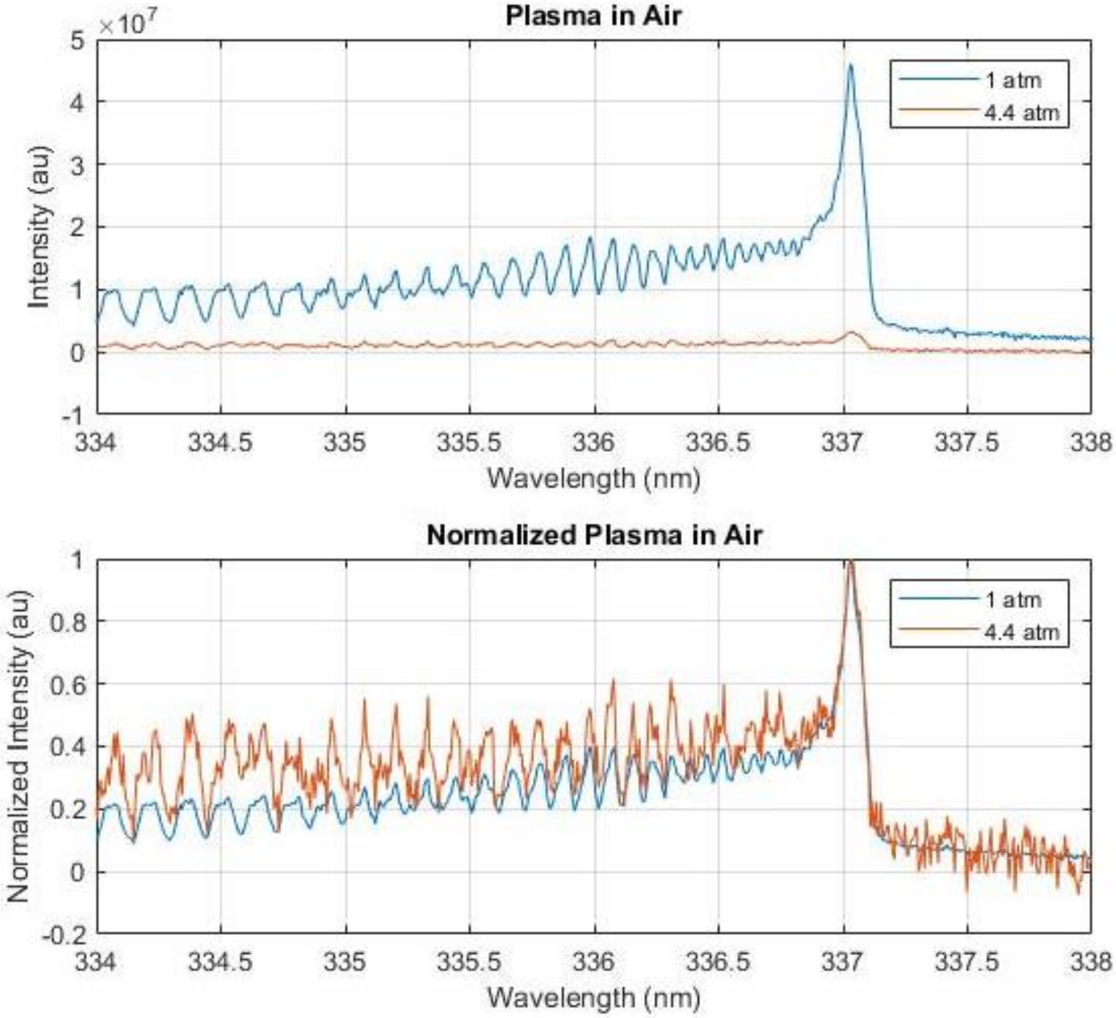

Figure 4.5 Air plasma optical emission spectroscopy 334 - 338 nm

The intensity of the signal drops as pressure is increased. This is likely due to a smaller cathode glow in high-pressure, normal glow plasmas. The purpose of this experiment was to find the nitrogen peaks with the spectrometer. In future experiments, the CO_2 can be doped with a small portion of nitrogen, and these peaks can possibly be studied to determine the electron temperatures [25,26].

4.3 CHARACTERIZATION OF PLASMA IN CARBON DIOXIDE

Optical emission spectroscopy was performed on gaseous CO_2. The spectral data was taken at 4.4 atm with a 1 mm gap and 15 mA in the test cell from ranges of 290-326 nm and 360-430 nm. The peaks were not clearly defined. Next, CO_2 pumped into a separate test cell and the pressure was lowered to 4 torr. The gap was 20 cm and the current was 15 mA. The spectral data was taken with the Ocean Optics HR4000 Spectrometer. The plasma was very stable, and the peaks were well defined.

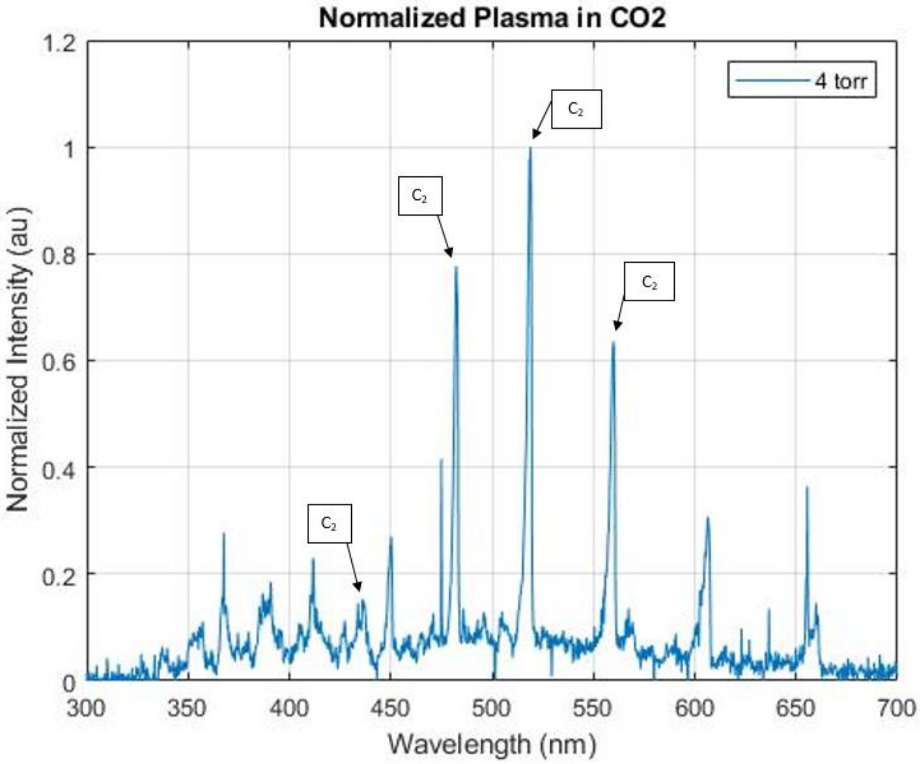

Figure 4.6 CO_2 optical emission spectroscopy 300 – 700 nm

Portions of the spectra were viewed with the IsoPLANE SCT 320 in 4.4 atm at 15 mA to compare with the with the data from Figure 4.6. This data is shown in Figure 4.7. The high-pressure plasma shows a flatter spectrum than the low-pressure CO_2 plasma.

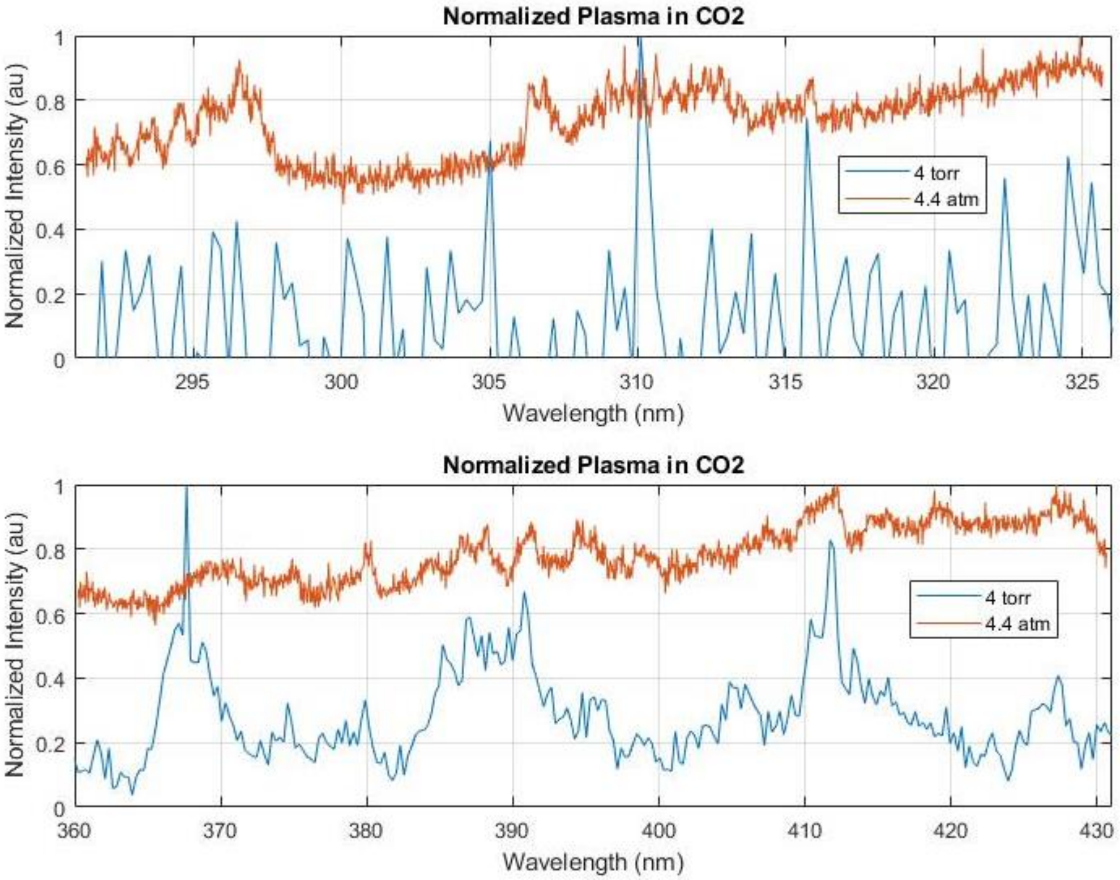

Figure 4.7 CO_2 pressure broadening, 290 – 327 nm (top), 360 – 431 nm (bottom)

Similar to the air at high pressure, the carbon dioxide plasma appeared to turn white. Since the peaks became flatter and the color of the plasma became whiter, we know spectral line broadening has occurred [27]. There are three main causes for spectral line broadening are natural or intrinsic broadening, doppler broadening, and collisional broadening. Collisional broadening, also commonly known as pressure broadening, seems to be the main player in the broadening of the spectrum in the case of Figure 4.7. Pressure broadening effects were also observed in supercritical CO_2 optical emission spectroscopy carried out by Suga [28].

Perturbation by colliding atoms in a high-pressure gas results in the broadening of emission lines as well as absorption lines. According to Heisenberg's uncertainty principle, the finite duration of the radiation process of an electron transition will give a spectral line with a finite width. For high pressure gases, especially gases with largely atomic nuclei, collisions will occur frequently. If a collision occurs before the radiation process of the electron transition is complete, then a premature transition and emission of a photon will occur. The decreased lifetime of the state will result in broadening the emission line [29].

Discharge current measurements in supercritical carbon dioxide were conducted using a Pearson current monitor with a 20:1 attenuator. When striking plasmas in high pressures, the electrodes began to act as capacitors. The electrodes would gather a charge and discharge rapidly with a high current. The rate at which a discharge would happen depended on the breakdown voltage and the charging rate that is governed by the power supply current output. A discharge rate at over 10 pulses per second can become very violent. Figure 4.8 shows the discharge current of a single pulse in supercritical carbon dioxide at a pressure of 80.7 atm and a temperature of approximately 327 K. The RMS current is a function of pulse frequency. A plasma was pulsed at approximately 2.22 pulses per second and had an RMS current of 145.9 mA. The electrode spacing was approximated using ImageJ software. A shadowgraph image of the electrode spacing is shown in Figure 4.9. The gap was 120+ microns.

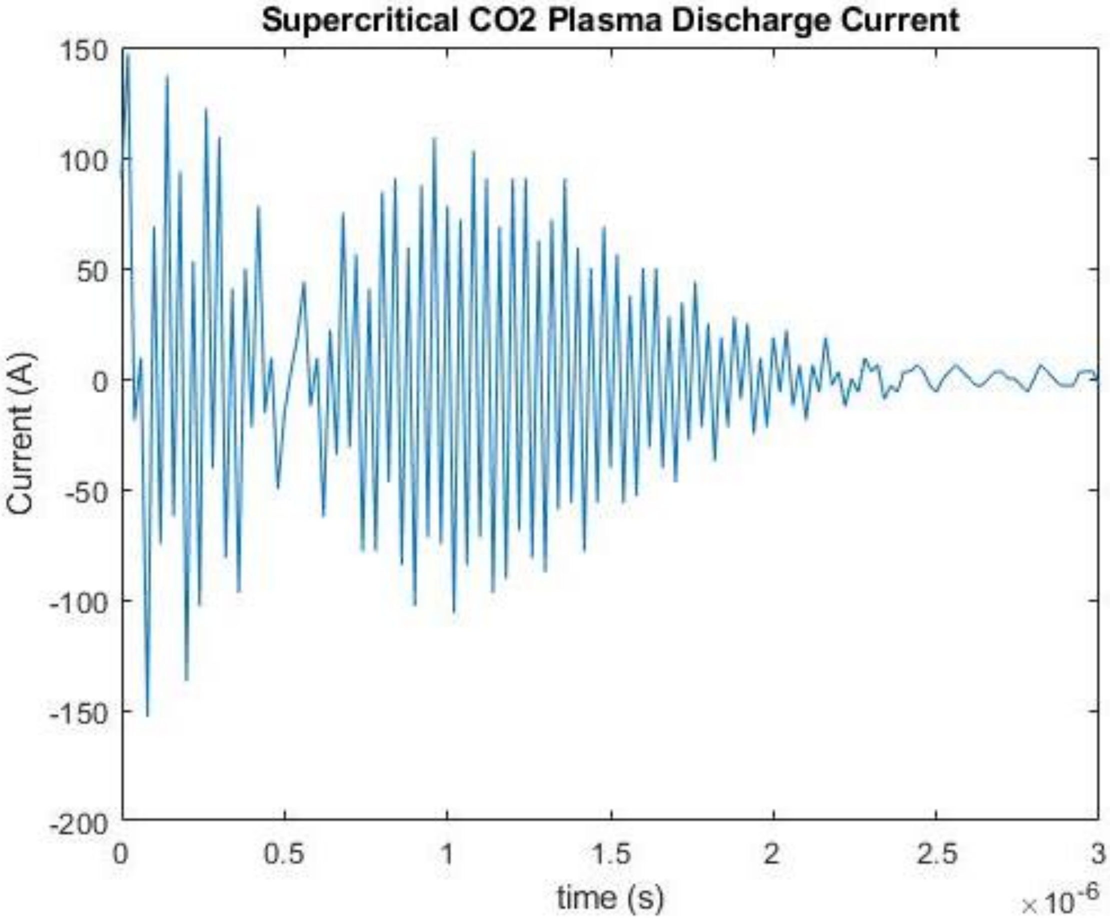

Figure 4.8 Discharge current in sCO2

The discharge current is almost typical of an underdamped RLC circuit. However, there is one large positive current spike followed by an oscillating phase that increases and then decreases in amplitude. This singular pulse of plasma consists of many oscillating pulses at approximately 25 MHz. It is very likely that these oscillations are were the cause of such violent EMPs. This waveform shows that there is a positive pulsed discharge that is approximately 40 ns in duration. This initial positive pulse reaches an amplitude and has a similar duration to the discharge current reading by Zhang [8]. However, our circuit contains shielded cable with an estimated capacitance of 18 pF/ft and inductance of 131.6 nH/ft. This cable would have a resonant frequency of 25.85 MHz if it were 4 feet long, and the amount of shielded cable downstream of the cathode is approximately 4 feet in length. This leads us to believe that the oscillations are caused by internal resonance between the conducting core of the cable and the braided shield of the cable. Therefore, the oscillating behavior of the current is relative to the behavior of an RLC circuit [30].

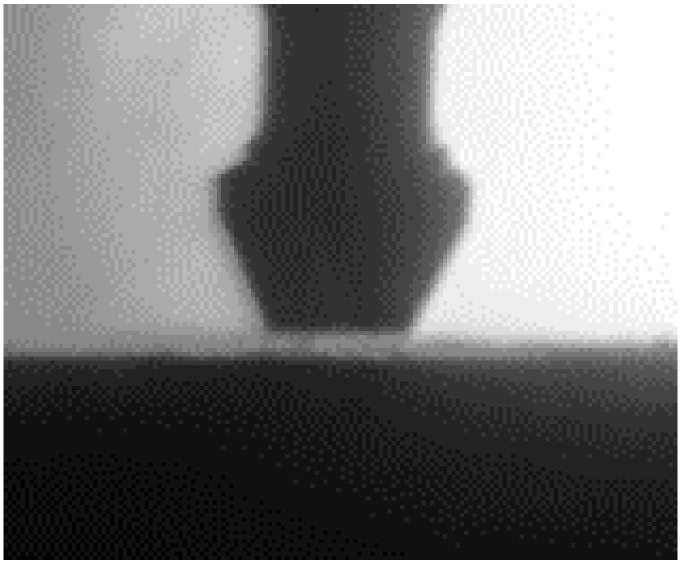

Figure 4.9 Shadowgraph image of electrode gap

The voltage output and current output from the power supply are shown in Figure 4.10. This output is achieved by having the power supply current on its lowest setting (0.1 mA). A low power supply output current causes slow discharge frequency. A high discharge frequency will create strong electromagnetic interference and affect the camera and electrical components. The plasma is in the arc regime also, so low frequency pulses will help preserve the life of the electrodes.

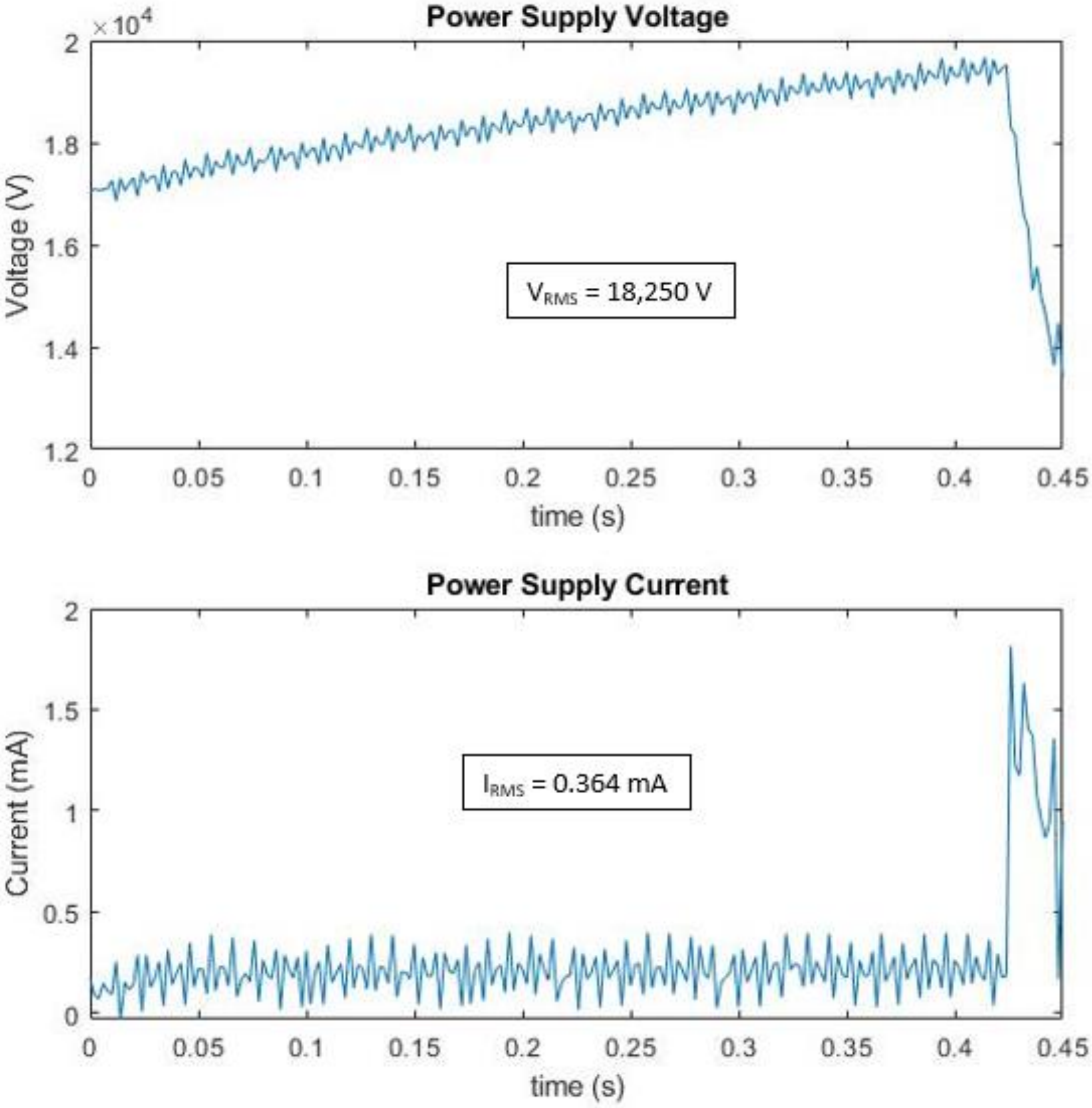

Figure 4.10 Power supply output

A zoomed look at a current discharge is shown in Figure 4.11. This current discharge was created at 79 atm and a temperature of approximately 327 K with an electrode spacing of approximately 50 µm. This test was performed after the discovery of the 25 MHz oscillations. Figure 4.11 shows that the 25 MHz oscillations affect the entire waveform. Figure 4.11 seems to show that the plasma discharge lasts approximately 52 ns, and what proceeds 52 ns is solely internal resonance caused by the extra capacitance and inductance from shielded cables.

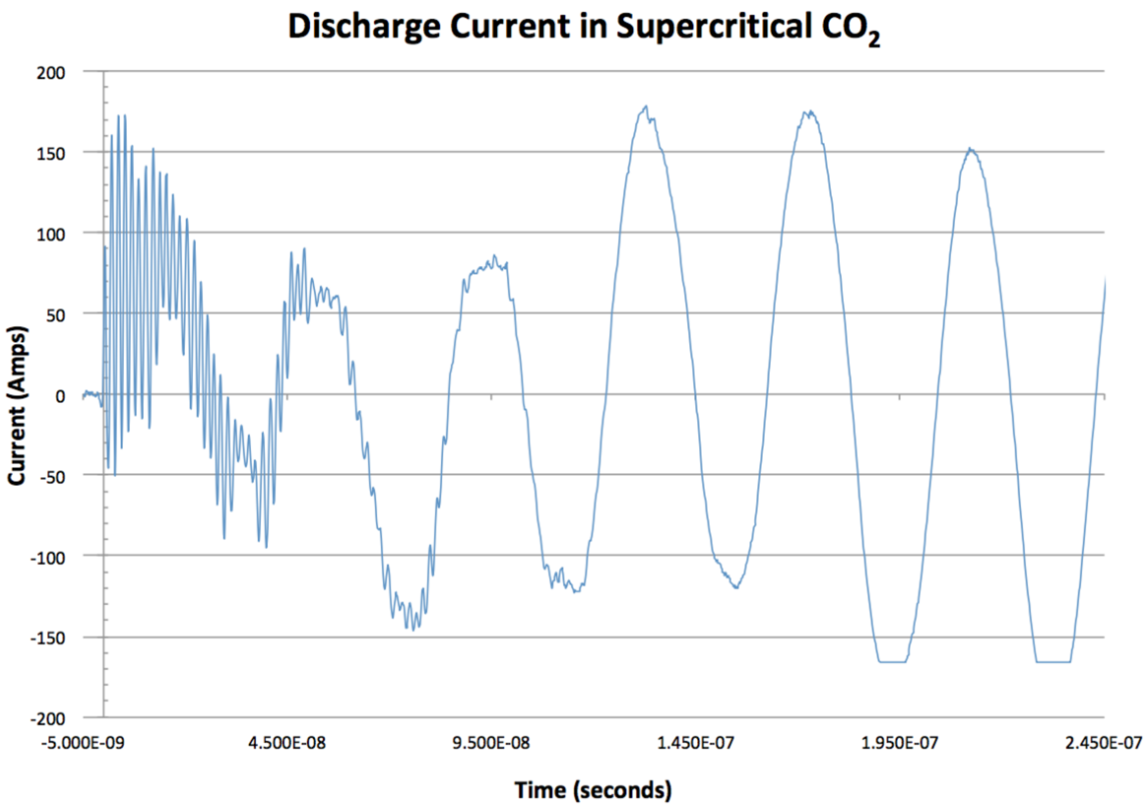

Figure 4.11 Detailed trace of discharge current

4.4 SCHLIEREN AND SHADOWGRAPH IMAGING

Schlieren high speed imaging was used to view the density gradients, convection currents, and the effect of pulsed plasmas in liquid, gaseous, and supercritical carbon dioxide. It is most efficient to test liquid, supercritical, then gaseous carbon dioxide. Liquid carbon dioxide was tested first at 76 atm and approximately 298 K with an electrode spacing of 150 µm.

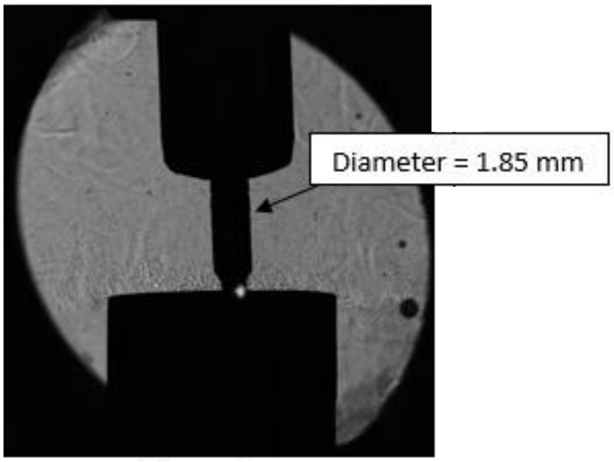

Time = 0 ms

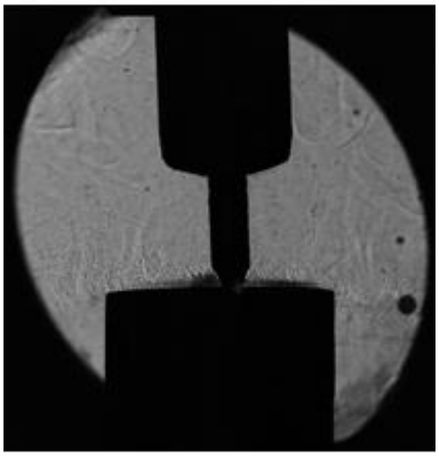

Time = 1 ms

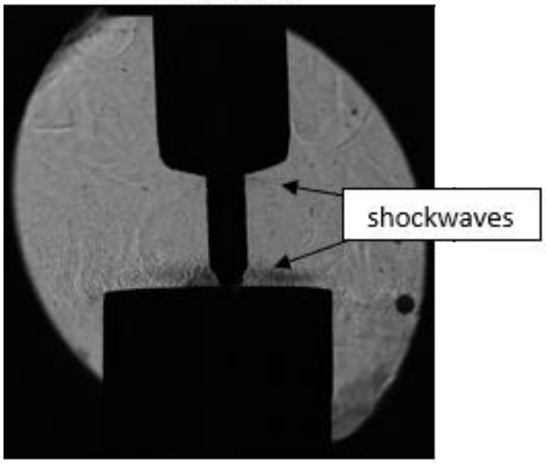

Time = 2 ms

Figure 4.12 Liquid CO_2 plasma at 76 atm, 298K with electrode spacing of 150 μm

When a plasma is struck in a dense medium, such as liquid CO_2, it will create a shockwave. Figure 4.12 shows two shockwaves. One large shockwave comes off the face of the cathode, and a small shockwave comes from a sharp corner on the anode. The large shockwave traveled upwards at approximately 0.8 m/s.

High pressure liquid carbon dioxide is heated using the cartridge heaters to reach supercritical pressures. The test cell takes over 30 minutes to become relatively evenly heated. Schlieren imaging enabled us to see how small temperature gradients can cause density fluctuations and convection currents. After 5 minutes of heating to 327 K, there is still a clear boundary layer between the liquid and supercritical fluid.

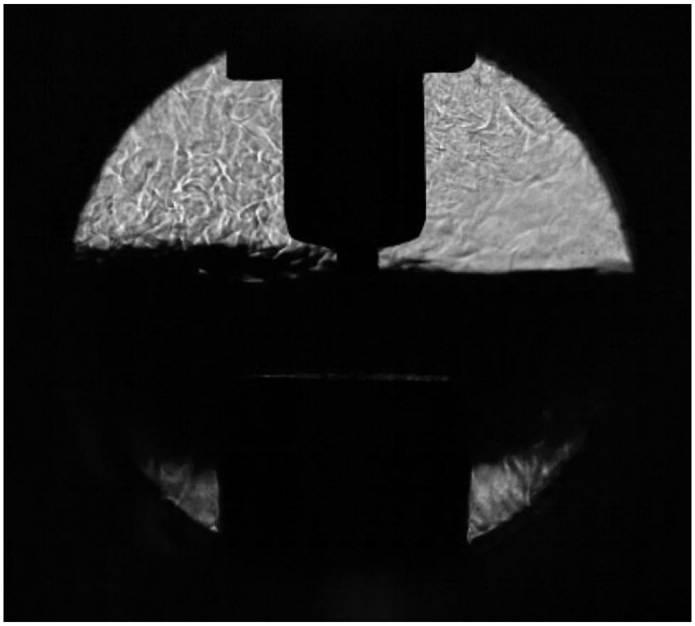

Figure 4.13 Early heating process of supercritical carbon dioxide

The liquid layer at the bottom of the test cell remained there for approximately 25 minutes. This is comparable to Case 1 in the Thermal Analysis section. Convection currents were observed after allowing the test cell the heat up even longer. The colder, denser carbon dioxide would stay at the bottom of the test cell, and the hotter, less dense carbon dioxide would flow up into the bellow. The supercritical carbon dioxide would cool down near the top of the bellow, and it would fall back down to the bottom of the test cell.

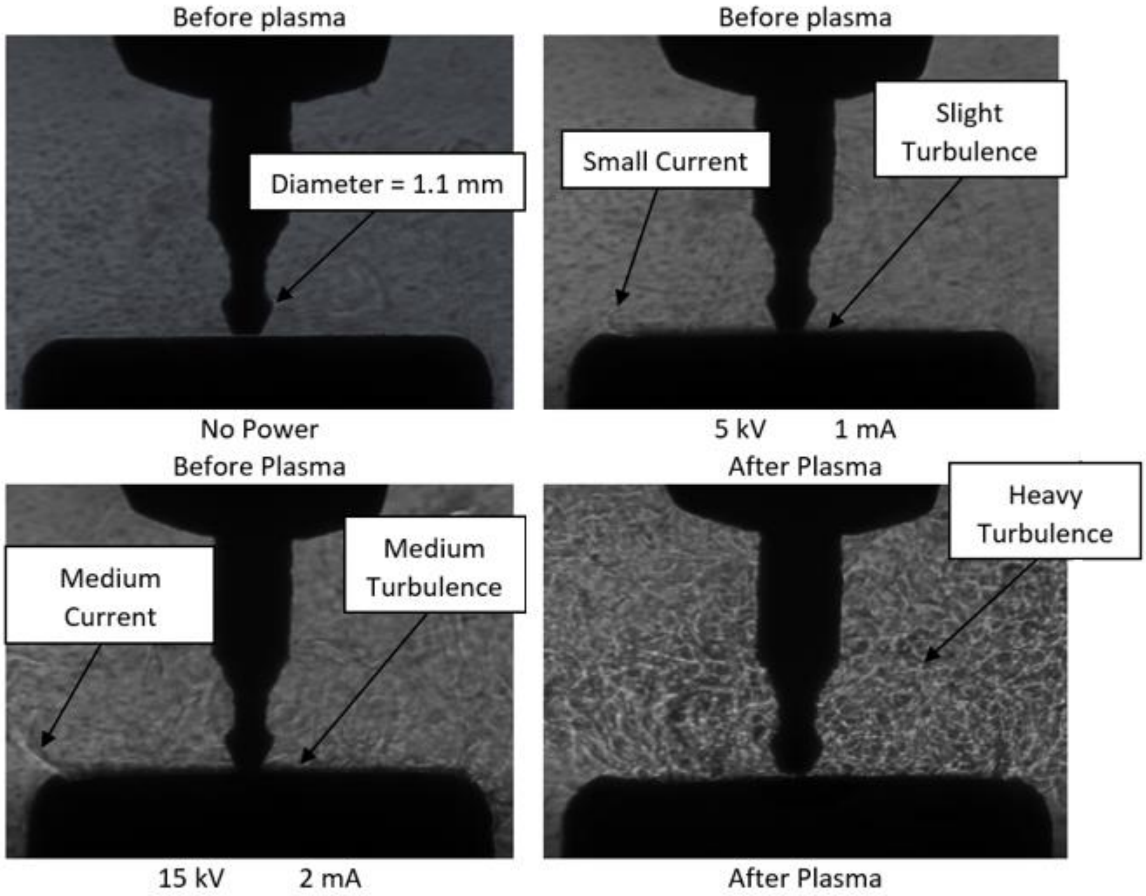

Figure 4.14 Effects of plasma and charge in supercritical CO_2

An interesting phenomenon is observed in supercritical carbon dioxide. As the electrodes become charged, positively charged ions are forced away from the anode tip. Positive ions also collide with neutral molecules as they’re forced away from the anode. These large positive ions and neutral molecules leave a wake behind. This phenomenon is known as ionic wind. The ionic wind effect is also seen in liquid carbon dioxide. The large density gradient in supercritical carbon dioxide makes the ionic wind much easier to see.

Ionic wind is not a phenomenon discussed by Ihara in his research with positively pulsed streamers in sCO_2 [17]. Ihara tested a needle to plane electrode arrangement, and estimated that the electric field strength at the tip of the needle was approximately 9 MV/cm. This approximation was made using the equation for a conducting hyperboloid [31].

V = Voltage, d = electrode gap, r = radius of curvature, $$E_{max} = \frac{2V}{r\,ln[1 + {}^{4d}/_{r}]} \qquad (7)$$

The radius of curvature is approximately 400 μm and the electrode gap is approximately 50 μm in Figure 4.14. At 5 kV the electric field is approximated to be 1.1 MV/cm, and at 15 kV it is approximately 3.4 MV/cm. Figure 4.10 shows that electrical breakdown occurs around 19.5 kV which means the electric field is approximately 4.4 MV/cm. The electric field required from breakdown is much lower than what Ihara calculated at 9 MV/cm. A lower breakdown may have occurred because the supercritical CO_2 has a clustering effect, and our electrode gap was much smaller than Ihara's. Or there may be some error in electric field calculations since the anode tip is not round and polished. Future tests should use a more rounded anode tip. It is also possible that breakdown can occur more easily in higher temperature supercritical CO_2.

During these tests, the effects of supercritical carbon dioxide as a solvent were also witnessed. The adhesive from the tape was dissolved and spread throughout the entire test cell. This made the windows unclear. But this was only noticed once supercritical conditions were met. Figure 4.15 shows the clear windows in liquid CO_2, and the dirty windows in supercritical CO_2.

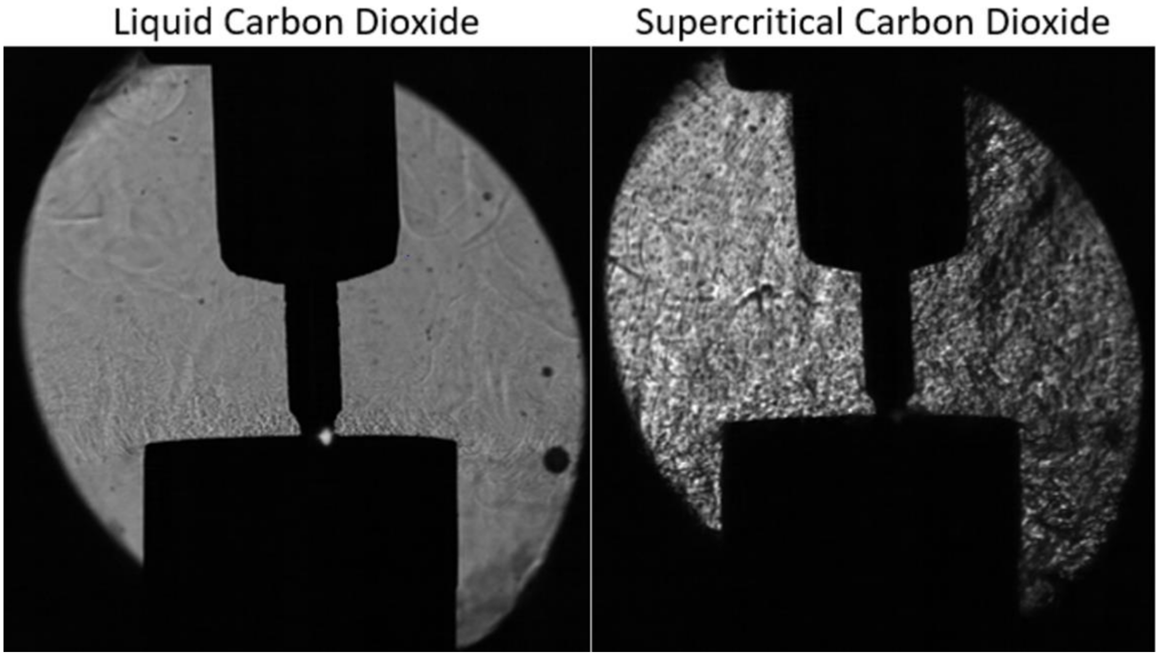
Liquid Carbon Dioxide

Supercritical Carbon Dioxide

Figure 4.15 Supercritical carbon dioxide solvent effects

Schlieren imaging was performed on a pulsed plasma in gaseous carbon dioxide at 55 atm and 327 K with an electrode spacing of 75 µm. Some particles were seen coming off the surface of the cathode after the plasma pulsed. This could potentially be electrode degradation.

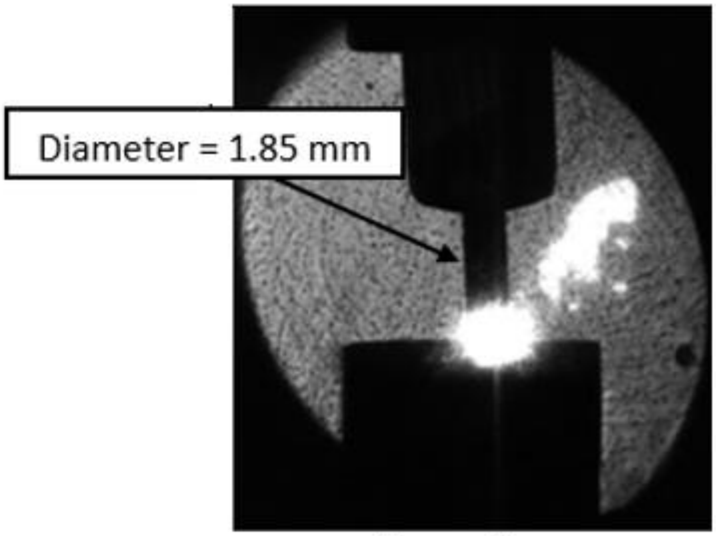

Time = 0 ms

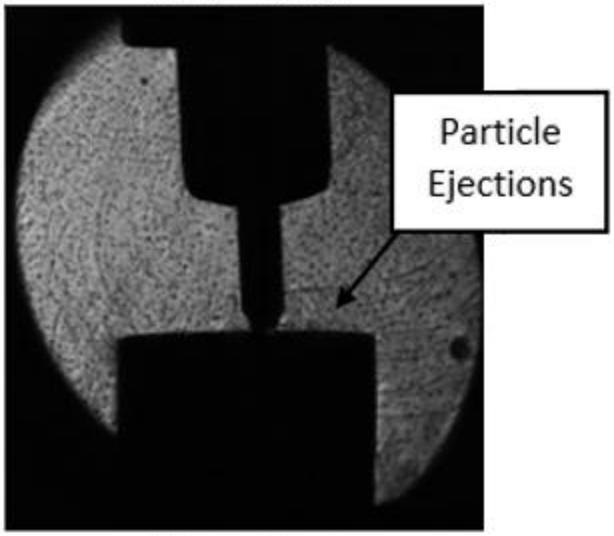

Time = 1 ms

Figure 4.16 Gaseous CO_2 plasma at 55 atm, 327 K with electrode spacing of 75 µm

4.5 ELECTRODE DEGRADATION

After striking plasmas in gaseous, liquid, and supercritical carbon dioxide, the test cell was disassembled, and the cathode was examined under a Keyence microscope. There were multiple spots on the face on the cathode that have experienced thermal erosion or shockwave damage. Figure 4.17 shows a colored image of the top face of the cathode. This image shows in great detail where and to what extent oxidation and thermal erosion have occurred. Figure 4.18 shows a topographic map of the cathode to show how deep the cathode spot goes.

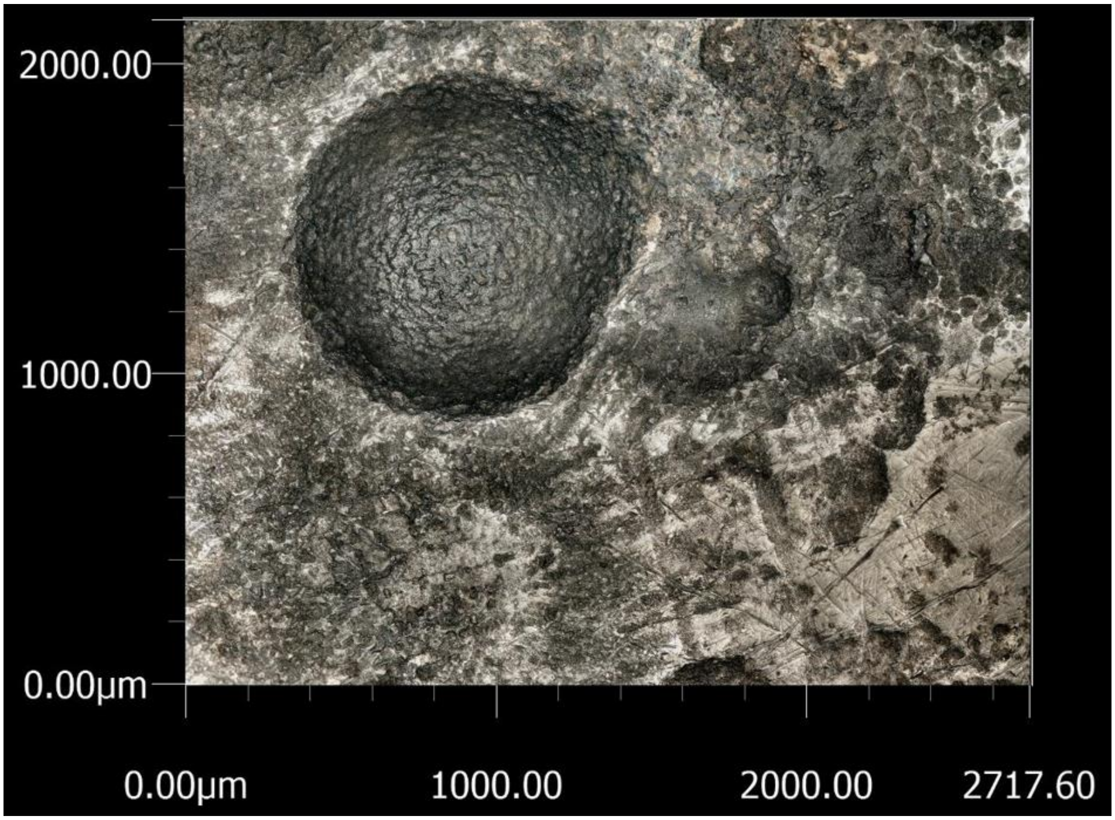

Figure 4.17 Cathode degradation

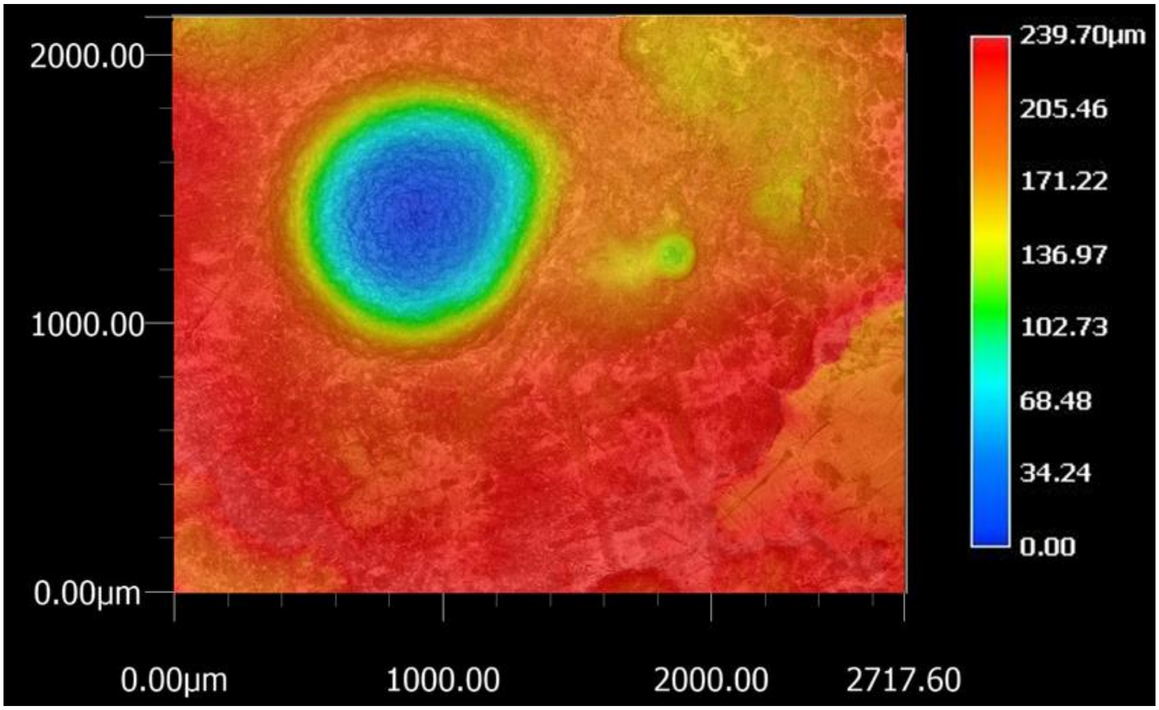

Figure 4.18 Topographic map of cathode

A low pulse frequency will limit the amount of time a thermal arc connects to the cathode. The cathode will experience less thermal erosion if the hot thermal arcs are pulsed at the lowest frequency possible. Future work should also include considering different coatings for the cathode. There are multiple reasons for this. Most importantly, the stainless-steel electrode tip has carbon in it. So, if there are carbon deposits in the test cell, it could possibly have come from the cathode rather than through electrochemical reduction. Strong materials that are more resistant to thermal erosion can be used to coat the cathode tip [32]. Cathode erosion makes it impossible to know the precise distance of the electrode gap.

The cathode tip is not the only part of the electrode that wears down over time. The Conax fittings come with Viton rubber seals and PEEK insulators. Over time, supercritical CO_2 will work its way into the porous plastic and make it expand slightly and become brittle. This is not a serious problem unless the PEEK insulator needs to be removed. The only way to get a saturated PEEK insulator off a metal rod is by breaking the PEEK. The Viton rubber experiences degradation over time. Over-compressing the rubber seal will deform it and increase the chance for an electrical arc through the Viton to the Conax housing.

4.6 ELECTRODE DISPLACEMENT

During testing, it was observed that the electrode gap would increase as the pressure in the test cell increased. Figure 2.2 and Figure 2.3 show the original and modified electrode designs with the Conax housing. The design in Figure 2.2 showed much more displacement than the modified Conax housing. The displacement was mitigated by adding a hex nut to the electrode, and an o-ring was placed between it and the plastic tube on the anode. The cathode has a similar design, but since it is not designed for high-voltage, it uses a ¼" electrode.

Data regarding electrode displacement was created using pressurized air. These tests were done by lowering the pressure to atmospheric pressure and moving the electrodes to a touching position. The pressure was then increased incrementally, and the gap between the electrodes was measured at each increment. The first test was done using the electrode design from Figure 2.3. However, the plastic tube was badly compressed from the Viton rubber. For the second test, extra kapton tape was added around the compressed area of the plastic to serve as a filler.

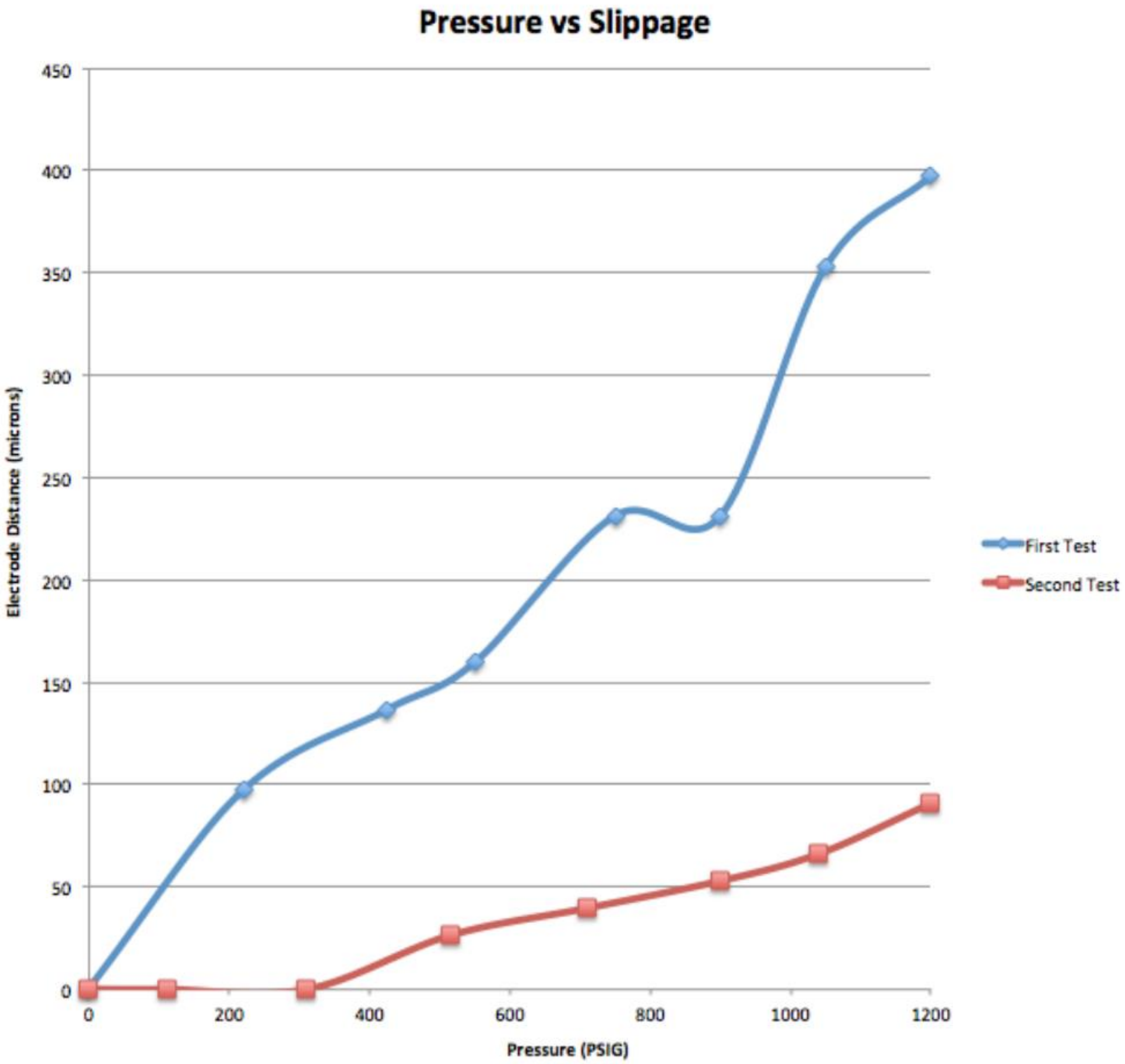

Figure 4.19 Electrode displacement plot

The slippage was greatly mitigated for the second test. When depressurizing, it was observed that the electrodes went back to their original positions. This observation shows that the main reason for electrode displacement was the flexion of the Viton rubbers and compression of the rubber o-rings.

CHAPTER 5

CONCLUSION

5.1 MAJOR FINDINGS

This test cell is a good prototype for a supercritical reactor. The system has been tested up to 135 atm, and it has proven to be safe and reliable. Experiments can be conducted remotely with LabVIEW and the USB connected DSLR camera.

A heat wrap that is wrapped around the bottom flange and the high-pressure bellow will significantly increase the heating speed of the CO_2, and it will cause the CO_2 to be more evenly heated than if only the cartridge heaters were used. If the cartridge heaters are the only source of heat, then the test cell will be unevenly heated. Internal convection currents will take place. Cold CO_2 will collect in the bottom of the test cell and slowly heat up. Hot CO_2 will rise into the bellow where it will cool and then fall back into the bottom of the test cell. It is currently unknown to what effect uneven heating has on supercritical clustering. It is possible that if uneven heating effects the way clusters behave, then it may be possible to achieve lower breakdown voltages with a test cell that is heated unevenly than if it were heated evenly.

Optical emission spectroscopy showed that high-pressure CO_2 discharges are more susceptible to pressure broadening effects than high-pressure N_2 discharges. As pressure increased, the peaks became much flatter in CO_2. Figure 4.6 shows clearly defined spectral peaks in a CO_2 plasma at 4 torr. However, there were no clearly defined spectral peaks when the pressure was increased to 4 atm.

The stainless-steel electrode tips will degrade and become oxidized after experiencing arc discharges. The electrodes will also become damaged if they touch one another. Tungsten electrode tips will serve as a better option in future experiments.

No corona discharges or streamers were seen in these tests. This is likely because the electrode spacing was too small to see any of these phenomena. It was seen that electrical breakdown occurred with an electric field strength of approximately 4.4 MV/cm rather than 9 MV/cm, as shown in Ihara's research [17]. The reason for breakdown in a lower electric field is not completely understood at this time. However, it may be due to higher temperature supercritical CO_2, effects of supercritical clustering, or inaccurate estimates on the electrode's radius of curvature.

It was seen that discharges in liquid CO_2 caused large shock waves, and discharges in supercritical CO_2 cause weaker shock waves. An example of the shock waves occurring in liquid can be seen in Figure 4.12, and the shock waves in supercritical CO_2 can be seen in Figure 4.14. The turbulence seen in Figure 4.14 is a result of rapidly repeated discharges that created multiple small shock waves, whereas Figure 4.12 shows one prominent shockwave in liquid CO_2 created by a single discharge.

Figure 4.14 also shows a phenomenon known as ionic wind. This is caused by the high electric field strength at the tip of the anode. The electric field strips electrons from neutral carbon dioxide molecules, and it sends the cations towards the cathode. A flowing effect can be seen as the cations collide with the neutral molecules on their way towards the cathode. The amount of current and energy being consumed is very low when ionic wind is created. Therefore, the amount of thrust generated from ionic wind in supercritical CO2 should be studied further, as there could be potential applications elsewhere.

The major oscillating frequency acting on the discharge current was 25 MHz for supercritical plasmas at multiple different temperatures and pressures. This leads us the conclude that the oscillations are due to a factor outside of the test cell. The oscillations are most likely caused by the capacitance and inductance of the shielded cables and Conax fittings. The current discharge oscillates and resembles and RLC circuit. However, the shielded cables keep the electronics safe when the plasma is discharged at a slow rate. Shorter cables will lessen the oscillation frequency.

Schlieren of shadowgraph techniques are necessary to view the electrode gap due to the intense diffraction caused by the supercritical fluid. A clear, magnified Schlieren or shadowgraph image is difficult to obtain with a large working distance. A redesign of the test cell is necessary to achieve more detailed images.

5.2 FUTURE WORK

Much knowledge was gained from experimentation with the SCR. This prototype enabled us to witness some of the shortcomings that can be improved for future designs. The main issues encountered in this project were poor image quality of the electrode gap, test cell cleanliness, electrode degradation, uneven heating, unwanted electrode displacement, and a poor ground connection.

Poor image quality is largely due to the size of the test cell. The electrode gap can barely be seen at 100 microns, and that measurement is uncertain. The distance from the center of the electrode gap to the outside of the window flange is 67 mm. Schlieren or shadowgraph imaging techniques have proven to be the best methods for measuring the electrode gap. However, the working distance is increased even further when a bi-convex or plano-convex lens is placed between window flange and the camera. In order to get a very high magnification, the working distance must be shortened. This means the sapphire windows should be thinner, and the test cell should be redesigned so the electrode gap is closer to the window. Figure 5.1 shows the thin lens equation and magnification equation. In order to get the best magnified image, the lens must be very close to the object, and the focal length of the lens must be short. Another positive benefit to decreasing the distance between the object and the window would be that there will be less fluid to distort the image. Shadowgraph and Schlieren imaging techniques do a great job of minimizing the fluid distortion effects. If there is a less thick layer of fluid to penetrate, the edge of the electrodes may appear sharper.

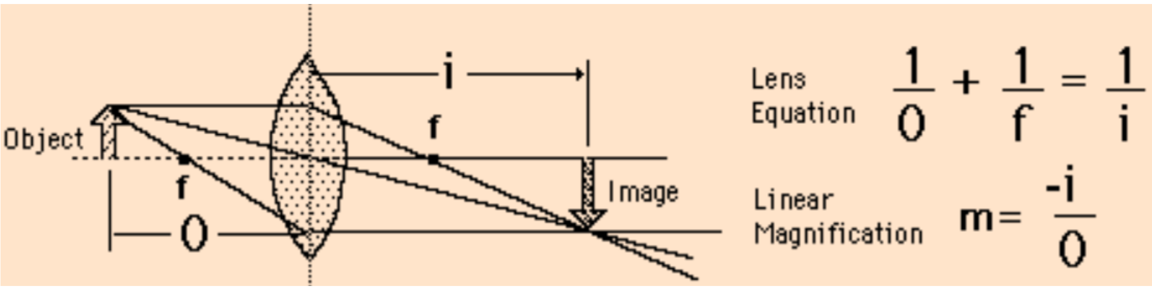

Figure 5.1 Thin lens and magnification equations

Figure 2.5 shows the current version of the anode tip being used. The reference measurement in this figure will be too far away from the electrode gap in a highly zoomed image. This means a new design for the anode tip is necessary. One idea would be to attach a tungsten needle with a known diameter to the anode. This diameter can be the reference measurement. A tungsten cathode tip can also be tested. However, this tip should not be pointed. The cathode tip needs to be plate-like so heat can dissipate well.

A needle will increase the strength of the magnetic field. With the needle-plate arrangement, streamers or corona discharges should be possible to observe. Testing a negative polarity power supply with the needle-plate arrangement should also be done. If a stable negative corona discharge can be produced, optical emission spectroscopy should be performed.

Test cell cleanliness is another issue that must be addressed. Contaminants inside the test cell can cause issues downstream with the back-pressure regulator as well as visibility issues with the test cell windows. The first precaution to keeping the test cell clean is to keep tapes and other materials outside of the test cell. For future work, small filters should be added to the system to maintain cleanliness. One filter should be placed upstream of the test cell to ensure no contaminants come from the pumps or the CO_2 tank. The other filter should be placed after the test cell. This filter is mainly to protect the back-pressure regulator. The back-pressure regulator will leak and be unable to form a proper seal if any contaminants get inside it.

Electrode degradation is an issue for multiple reasons that are discussed in Chapter 4.4. Experimentation with different electrode tip coatings should be tried. Some recommended coatings are platinum and tungsten. The cathode is bombarded with powerful shockwaves as well as high temperatures during testing, and the anode tip reaches high temperatures. Different coating materials and different coating thicknesses should be tested. After being tested they should be viewed under the Keyence microscope to check for damage.

Uneven heating is a problem that not only contributes to different density gradients, but to high-pressure convection currents. The test cell can be more evenly heated using heat wrap around the bellow and the rest of the test cell. A smaller test cell design would be easier and quicker to heat than the current test cell. Other groups have used a JASCO pump that circulates supercritical CO_2 through the system and runs it through a heater.

Another improvement that can be made on the setup deals with unwanted electrode displacement due to high pressures. As discussed in Chapter 4.6, improvements were made to address the electrode displacement problem. However, the problem was only mitigated and not completely solved. It is believed the Viton rubber is the cause of the displacement under high pressures. Designing an electrode housing without the Viton seal would be ideal in eliminating electrode displacement. This has been accomplished by Goto [20], and his supercritical CO_2 plasma reactor schematic is shown in Figure 5.2.

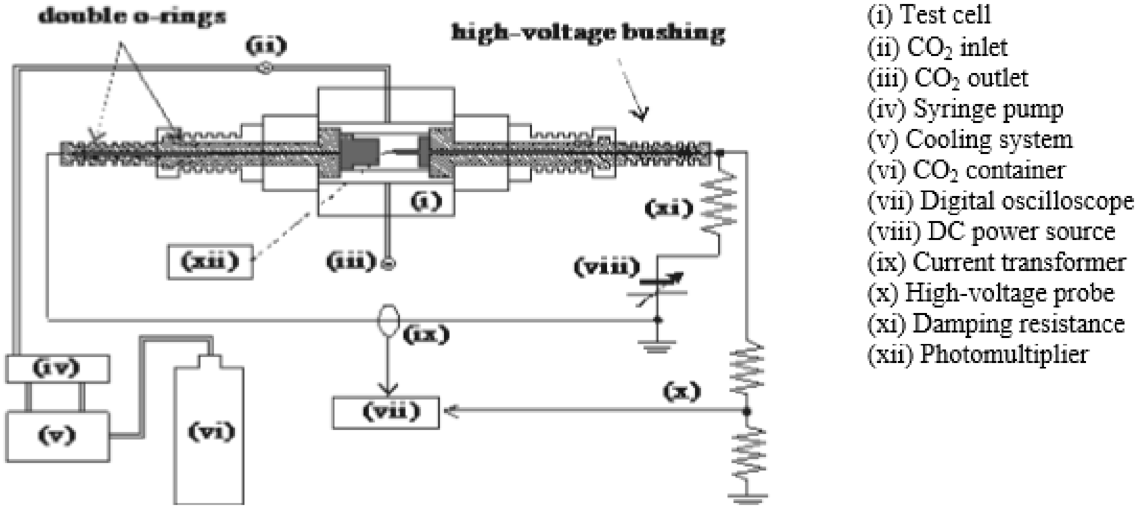

Figure 5.2 Plasma reactor schematic (non-slip electrodes) [20]

If the electrode displacement under high pressures issue is completely fixed, then a gear system could be added to the top flange of the bellow to control the electrode spacing. Currently, the electrode spacing is controlled by individually tightening each of the 4 bolts on the top flange. The four bolts on the top flange are ⅜” - 16. This means each full turn of the screw will lower the anode by 1/16”. Small spur gears can be attached to each of the bolts, and a larger inner gear can be used to turn each of the spur gears in unison.

Electromagnetic interference is an unwanted problem when working with high-voltage pulsing plasmas. A solid earth-ground connection can be very beneficial to mitigating EMIs and EMPs. The electrical shielding is currently connected to a water line that is far from the test cell. The water line connection was successful in mitigating EMIs and EMPs, and the camera and the LabView program does not shut down during tests. One or two solid grounding rods located underneath the test cell would be much more beneficial. One rod could be for the main electrical flow, and the other rod could be for the shielding. It would also be beneficial to test and confirm if the resonating discharge current is coming from the shielded cables in the circuit. This could be done by using unshielded cables and connecting to a strong earth ground. Shortening the length of cable used would also help. To be safe, the power supply current should be turned very low to prevent rapid discharges from creating EMPs that could damage the electronics.

A closer look should also be taken at the ionic wind produced in supercritical CO_2. Ionic wind can be used as a mechanism for propulsion in air. Unfortunately, the thrust created in air is very weak. However, it may be true that thrust created by ionic wind in supercritical CO_2 could be very strong. If the thrust is strong, there could be potential applications for drones on Venus in the distant future.

REFERENCES

[1] Kiyan, Tsuyoshi, et al. "Pulsed Discharge Plasmas in Supercritical Carbon Dioxide." *2005 IEEE Pulsed Power Conference*. IEEE, 2005.

[2] Spencer, Laura Frances. The Study of CO2 Conversion in a Microwave Plasma/Catalyst System. Diss. 2012.

[3] Friedrich, J. P., and E. H. Pryde. "Supercritical CO2 extraction of lipid-bearing materials and characterization of the products." *Journal of the American Oil Chemists' Society* 61.2 (1984): 223-228.

[4] Wakayama, Hiroaki, Tatsuya Hatanaka, and Yoshiaki Fukushima. "Synthesis of Pt–Ru Nanoporous Fibers by the Nanoscale Casting Process Using Supercritical CO2 for Electrocatalytic Applications." *Chemistry letters* 33.6 (2004): 658-659.

[5] Stauss, Sven, Hitoshi Muneoka, and Kazuo Terashima. "Review on plasmas in extraordinary media: plasmas in cryogenic conditions and plasmas in supercritical fluids." *Plasma Sources Science and Technology* 27.2 (2018): 023003.

[6] Urabe, Keiichiro, et al. "Dynamics of pulsed laser ablation in high-density carbon dioxide including supercritical fluid state." *Journal of Applied Physics* 114.14 (2013): 143303.

[7] Zasova, L. V., et al. "Structure of the Venus atmosphere." *Planetary and Space Science* 55.12 (2007): 1712-1728.

[8] Zhang, C. H., et al. "Generation of DC corona discharge in supercritical CO/sub 2/for environment protection purpose." *Fourtieth IAS Annual Meeting. Conference Record of the 2005 Industry Applications Conference, 2005.*. Vol. 3. IEEE, 2005.

[9] S. Hamaguchi, “Physics of discharges in supercritical fluids,” Osaka University, 2005 (in Japanese, unpublished).

[10] Kiyan, Tsuyoshi, et al. "Negative DC prebreakdown phenomena and breakdown-voltage characteristics of pressurized carbon dioxide up to supercritical conditions." *IEEE transactions on plasma science* 35.3 (2007): 656-662.

[11] Kiyan, Tsuyoshi, et al. "Polarity effect in DC breakdown voltage characteristics of pressurized carbon dioxide up to supercritical conditions." *IEEE transactions on plasma science* 36.3 (2008): 821-827.

[12] Furusato, Tomohiro, et al. "Fractal analysis of positive pulsed streamer patterns in supercritical carbon dioxide." *IEEE Transactions on Plasma Science* 40.10 (2012): 2425-2430.

[13] Furusato, T., et al. "Visualization of positive pulsed streamer in supercritical carbon dioxide by Schlieren method." *2011 IEEE Pulsed Power Conference.* IEEE, 2011.

[14] Giants, Thomas W. "Crystallinity and dielectric properties of PEEK, poly (ether ether ketone)." *IEEE Transactions on Dielectrics and Electrical Insulation* 1.6 (1994): 991-999.

[15] Furusato, Tomohiro, et al. "Initiation mechanism of a negative nanosecond pulsed discharge in supercritical carbon dioxide." *IEEE Transactions on Plasma Science* 40.11 (2012): 3105-3115.

[16] Ihara, T., et al. "Initiation mechanism of a positive streamer in pressurized carbon dioxide up to liquid and supercritical phases with nanosecond pulsed voltages." *Journal of Physics D: Applied Physics* 45.7 (2012): 075204.

[17] Ihara, Takeshi, et al. "Positive pulsed streamer in supercritical carbon dioxide." *IEEE Transactions on Plasma Science* 39.11 (2011): 2650-2651.

[18] Rasband, W.S., ImageJ, U. S. National Institutes of Health, Bethesda, Maryland, USA, https://imagej.nih.gov/ij/, 1997-2018.

[19] Bak, Moon Soo, Seong-Kyun Im, and Mark Cappelli. "Nanosecond-pulsed discharge plasma splitting of carbon dioxide." *IEEE Transactions on Plasma Science* 43.4 (2015): 1002-1007.

[20] Goto, M., et al. "Reaction in plasma generated in supercritical carbon dioxide." *Journal of Physics: Conference Series*. Vol. 121. No. 8. IOP Publishing, 2008.

[21] Joo, Jinsoo, and C. Y. Lee. "High frequency electromagnetic interference shielding response of mixtures and multilayer films based on conducting polymers." *Journal of Applied physics* 88.1 (2000): 513-518.

[22] Gentilman, Richard L., et al. "Large-area sapphire windows." *Window and Dome Technologies VIII*. Vol. 5078. International Society for Optics and Photonics, 2003.

[23] Autodesk® Autodesk Fusion 360, 2019, Autodesk, Inc.

[24] Ansys® Academic Research Mechanical, Release 18.1, ANSYS, Inc.

[25] Pai, David Z., Sven Stauss, and Kazuo Terashima. "Field-emitting Townsend regime of surface dielectric barrier discharges emerging at high pressure up to supercritical conditions." *Plasma Sources Science and Technology* 24.2 (2015): 025021.

[26] Tomai, Takaaki, Tsuyohito Ito, and Kazuo Terashima. "Generation of dielectric barrier discharge in high-pressure N2 and CO2 environments up to supercritical conditions." *Thin Solid Films* 506 (2006): 409-413.

[27] Goueguel, Christian L., Dustin L. McIntyre, and Jinesh C. Jain. "Influence of CO2 pressure on the emission spectra and plasma parameters in underwater laser-induced breakdown spectroscopy." *Optics letters* 41.23 (2016): 5458-5461.

[28] Suga, Yosuke, and Toshiyuki Watanabe. "Plasma optical emission spectroscopy in supercritical fluid for material synthesis process." *Transactions of the Materials Research Society of Japan* 35.1 (2010): 15-17

[29] E. F. Wyner, "D" Line Radiation in the Afterglow of High Pressure Sodium Arc Discharge, *GTE Sylvania Laboratory Report LR85*, March 1978

[30] Mak, Se-yuen. "The RLC circuit and the determination of inductance." *Physics Education 29.2* (1994): 94.

[31] Bamji, S. S., A. T. Bulinski, and K. M. Prasad. "Electric field calculations with the boundary element method." *IEEE Transactions on Electrical Insulation* 28.3 (1993): 420-424.

[32] Fridman, Alexander, and Lawrence A. Kennedy. *Plasma physics and engineering*. CRC press, 2004.

[33] Burm, K. T. A. L. "Continuum radiation in a high pressure argon–mercury lamp." *Plasma Sources Science and Technology* 13.3 (2004): 387.

[34] Chang, J-S., Phil A. Lawless, and Toshiaki Yamamoto. "Corona discharge processes." *IEEE Transactions on plasma science* 19.6 (1991): 1152-1166.

[35] Faircloth, D. C. "Technological aspects: High voltage." *arXiv preprint arXiv:1404.0952* (2014).

[36] Ito, Tsuyohito, and Kazuo Terashima. "Generation of micrometer-scale discharge in a supercritical fluid environment." *Applied physics letters* 80.16 (2002): 2854-2856.

[37] Jüttner, Burkhard. "Cathode spots of electric arcs." *Journal of Physics D: Applied Physics* 34.17 (2001): R103.

[38] Kawashima, Ayato, et al. "A supercritical carbon dioxide plasma process for preparing tungsten oxide nanowires." *Nanotechnology* 18.49 (2007): 495603.

[39] Khomich, Vladislav Yu, and Igor E. Rebrov. "In-atmosphere electrohydrodynamic propulsion aircraft with wireless supply onboard." *Journal of Electrostatics* 95 (2018): 1-12.

[40] Kiyan, Tsuyoshi, et al. "Weibull statistical analysis of pulsed breakdown voltages in high-pressure carbon dioxide including supercritical phase." *IEEE Transactions on Plasma Science* 39.8 (2011): 1729-1735.

[41] Kurniawan, H., T. Kobayashi, and K. Kagawa. "Effect of different atmospheres on the excitation process of TEA-CO2 laser-induced shock wave plasma." *Applied spectroscopy* 46.4 (1992): 581-586.

[42] Lawler, J. E. "Bremsstrahlung radiation from electron–atom collisions in high pressure mercury lamps." *Journal of Physics D: Applied Physics* 37.11 (2004): 1532.

[43] Liu, Chang-jun, Gen-hui Xu, and Timing Wang. "Non-thermal plasma approaches in CO2 utilization." *Fuel Processing Technology* 58.2-3 (1999): 119-134.

[44] Machmudah, S., et al. "Observation of Optical Emission Intensity of Plasma Induced by Nanosecond Laser Pulses in Supercritical CO2 Medium."

[45] Maehara, T., et al. "Spectroscopic measurements of high frequency plasma in supercritical carbon dioxide." Physics of Plasmas 16.3 (2009): 033503.

[46] Meek, J. M. "A theory of spark discharge." Physical review 57.8 (1940): 722.

[47] Saga, Koichiro, and Takeshi Hattori. "Wafer cleaning using supercritical CO2 in semiconductor and nanoelectronic device fabrication." Solid State Phenomena. Vol. 134. Trans Tech Publications Ltd, 2008.

[48] Staack, David, et al. "Characterization of a dc atmospheric pressure normal glow discharge." *Plasma Sources Science and Technology* 14.4 (2005): 700.

[49] Staack, David, et al. "DC normal glow discharges in atmospheric pressure atomic and molecular gases." *Plasma Sources Science and Technology* 17.2 (2008): 025013.

[50] Staack, David, et al. "Nanoscale corona discharge in liquids, enabling nanosecond optical emission spectroscopy." *Angewandte Chemie International Edition* 47.42 (2008): 8020-8024

[51] Vance, Edward F. "Shielding effectiveness of braided-wire shields." *IEEE Transactions on Electromagnetic Compatibility* 2 (1975): 71-77.

[52] Wang, Jin-Yun, et al. "CO2 decomposition using glow discharge plasmas." Journal of catalysis 185.1 (1999): 152-159.

[53] Chen, George, and A. E. Davies. "Electric stress computation-a needle-plane electrode system with space charge effects." *COMPEL-The international journal for computation and mathematics in electrical and electronic engineering* (1996).

APPENDIX A

JUNCTION BOX AND CONTROLS SYSTEM

This box contains very sensitive data acquisition cards along with a 24V power supply and a surge protector with 5 inlet plugs. The components in the junction box are used to control, monitor, and power many key elements in the system. An 8-slot chassis is used with 8 data acquisition (DAQ) cards to give readings on pressure, temperature and power supply output and input. The cards can also control the system by heating the test cell, moving the solenoid valves, and controlling the electronic pressure regulator (EPR3000). LabVIEW is used to monitor and control the system. The box is also equipped with an on/off switch to reset the components in case an EMP disrupts the readings.

The 24V power supply inside the junction box has a terminal block attached to it as well as a voltage divider. The power supply is connected to the terminal block so that there are two ground terminals, four 12V terminals, and two 24V terminals.

Some crucial components in the system are the cartridge heaters, thermocouples, pressure transducers, electronic pressure regulator, and back-pressure regulator. The cartridge heaters are used to boost the temperature of the test cell. The 4 cartridge heaters indirectly heat the CO_2 to put it beyond the critical temperature. The cartridge heaters have built in thermocouples. A relay switch is used to turn the cartridge heaters on or off based off a setpoint temperature given by the user in LabVIEW.

There are 3 thermocouple readings used in this experiment. One thermocouple reading is given at a point downstream of the test cell. This thermocouple is connected via a ¼” NPT pipe plug fitting. Another thermocouple is built into one of the cartridge heaters, and the final thermocouple is taped to the bottom of the test cell.

There is one pressure transducer downstream of the test cell that is connected via a ¼” NPT fitting, and there is a built-in pressure transducer in the electronic pressure regulator. The EPR3000 is a device that allows precise control of the back-pressure. This device can set a pilot pressure in the between 0-3000 psig for a back-pressure regulator. The back-pressure regulator and the EPR3000 are both products from Equilibar. These two devices limit the maximum pressure in the test cell. The schematic shown in Figure 2.6 shows that if the pressure in the test cell exceeds the pressure given by the EPR3000, then CO_2 will be vented out so that the pressure in the test cell can never exceed the back-pressure given by the EPR3000.

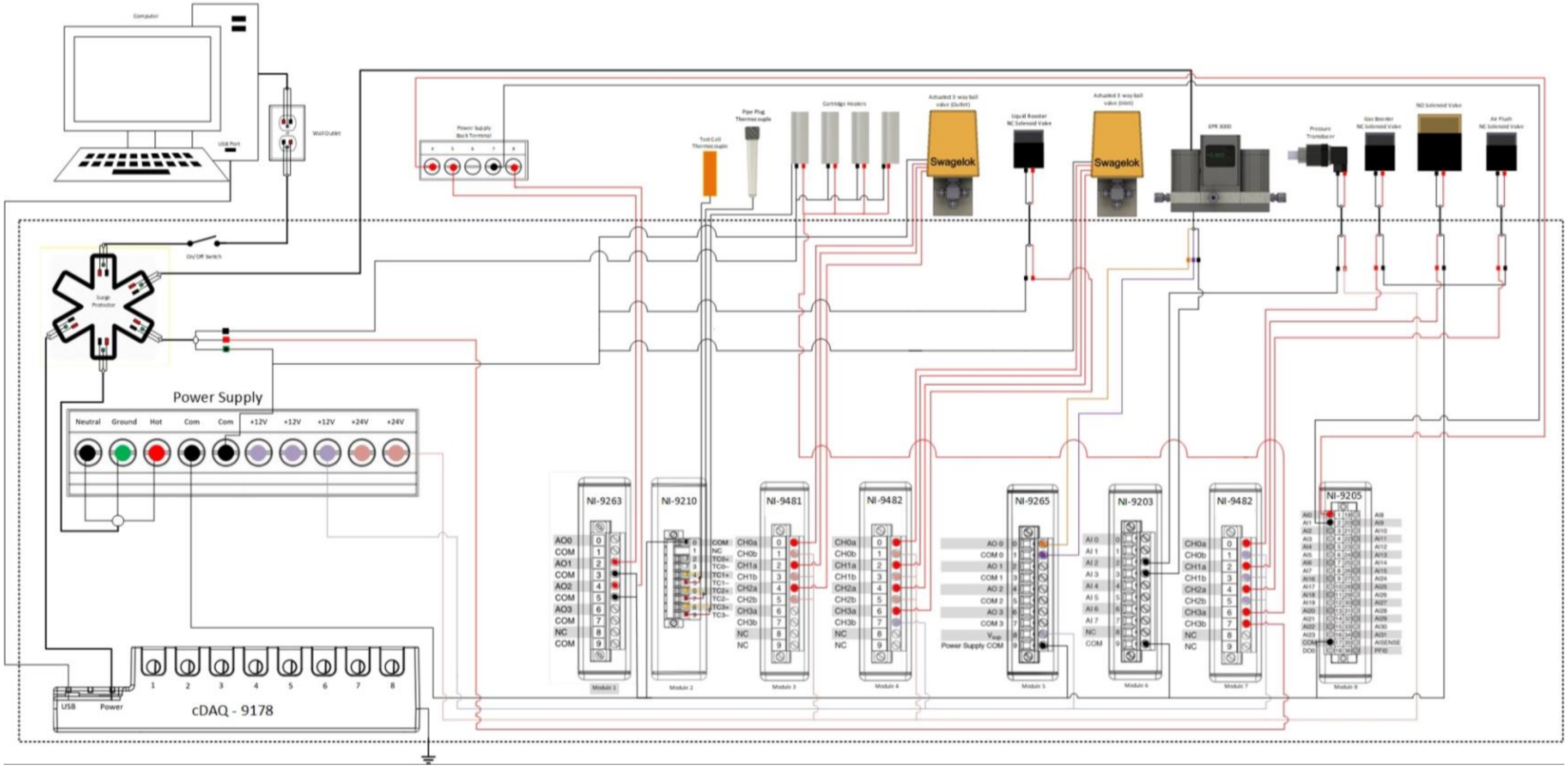

Figure A.1 Junction box and controls system schematic

APPENDIX B

LABVIEW BLOCK DIAGRAM

This LabVIEW program runs in a continuous while loop. The block diagram was designed to be easily understood. Each module is placed inside a box labeled with its module number.

The first module is the voltage output card. The voltage output card gives a voltage ranging from 0-10 VDC. This card allows the user to control the power supply's current and voltage outputs.

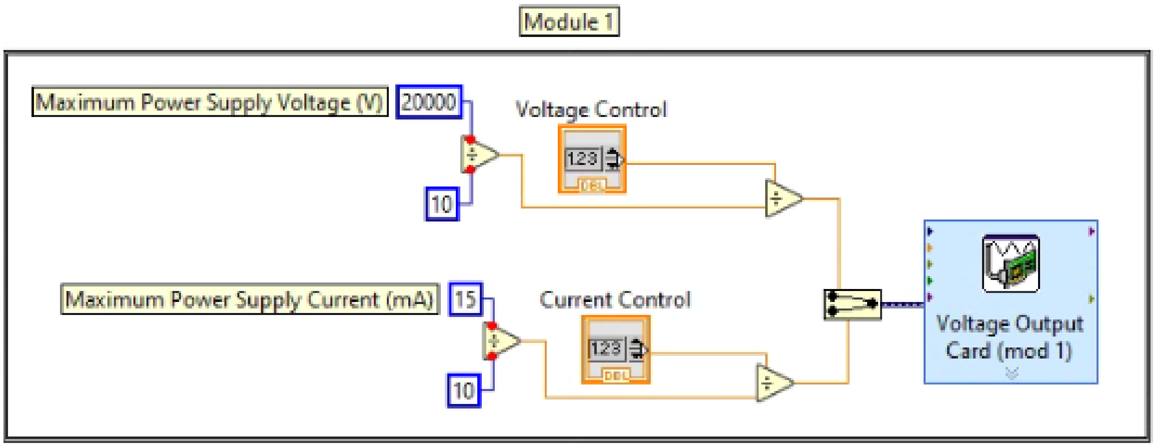

Figure B.1 Module 1

Module 2 is a thermocouple card. Module 2 gives the temperature readings of three separate thermocouples. One of those thermocouples in in a cartridge heater. The cartridge heaters and two solenoid valves are connected to Module 7, a mechanical relay card. Modules 2 and 7 communicate with each other to control when the cartridge heaters are powered on and off. A setpoint value is entered by the user. If the temperature reading on module 2 is below the setpoint, the mechanical relay card will complete the circuit to the cartridge heaters and power them on. Once the temperature exceeds the setpoint, the cartridge heaters will power off.

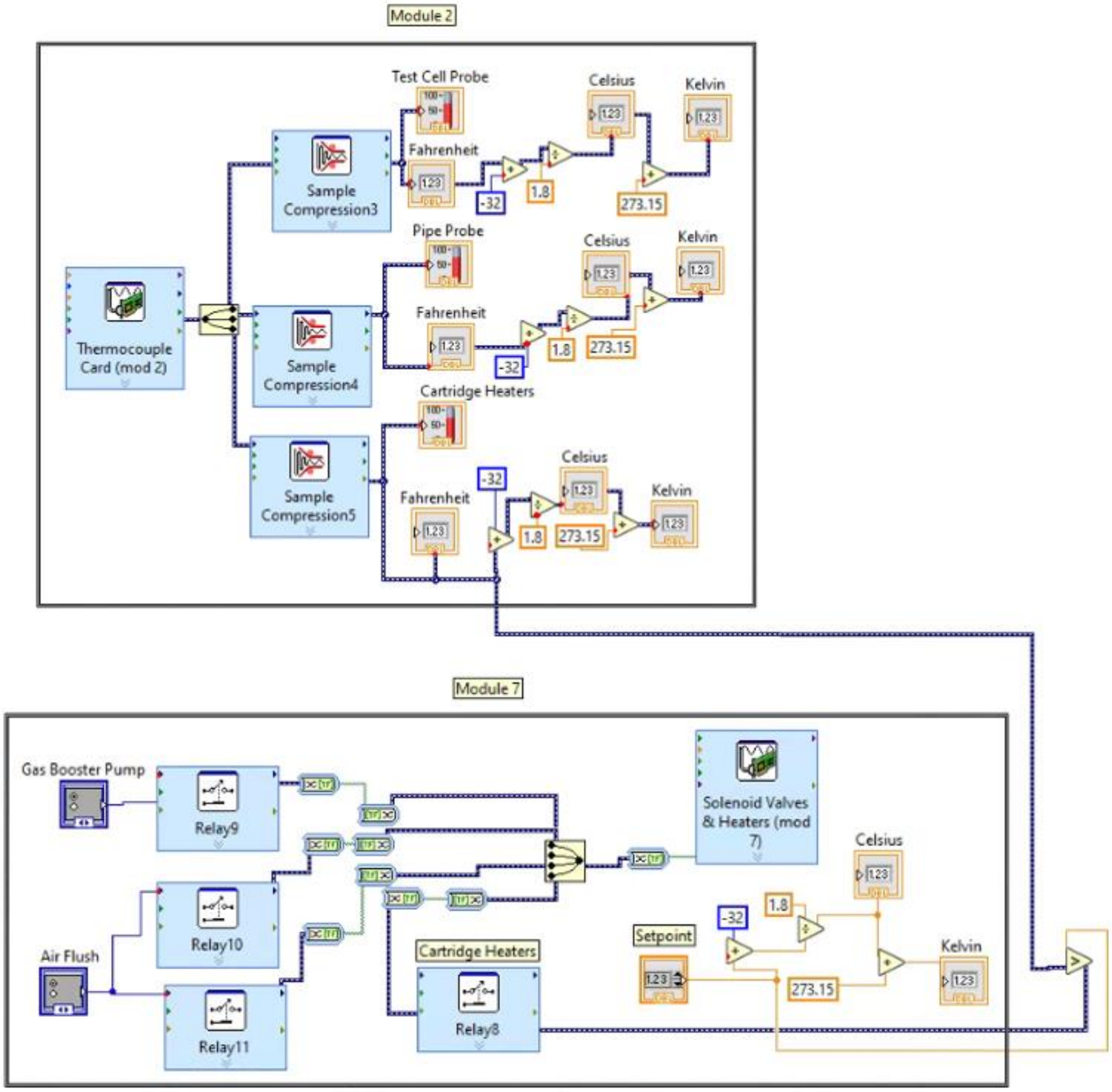

Figure B.2 Module 2 and module 7

Module 3 controls the Swagelok 3-way ball valve on the outlet side of the booster pumps. This module can set the ball valve to open, closed, or vent.

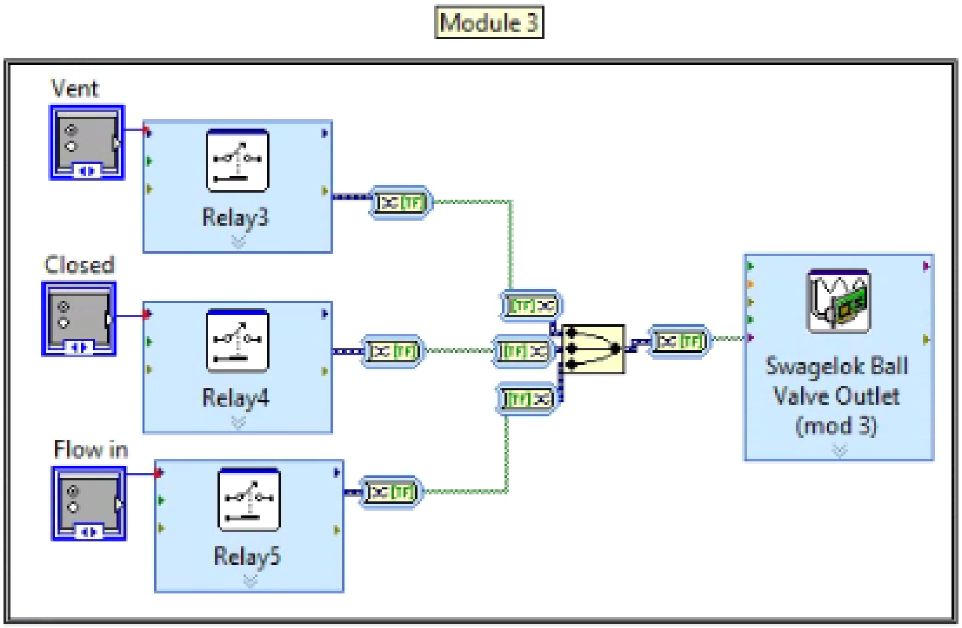

Figure B.3 Module 3

Module 4 is another mechanical relay card. This card controls the Swagelok 3-way ball valve on the inlet side of the gas booster pump. This card allows the user to position the ball valve so that either air or CO_2 can flow through the pump. Or the user can close the valve. This module also controls the liquid booster pump solenoid.

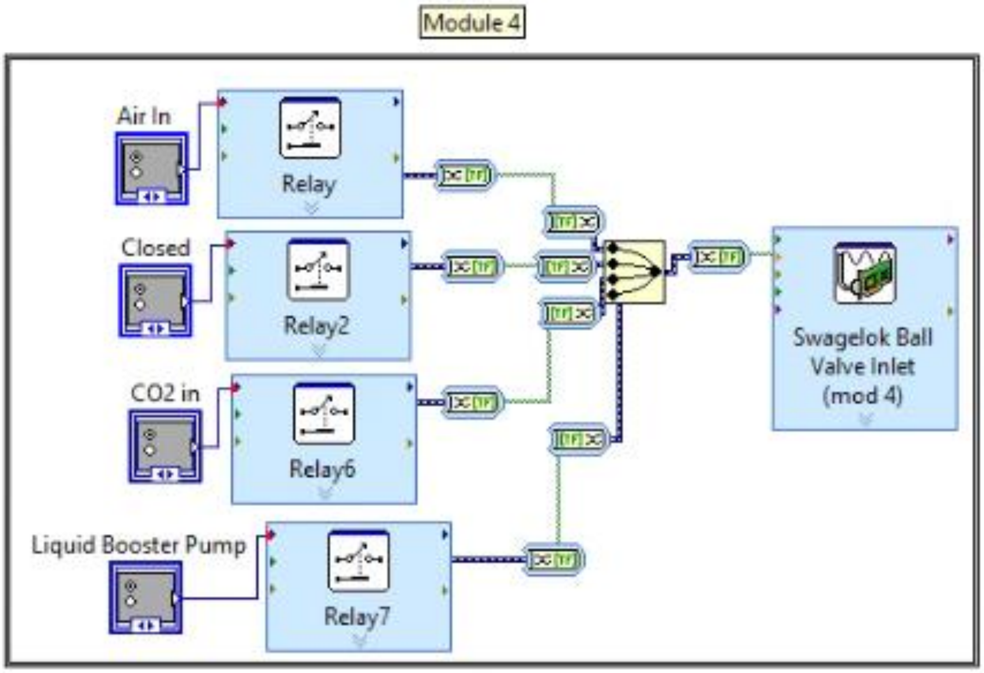

Figure B.4 Module 4

Module 5 controls the outlet pressure of the EPR3000. The EPR3000 is controlled with a 4-20 mA signal. This part of the code was designed so that the user could not input a back pressure higher than the Max Allowable Pressure (1500 psig). This is a safety feature that prevents the user from going to high and unwanted pressures. If higher back-pressure is desired, the user can change the Max Allowable Pressure value in the block diagram. The highest pressure that the EPR3000 can produce is 3000 psig. However, it is not recommended the user exceed 2500 psig, because the Swagelok ball valves are rated for only 2500 psig.

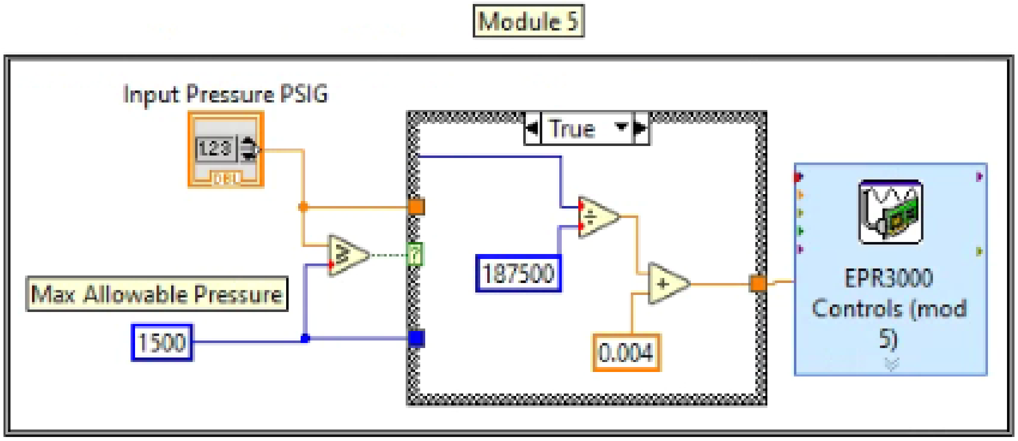

Figure B.5 Module 5

Module 6 is a current input card. This card receives signals ranging from 4-20 mA. Module 6 shows the back-pressure created by the EPR3000 and the test cell pressure.

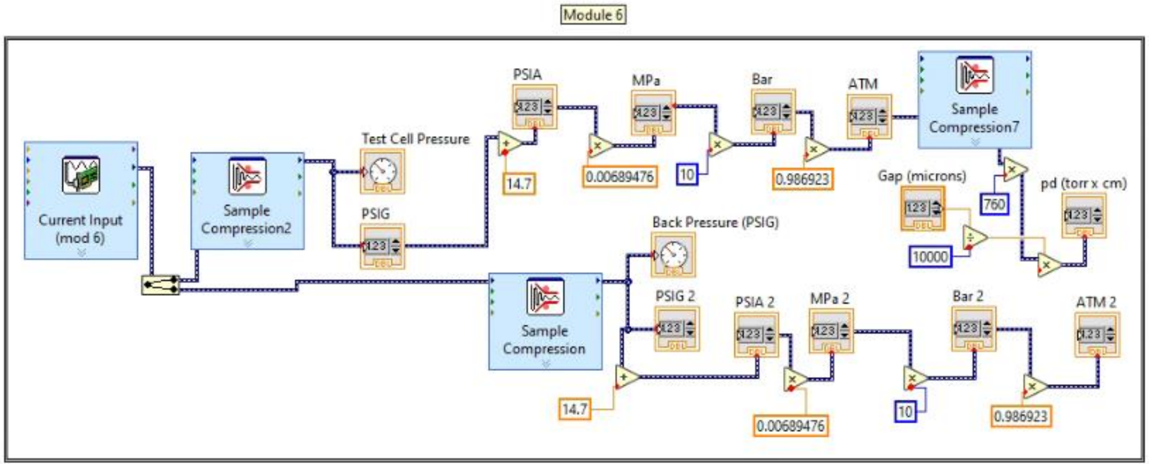

Figure B.6 Module 6

Module 8 is a voltage output card. This card can measure voltages ranging from -10-10 volts. This card measures the total voltage produced by the power supply and the current output from the power supply. The power supply outputs 0 V for no current and no voltage, and 10 V for maximum current and maximum voltage. The relationship is linear, and the calculations are done by LabVIEW. This block also produces a plot showing current and voltage outputs simultaneously.

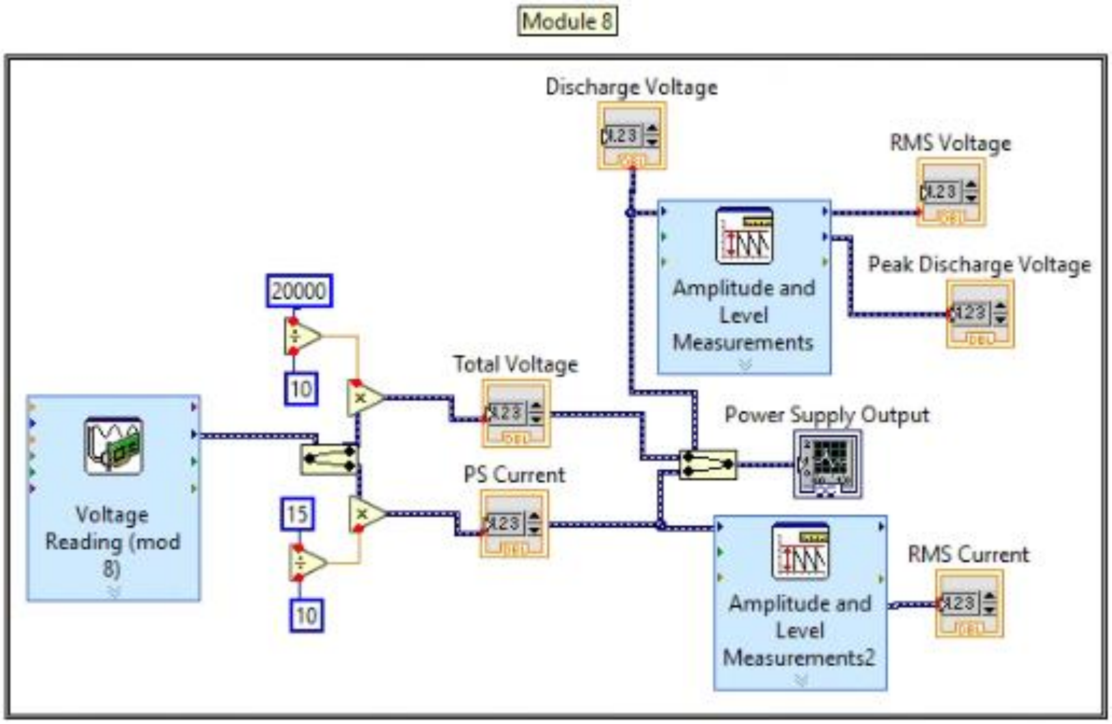

Figure B.7 Module 8

APPENDIX C

LOW PRESSURE TESTING

This LabVIEW program This prototype This is a high-pressure, high-voltage system. It is crucial for everyone's safety that the user operates with extreme caution and care. A low-pressure test can be performed to ensure all fittings are tightened properly and there is no leakage. A low-pressure test should be performed with pressurized air.

1) Turn the junction box on. This is done by flipping the switch on the junction box up to the on position.
2) Turn on the shop air.
3) Open the sCO2_Reactor_Controller shortcut.

Figure C.1 LabVIEW shortcut

4) In the LabVIEW program check the pressure of the test cell. If the pressure is greater than atmospheric pressure, slowly vent the air out of the back-pressure regulator by slightly cracking open the ball valve beside the back-pressure

regulator. Close the ball valve once the test cell pressure reaches atmospheric pressure. (If the test cell is already at atmospheric pressure, close the ball valve.)

5) Turn the Flow in on and wait until you hear the 3-way ball valve stop turning. Once the ball valve stops turning, turn the Flow in back off. (Do not leave these radio buttons turned on when they are not in use.) This will position the 3-way ball valve after the outlet of the booster pumps to flow up the flexible hose and into the test cell.

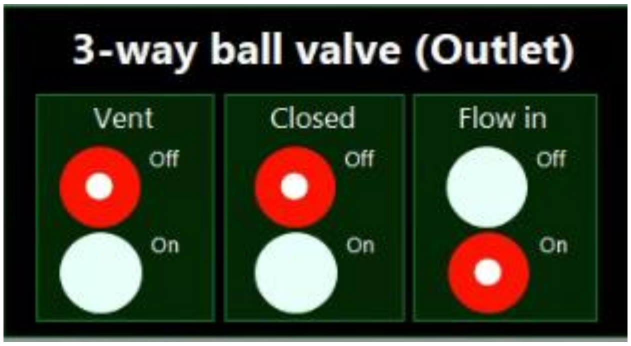

3-way ball valve (Outlet)

Vent ● Off ○ On

Closed ● Off ○ On

Flow in ○ Off ● On

Figure C.2 Flow in radio buttons

6) Turn the Air in on and wait until you hear the 3-way ball valve stop turning. Once the ball valve stops turning, turn the Air in back off. (Do not leave these radio buttons turned on when they are not in use.) This will position the 3-way ball valve at the inlet of the gas booster pump to flow air into the pump inlet.

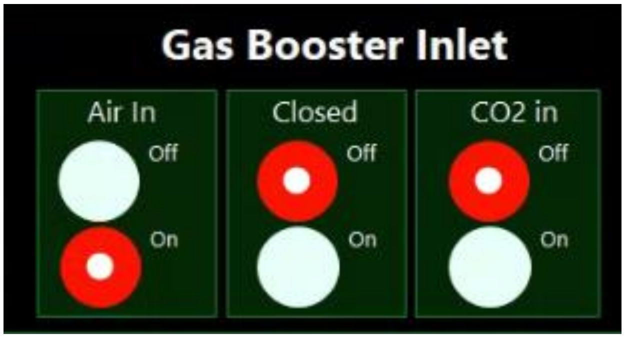

Gas Booster Inlet

Air In ○ Off ● On

Closed ● Off ○ On

CO2 in ● Off ○ On

Figure C.3 Air in radio buttons

7) Ensure that the valve on the inlet side of the test cell is open. Turn on the Air Flush. This button pump air into the test cell. Pressurize the test cell to the desired pressure. A good pressure is 400 psig. Turn the Air flush off when the desired pressure is reached.

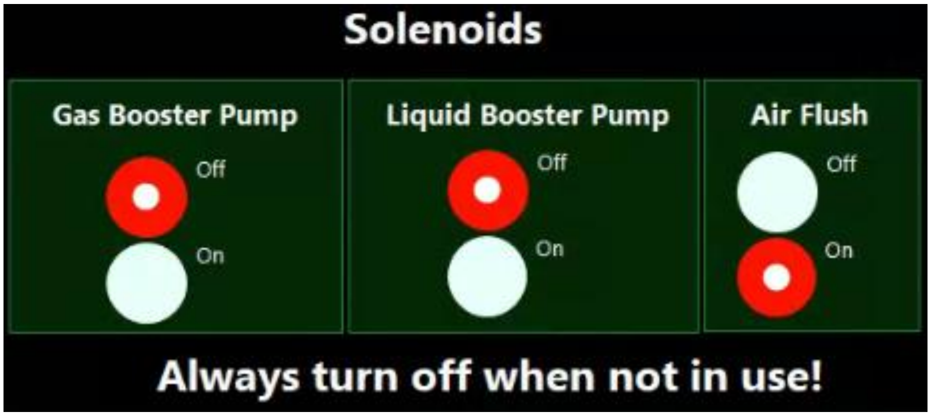

Always turn off when not in use!

Figure C.4 Air flush radio buttons

8) Close the valves that are directly before and after the test cell. Wait 15 seconds for the pressure to stabilize.

9) Watch the pressure gauge in the LabVIEW program to see if there is steady leakage.

10) A long pressure test can also be done to see if there is a slow leak. Observe the pressure on the LabVIEW program, and then hit the stop button. This is the red stop sign at the top of the program. The pressure will stay frozen on the screen. Leave the test cell for an extended period of time. Come back and hit run on the program. If the pressure has a significant drop, there is a leak.

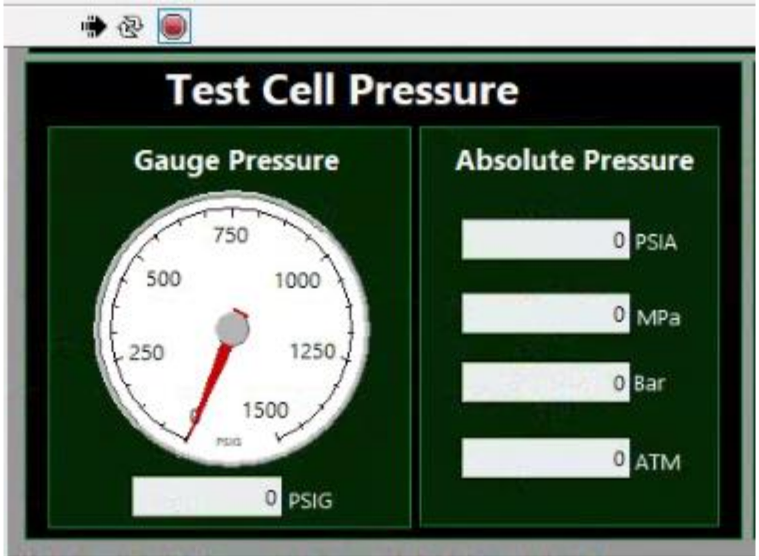

0 PSIG

0 PSIA

0 MPa

0 Bar

0 ATM

Figure C.5 Pressure gauge and run/stop buttons

11) If there is any leakage, find the leak using a soap bubble test. Then, tighten the fitting that is leaking.

12) Repeat step 9 if a leak was found.

APPENDIX D

GENERAL OPERATIONS

These instructions will clearly layout how to create supercritical CO$_2$.

1) Turn the junction on.

2) Turn on the shop air.

3) Close the outlet ball valve so that no fluid can leave the test cell when its pressurized.

4) Turn the Flow in on and wait until you hear the 3-way ball valve stop turning. Once the ball valve stops turning, turn the Flow in back off. (Do not leave these radio buttons turned on when they are not in use.) This will position the 3-way ball valve after the outlet of the booster pumps to flow up the flexible hose and into the test cell.

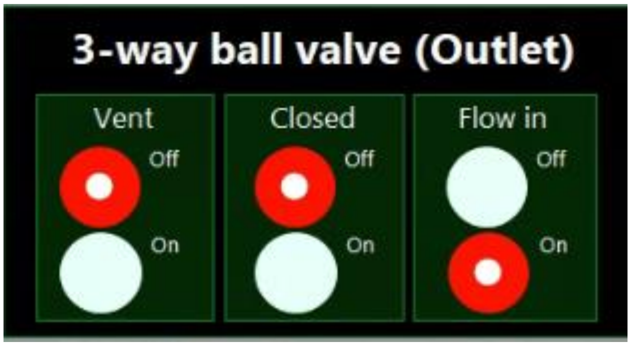

Figure D.1 Flow in radio buttons

5) Open the Nitrogen tank and increase the pressure to at least 110% of the desired test cell pressure. The nitrogen will supply the back-pressure.

6) Open the liquid CO_2 tank, and open the valve directly downstream of the CO_2 tank. This will make some noise as liquid CO_2 passes through the check valves of the liquid booster pump and the secondary check valve located downstream from the pump. The pressure should increase to 750-830 psig unless the tank is becoming empty.

7) Check the LabVIEW program to see what the pressure in the test cell is. Manually close the valve on the inlet side of the test cell. Slowly vent out approximately 200 psig of CO_2 from the outlet of the test cell. This step removes air from the test cell. Close the outlet valve once the pressure reaches approximately 600 psig.

8) Open the valve on the inlet side of the test cell. This will make some noise as more liquid CO_2 flows through the check valves.

9) Set the back-pressure in the LabVIEW program by typing the desired back pressure in the Setpoint box and hitting enter. The gauge showing the back-pressure should go up to match the setpoint pressure.

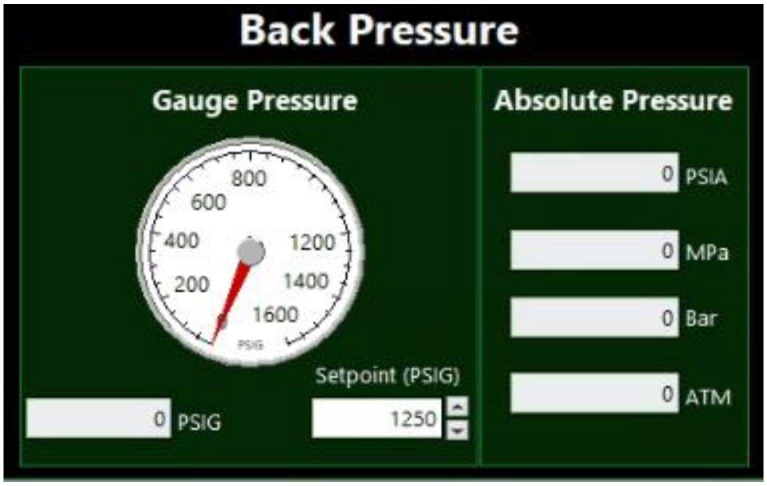

Figure D.2 Back-pressure setpoint

10) Open the outlet valve. This is safe now that the back-pressure regulator is engaged.

11) Pump CO_2 into the test cell by turning the Liquid Booster Pump on in the LabVIEW program. Watch the test cell pressure gauge and turn the pump off once the pressure is approximately 50 psig less than the back-pressure.

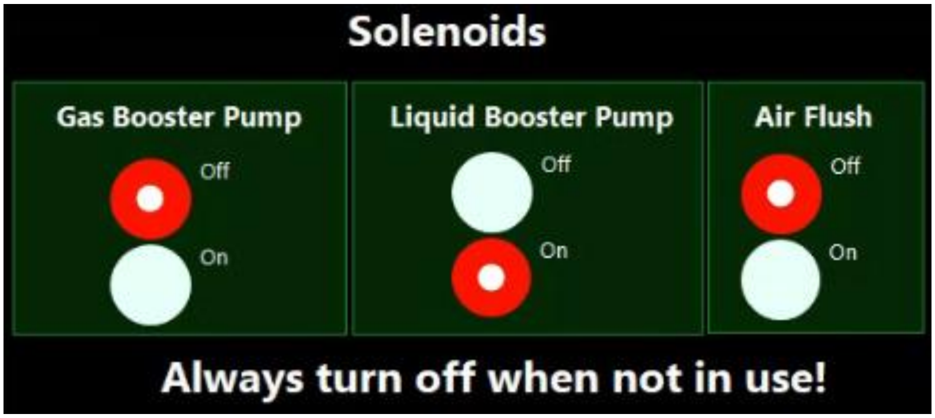

Figure D.3 Liquid booster pump

12) Manually close the valve leading to the inlet to the test cell. Next, move the 3-way ball valve (Outlet) to a closed position in the LabVIEW program. This method with trap pressurized CO_2 in the flexible hose so that it can be used later if needed.

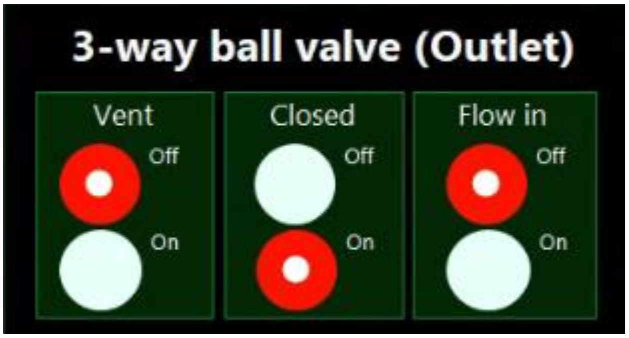

Figure D.4 Mitigate leakage

13) Close the liquid CO_2 tank and the valve just downstream of the tank.

14) Heat the test cell. There are two separate heat sources for the test cell. The test cell should be wrapped in heat wrap. Turn the heat wrap on, and make sure its

thermocouple is placed between the wrap and the bellow. Turn on the cartridge heaters by entering a setpoint temperature in the LabVIEW program.

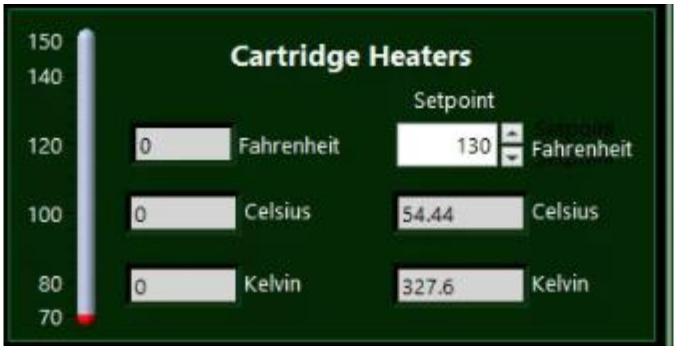

0 Fahrenheit
0 Celsius
0 Kelvin

Setpoint
130 Fahrenheit
54.44 Celsius
327.6 Kelvin

Figure D.5 Cartridge heaters

15) The test cell takes approximately 30 minutes to heat up. Now is a time to set up for shadowgraph imaging or optical emission spectroscopy.

16) Monitor the test cell pressure. If the pressure is dropping and leaks cannot be found with the soap bubble test, then it's likely that the leaking is happening in the back-pressure regulator. Close the outlet valve and proceed with testing. Monitor the pressure closely. If the temperature of the fluid increases the pressure will increase. The back-pressure regulator will need to be disassembled and cleaned before the next test.

17) Adjust the electrode gap by tightening the bolts on the top of the bellow.

18) Turn on the oscilloscope and set the viewing width to approximately 20 microseconds. Set the trigger to capture rising pulses at 20 amps. Set the power supply to measure RMS and maximum peaks.

19) Use the power supply to create plasma. The power supply can be controlled manually, or it can be controlled through LabVIEW. (Manual control has shown to be more accurate.)

20) After the plasma pulses, stop the LabVIEW program. Right click the plot and export the data to excel. Hit run on the LabVIEW program.

21) Record the RMS and maximum peak data from the oscilloscope. Save oscilloscope data to a USB drive. Take a picture of the electrode gap and record the test cell pressure and the test cell temperature.

22) Collect data. Parameters such as power supply current, temperature, electrode spacing, and pressure decrease can be modified while maintaining a pressurized test cell.

APPENDIX E

DEPRESSURIZING

Depressurizing the test cell can potentially be dangerous if done the wrong way. Rapid decompression creates dry ice. The exhaust vent is a plastic hose, so a slow depressurization is ideal.

1) Close the valve right before the back-pressure regulator.

2) Change the setpoint on the back-pressure regulator to 0 psig. This will vent out a small amount of CO_2.

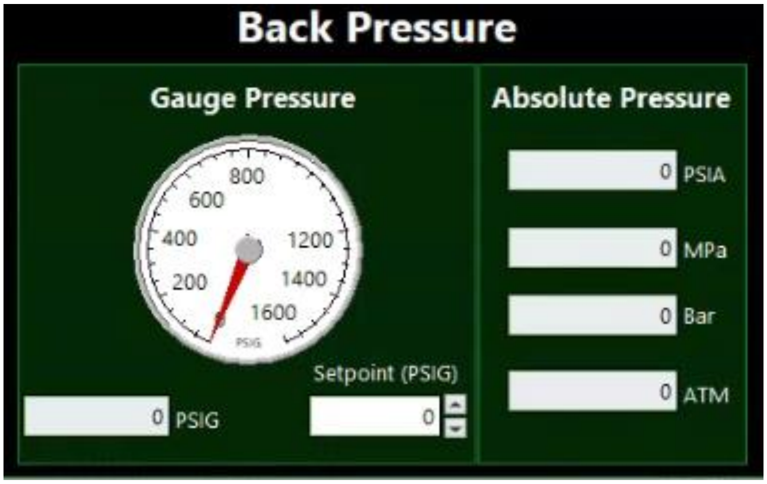

Back Pressure

Gauge Pressure

0 PSIG

Setpoint (PSIG): 0

Absolute Pressure

0 PSIA

0 MPa

0 Bar

0 ATM

Figure E.1 Depressurizing

3) Slowly crack open the valve downstream of the test cell so that the CO_2 flows out steadily. The test cell can take 1 or 2 minutes to depressurize.

4) There is a high-pressure load of CO_2 inside the flexible hose. This CO_2 can be stored in the hose and saved for the next test. Or the CO_2 can be vented.

5) Change the setpoint on the cartridge heaters to 0˚F.

6) Turn off the shop air, and close the Nitrogen tank, and make sure the CO_2 tanks are closed also.

7) Turn of the heat wrap controls.

8) Close the LabVIEW program.

9) Turn off the junction box.

APPENDIX F

DISASSEMBLY AND CLEANING

Cleaning and disassembly are not often necessary. Once 100-micron filters are added to the system, cleaning should very rarely be necessary. This is the guide for separating the test cell from the system and cleaning the sapphire windows.

1) Ensure that the test cell is not pressurized. This can be done by checking on the LabVIEW program or by slowly opening the exhaust valve and checking for flow.
2) Ensure that the test cell is not pressurized. This can be done by checking on the LabVIEW program or by slowly opening the exhaust valve and checking for flow.
3) Remove the arches by loosening the top fittings on the elbows. Tap lightly with a rubber mallet in an upward motion to dislodge the arches.

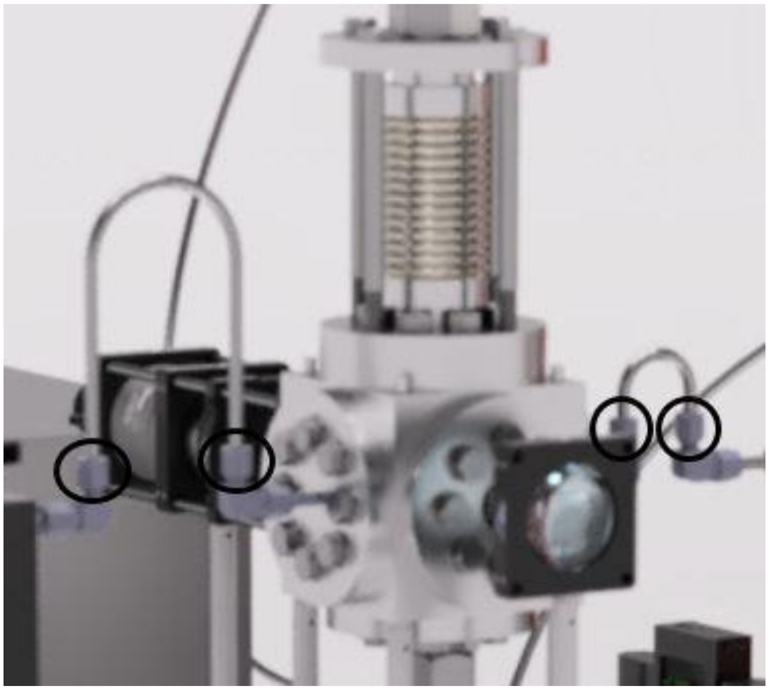

Figure F.1 Arch removal

4) Disconnect the top and bottom electrode fittings from the electrodes.
5) Loosen the feet of the test cell from the legs. Do not loosen the feet of the test cell from the table.
6) Carefully lift the test cell up and lay it on its side. The feet should still be in the same position on the table. This makes for an easy reassembly process.
7) Unscrew the legs from the test cell.
8) Place the test cell in a vice grip. Position it so the bottom flange can be removed.
9) Use a ⅜" inch socket wrench to remove the 8 bolts from the bottom flange. Remove the bolts in a star pattern.
10) Use a lens cleaning glass and ethanol to clean the inside and outside of the test cell windows. Also clean as much as the inside surface as possible. Clean the cathode tip as well.

11) After cleaning, place an o-ring inside the groove and finger tighten the flange onto the test cell. Make sure that the o-ring is in the groove.

12) Use a torque wrench to tighten each bolt with a torque of 37 ft lbs. Tighten the bolts in a star pattern.

13) Screw the legs back into the test cell. Do not tighten them too hard. They break easily if over tightened.

14) Gently lower the test cell into the feet on the table. Tighten the feet to the legs.

15) Reattach the arches and reattach the electrode fittings.

16) Make sure there is foil connecting the metal Conax electrode housing to the flange for both the top and bottom of the test cell. This completes the circuit for the grounded shield.

17) Cleaning is complete. It is generally good practice after disassembly to perform a pressure test and check for leaks.